Nonequilibrium dynamics of piecewise-smooth stochastic systems

Paul Matthias Geffert

School of Mathematical Sciences

Queen Mary University of London

Submitted in partial fulfillment of the requirements of the Degree of Doctor of Philosophy

May 2018

Statement of Originality

I, Paul Matthias Geffert, confirm that the research included within this thesis is my own work or that where it has been carried out in collaboration with, or supported by others, that this is duly acknowledged below and my contribution indicated. Previously published material is also acknowledged below.

I attest that I have exercised reasonable care to ensure that the work is original, and does not to the best of my knowledge break any UK law, infringe any third party's copyright or other Intellectual Property Right, or contain any confidential material.

I accept that the College has the right to use plagiarism detection software to check the electronic version of the thesis.

I confirm that this thesis has not been previously submitted for the award of a degree by this or any other university.

The copyright of this thesis rests with the author and no quotation from it or information derived from it may be published without the prior written consent of the author.

Signature:

Date:

Details of collaboration and publications:
1. Publications related to the content of the thesis

- P. M. Geffert, W. Just, *Nonequilibrium dynamics of a pure dry friction model subjected to coloured noise*, Phys. Rev. E **95**, 062111 (2017)

2. Other collaborations and publications

- W. Just, P. M. Geffert, A. Zakharova, E. Schöll, *Noisy dynamical systems with time delay: some basic analytical perturbation schemes with applications*, in *Control of Self-Organizing Nonlinear Systems*, edited by E. Schöll, S. H. L. Klapp, P. Hövel (Springer, Berlin, Heidelberg, 2016)

- P. M. Geffert, *Stochastic Non-Excitable Systems with Time Delay*, Springer Best Masters Series, (2015)

Abstract

Piecewise-smooth stochastic systems have attracted a lot of interest in the last decades in engineering science and mathematics. Many investigations have focused only on one-dimensional problems. This thesis deals with simple two-dimensional piecewise-smooth stochastic systems in the absence of detailed balance. We investigate the simplest example of such a system, which is a pure dry friction model subjected to coloured Gaussian noise. The finite correlation time of the noise establishes an additional dimension in the phase space and gives rise to a non-vanishing probability current. Our investigation focuses on stick-slip transitions, which can be related to a critical value of the noise correlation time. Analytical insight is provided by applying the unified coloured noise approximation. Afterwards, we extend our previous model by adding viscous friction and a constant force. Then we perform a similar analysis as for the pure dry friction case. With parameter values close to the deterministic stick-slip transition, we observe a non-monotonic behaviour of the probability of sticking by increasing the correlation time of the noise. As the eigenvalue spectrum is not accessible for the systems with coloured noise, we consider the eigenvalue problem of a dry friction model with displacement, velocity and Gaussian white noise. By imposing periodic boundary conditions on the displacement and using a Fourier ansatz, we can derive an eigenvalue equation, which has a similar form in comparison to the known one-dimensional problem for the velocity only. The eigenvalue analysis is done for the case without a constant force and with a constant force separately. Finally, we conclude our findings and provide an outlook on related open problems.

Contents

List of Figures

Acknowledgements

First I have to thank my supervisor Wolfram Just for the great experience of being a PhD student under his supervision. He gave me the freedom to pursue my own research ideas at my own pace. His extremely broad knowledge was very helpful during scientific discussions when he pointed out inaccuracies in my reasonings and calculations or he revealed unexpected connections between particular areas of mathematics and physics. This thesis would not have been possible without his support and patience.

Many thanks to all members of the School of Mathematical Sciences at Queen Mary University of London, especially my former and current PhD colleagues, who made my time here a very enjoyable one.

I thank Queen Mary University of London and the School of Mathematical Sciences for providing financial support for my PhD studies.

A big thank you to Hannah Sheeran, Jarrod Williams and Johannes Pausch for proofreading this thesis.

I thank my friends and my family, especially my parents Dorothea and Michael Geffert, my brother Johannes Geffert, my sister Karin Geffert along with Matthias and David Reiners for constant support and encouragement throughout my entire time of studying. Many thanks as well to Almut and Christian Beck for their support and many useful pieces of advice, especially at the beginning of my time as a PhD student.

Last but not least, I want to thank my girlfriend Wei Sam Soo for her moral support, for being understanding when I became very busy writing my thesis, and for being a constant source of comfort and love.

This thesis is dedicated to my late grandfather Walter Schröck-Vietor, who cannot witness this achievement with me but I will always remember his encouragement and his great interest in my studies.

Chapter 1

Introduction

Piecewise-smooth dynamical systems have attracted a lot of attention over the past decade. They have been widely used for phenomenological models in engineering and other applied sciences. As such systems cannot be investigated in the same way as smooth dynamical systems, a new theoretical framework is needed for the mathematical treatment [28]. Piecewise-smooth dynamical systems can be modelled by differential equations with discontinuities [34]. The dynamics exhibit new and unexpected phenomena, new types of bifurcations, which do not appear in the theory of smooth dynamical systems [21,68], or a loss of determinism as multivalued solutions arise although the dynamics started from a single initial condition [53]. In the past few years, concepts from smooth dynamical systems have been adapted and used in the context of piecewise-smooth dynamical systems, e.g. the so-called master stability function, to investigate the synchronisation properties of coupled non-smooth systems [23, 70, 79]. Applications of piecewise-smooth dynamical systems can be found in various fields of research, e.g. in neurodynamics [22] or superconducting resonators [54]. Systems with dry friction (or Coulomb friction) are very prominent examples of piecewise-smooth systems [9,10,100] and have been investigated in many different contexts, e.g. in seismology [13,14]. Characteristic of the dynamics of these systems is the appearance of stick-slip motion [30,98].

In comparison to deterministic systems, the theory of piecewise-smooth stochastic systems is still in its infancy. Stochastic models with discontinuous drifts are used in physics and biology, e.g. in the framework of Brownian ratchets [69,81,85,86] or for a phenomenological description of the stochastic motion of small solid objects

on a solid surface, i.e. stochastic dry friction models [3, 4, 15, 27, 48]. The dynamics of such models exhibits new features such as noise dependency of the correlation time [94] or directed motion due to the interplay of asymmetric vibrations and dry friction in the absence of a constant bias [7]. Non-Gaussian distributions for the underlying macroscopic variables have been found [27, 48, 57, 71, 72]. In addition, stochastic dry friction models have been used in the framework of diffusive transport in graphene [80]. From a more rigorous point of view, the influence of Gaussian white noise on sliding motion in Filippov systems close to a switching manifold and near periodic orbits has been investigated [88, 90].

Analytical results are available for a few piecewise-smooth stochastic systems, e.g. exact solutions for the propagator [15, 94], closed expressions for the power spectral density via Laplace transformations [95] and estimates for the first passage time distribution [19]. Furthermore, the concepts of path integral methods and weak-noise approximations, which are normal tools to study smooth stochastic models, have been extended to investigate piecewise-smooth stochastic systems [5, 6, 18]. In addition to the aforementioned studies where Gaussian noise sources were used, dry friction models with non-Gaussian noise have been considered as well [7, 8, 58]; these models are partially exactly solvable. While the aformentioned investigations focused on Langevin dynamics, dry friction has been considered in connection to the Boltzmann-Lorentz equation in the framework of granular material, e.g. studies on a granular rotor [84, 92] and an adiabatic piston subjected to granular gas [83, 93].

Some features of stochastic dry friction models have been found in experiments including water droplets and small solid objects sliding on a vibrating substrate [16, 42–44, 73] or rotators subjected to granular media [32, 40, 41].

The abovementioned investigations focused mainly on one-dimensional problems. For higher dimensions, studies are very rare. A few examples are numerical investigations on the displacement statistics [72], the derivation of asymptotic expressions for the transitional probability distribution in an N-dimensional Fillipov system [89], and results on the autocorrelation function of the velocity in higher dimensions [26]. The obvious advantage of one-dimensional problems is that analytical results are easier to compute. On the other hand, for example, regarding two or higher dimensional stochastic systems, the question always arises as to whether detailed balance is violated [82], which can hamper analytical computations. Prominent examples for such a scenario are systems with Gaussian coloured noise.

Stochastic perturbations are very often modelled by using Gaussian white noise, which is usually an appropriate choice and analytical calculations can be done since such problems often represent a Markov process. However, if the correlation time of the noise and the characteristic time scale of the investigated system are of the same order, a correlated noise (or coloured noise) is more appropriate [47]. Analytical calculations of problems containing coloured noise are hampered by the lack of detailed balance and Fokker-Planck techniques cannot be used directly since we are dealing with a non-Markov process. Such a correlated noise can be generated for example by an Ornstein-Uhlenbeck process, which enables us to obtain an higher dimensional equivalent Markov process. In general, one has to rely on approximation schemes, which are well established in the literature [36, 37, 55]. Models including a coloured noise have been studied in many different contexts, e.g. magnetic resonance [62], neurodynamics [11] and recently in active particle systems [35, 65, 99].

In this thesis we will go beyond one-dimensional piecewise-smooth problems and investigate simple two-dimensional models, which do not obey detailed balance. An obvious choice lies in focusing on a piecewise-smooth system subjected to coloured noise, which gives rise to an additional dimension in phase space. We are interested in how the impact of the correlation time of the noise affects the properties of the underlying system, e.g. how the shape of the probability distribution or the power spectral density changes. In general, we want to elaborate on whether transition phenomena between the low correlation regime and high correlation regime become visible and can be expressed by analytical means. The investigations focus first on a pure dry friction model before we study a system with dry and viscous friction plus a constant force, similarly to the case of the model subjected to white noise [94].

In addition, we will consider the eigenvalue problem of a dry friction model with displacement, velocity and Gaussian white noise. As results for the one-dimensional for the velocity are well established in the literature, the question is how the dry friction affects the dynamics of the displacement of a particle. In particular, we want to investigate the structure of the underlying eigenvalue spectrum and study the impact of dry friction on the eigenvalues. Our goal is to perform this analysis analytically to a large extent.

1.1 The Langevin equation with dry friction

To set the background of this thesis, we discuss some aspects of Brownian motion with dry friction. Historically, only a viscous friction has been taken into account in the Langevin equation [38]. Therefore, we investigate the impact of an additional dry friction contribution, which comes into play when solid-solid interactions are considered, e.g. a solid object sliding over a vibrating plate. The dry friction can be characterised by the following scenario: when the object is at rest, an applied force has to overcome a certain threshold value to move the object and, consequently, it slides on the plate. If the force is not large enough, the object does not move and remains at its current position. The simplest way to model dry friction from a macroscopic and phenomenological point of view is by using the sign-function as the velocity dependent friction, which has the following properties:

$$\sigma(\pm v) = \pm 1, \quad \sigma(0) = 0. \tag{1.1}$$

More complex and more challenging friction models can be used to take into account all characteristics, which can occur in systems with dry friction like hysteresis and the Stribeck curve [100]. However, in this thesis, we stick to the model shown in Eq. (1.1).

Initially, the work of Caughey et al. [3, 4, 15], de Gennes [27] and Kawarada and Hayakawa [57] have only considered the stochastic dynamics of an object on a vibrating horizontal plate and therefore only viscous and dry friction have been taken into account there. However, experiments have been conducted by using an inclined plate, where the object has been subjected to an additional constant force as well e.g. [16]. Thus, the Langevin equation for the velocity of a particle with dry friction, viscous friction and a constant force reads

$$\dot{v}(t) = -\nu\sigma(v(t)) - \gamma v(t) + F + \sqrt{D}\xi(t). \tag{1.2}$$

Here ν is the dry friction coefficient and γ the viscous friction coefficient. F denotes the constant force and D is the diffusion constant. For convenience, we have set the mass of the particle to one. The variable $\xi(t)$ describes Gaussian white noise with

zero mean and a delta-correlated autocorrelation function

$$\langle \xi(t) \rangle = 0, \quad \langle \xi(t)\xi(t') \rangle = \delta(t - t'), \tag{1.3}$$

where $\langle \ldots \rangle$ denotes the average over all realisations. Since Eq. (1.2) represents a Markov process, we can derive the corresponding Fokker-Planck equation for the propagator of the velocity

$$\frac{\partial}{\partial t} P(v, t|v_0, 0) = \frac{\partial}{\partial v} \left(\nu\sigma(v) + \gamma v - F \right) P(v, t|v_0, 0) + \frac{D}{2} \frac{\partial^2}{\partial v^2} P(v, t|v_0, 0). \tag{1.4}$$

Here we have the initial condition $P(v, 0|v_0, 0) = \delta(v - v_0)$. As the noise is additive in Eq. (1.2), we do not need to specify whether we use the Ito or Stratonovich interpretation [38].

In the case of pure dry friction ($\gamma = 0,\ F = 0$), Eq. (1.2) simplifies to

$$\dot{v}(t) = -\nu\sigma(v(t)) + \sqrt{D}\xi(t). \tag{1.5}$$

This case is also called Brownian motion with two-valued drift [88]. By applying the following transformation to non-dimensional units (also see App. B.3 as well)

$$x = \frac{2\nu}{D} v, \ t' = \frac{2\nu^2}{D} t \tag{1.6}$$

the corresponding Fokker-Planck equation reads

$$\frac{\partial}{\partial t'} P(x, t'|x_0, 0) = \frac{\partial}{\partial x} \sigma(x) P(x, t'|x_0, 0) + \frac{\partial^2}{\partial x^2} P(x, t'|x_0, 0) \tag{1.7}$$

and we have the initial condition

$$P(x, 0|x_0, 0) = \delta(x - x_0). \tag{1.8}$$

To solve Eq. (1.7) via the eigenfunction expansion of the propagator, some care needs to be taken. Since we are dealing with a piecewise-smooth drift function, we have to solve the problem for the two half spaces ($x > 0$ and $x < 0$) separately and then match the solutions together at the continuity, by imposing continuity for the eigenfunctions and the probability current. Further details of such a calculation are

presented in the next Chapter 2 and in [94]. Thus, the time-dependent solution can be found explicitly for the pure dry friction case

$$P(x,t'|x_0,0) = \frac{e^{-t'/4}}{2\sqrt{\pi t'}} e^{-(|x|-|x_0|)/2} e^{-(x-x_0)^2/(4t')} + \frac{e^{-|x|}}{4}\left[1+\mathrm{erf}\left(\frac{t'-(|x|+|x_0|)}{2\sqrt{t'}}\right)\right] \tag{1.9}$$

where

$$\mathrm{erf}(z) = \frac{2}{\sqrt{\pi}}\int_0^z e^{-t^2} dt \tag{1.10}$$

is the error function. In the stationary limit $t' \to \infty$, we obtain the stationary probability distribution

$$P(x) = \frac{1}{2}\exp(-|x|). \tag{1.11}$$

In Fig. 1.1, we present the time evolution of the propagator Eq. (1.9). We start from the initial condition $x_0 = 2$ (see Eq. (1.8)) and the system evolves until it reaches the stationary distribution (blue curve in Fig. 1.1). The characteristics of a system with dry friction is the cusp of the probability distribution, which can be observed at $v = 0$.

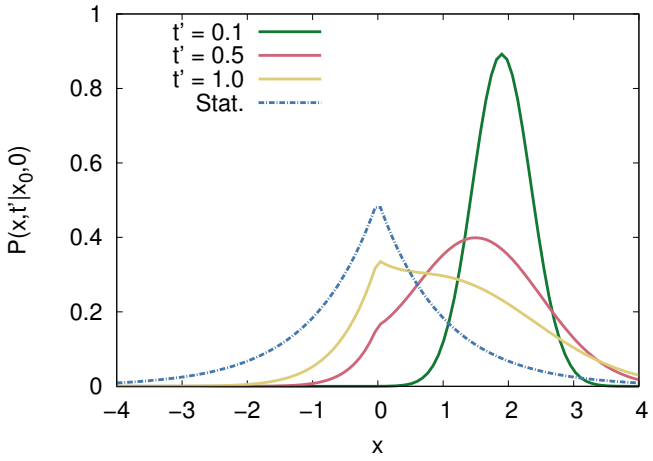

Figure 1.1: Time evolution of the propagator from Eq. (1.9) for the pure dry friction case. The initial condition is $x_0 = 2$. The dotted-dashed line denotes the stationary probability distribution (Eq. (1.11)).

For additional viscous friction and a constant force, it has not been possible to find an exact solution for the propagator. Nevertheless, an expression for the time-dependent solution of the underlying Fokker-Planck equation (Eq. (1.4)) can

be found and represented in terms of parabolic cylinder functions (see App. C) by using a spectral decomposition [94] or considering the problem in Laplace space [95].

The shown Langevin equation (Eq. (1.2)) represents a Markov process, which enables us to apply Fokker-Planck techniques, which means that an analytical treatment of the problem is possible. Furthermore, with natural boundary conditions the probability current vanishes in the stationary case in one dimension, which straightforwardly leads to the stationary probability distribution. This does not apply for systems with coloured noise, in which we have a non-vanishing stationary probability current, as we will see later in this thesis.

1.2 Outline of the thesis

This thesis consists of six chapters and four appendices. Chapter 2 gives an introduction on the concepts and methods that are used in this thesis. Thus, these preliminaries are important to support the understanding of the thesis.

Chapter 3 deals with the investigation of a pure dry friction model subjected to coloured noise. We derive an analytical expression for the marginal stationary probability distribution of the velocity by using the so-called unified coloured noise approximation. The joint probability distribution for the velocity and the noise amplitude is computed numerically and its properties are discussed in comparison with an analytical asymptotic expression. The findings are supported by numerical simulations of the stationary probability current to underline the nonequilibrium character of our model. Afterwards, we turn towards dynamical features of the model like correlations of the velocity, which are computed via the power spectral density. Finally, the statistics for sticking and sliding time periods are investigated.

In Chapter 4, we extend the pure dry friction model with coloured noise by adding viscous friction and constant bias. Here the focus lies on the interplay of the constant force and the correlation time of the noise. The analysis in this chapter is basically the same as in Chapter 3. We will focus our investigations on parameter values close to the deterministic stick-slip transition of the model.

In Chapter 5, we derive an eigenvalue equation for the problem of a two-dimensional piecewise-smooth system with displacement, velocity and Gaussian white noise. Here we make use of periodic boundary conditions for the displacement, which facil-

itates analytical calculations. The procedure is based on the approach used for the one-dimensional problem for the velocity only. The eigenvalue analysis is performed by considering the problems with and without a constant force separately.

Finally, we summarise the main results of this thesis in Chapter 6 and also provide an outlook on closely connected open and interesting problems.

Details on calculations and derivations are put in the appendices to facilitate the reading of the thesis and to keep it self-contained.

Chapter 2

Preliminaries

For the convenience of the reader, we introduce and recall particular methods and results in this chapter to support the understanding of the thesis. In Sec. 2.1, we investigate an Ornstein-Uhlenbeck process subjected to coloured noise. As this model is tractable analytically, it is suitable to show the characteristics of coloured noise and the important differences towards Gaussian white noise. In Sec. 2.2 we introduce the so-called unified coloured noise approximation, which is a simple approximation scheme for systems with coloured noise, where the violation of detailed balance hampers analytical calculations. This approximation is used in the Chapters 3 and 4. We revisit results from a Fokker-Planck approach to Brownian motion with dry friction in Sec. 2.3. The presented methods are applied in Chapter 5. Finally, we elaborate the connection of our investigations to more rigorous treatments of Filippov systems with noise.

2.1 Ornstein-Uhlenbeck process driven by coloured noise

Before we start our investigations on systems with coloured noise, we recall known results from the classical Ornstein-Uhlenbeck process with Gaussian white noise. The equation of motion reads

$$\dot{v}(t) = -\gamma v(t) + \sqrt{D}\xi(t) \tag{2.1}$$

where γ is the viscous friction coefficient, D the diffusion constant and $\xi(t)$ describes Gaussian white noise with zero mean $\langle \xi(t) \rangle = 0$ and δ correlation $\langle \xi(t)\xi(s) \rangle = \delta(t-s)$. Through the entire thesis we will set $D = 1$ (by applying appropriate transformations of the variables, we can always get rid of the diffusion constant, see App. B). The corresponding Fokker-Planck equation reads

$$\frac{\partial}{\partial t} P(v,t|v_0,t_0) = \frac{\partial}{\partial v} \gamma v P(v,t|v_0,t_0) + \frac{1}{2} \frac{\partial^2}{\partial v^2} P(v,t|v_0,t_0). \tag{2.2}$$

It can be rewritten in the form

$$\frac{\partial}{\partial t} P(v,t|v_0,t_0) = -\frac{\partial}{\partial v} J(v,t), \tag{2.3}$$

$$J(v,t) = -\gamma v P(v,t|v_0,t_0) - \frac{1}{2} \frac{\partial}{\partial v} P(v,t|v_0,t_0). \tag{2.4}$$

Eq. (2.3) is interpreted as a continuity equation with the probability current $J(v,t)$. We impose natural boundary conditions, which means that the probability distribution and the probability current vanishes at $v \to \pm\infty$. As we have a one dimensional problem, it follows that the stationary probability current vanishes everywhere. Therefore, the stationary solution can be obtained by a straightforward integration from Eq. (2.4) and we get

$$P(v) = \sqrt{\frac{\gamma}{\pi}} \exp\left(-\gamma v^2\right). \tag{2.5}$$

The time-dependent solution of Eq. (2.2) reads

$$P(v,t|v_0,0) = \sqrt{\frac{\gamma}{\pi(1-e^{-2\gamma t})}} \exp\left[-\frac{\gamma(v-v_0 e^{-\gamma t})^2}{1-e^{-2\gamma t}}\right] \tag{2.6}$$

with the initial condition

$$P(v,0|v_0,0) = \delta(v-v_0). \tag{2.7}$$

By using these results (Eqs. (2.5) and (2.6)), the stationary autocorrelation function can be expressed via [38]

$$\begin{aligned} G(t) &= \langle (v(t) - \langle v \rangle)(v(0) - \langle v \rangle) \rangle \\ &= \langle v(t)v(0) \rangle - \langle v \rangle^2 \\ &= \int_{-\infty}^{\infty} \int_{-\infty}^{\infty} v v_0 P(v, t|v_0, 0) P(v_0) dv dv_0 \\ &= \frac{1}{2\gamma} \exp\left(-\gamma t\right) \\ &= \frac{\tau_c}{2} \exp\left(-\frac{t}{\tau_c}\right). \end{aligned} \tag{2.8}$$

Here, we have defined the correlation time $\tau_c = \gamma^{-1}$ and we have zero mean for the velocity $\langle v \rangle = 0$. The power spectral density of the velocity is defined as

$$S_{vv}(\omega) = \frac{1}{2\pi T} \lim_{T \to \infty} |v(\omega)|^2, \tag{2.9}$$

where $v(\omega)$ denotes the Fourier transform of the velocity $v(t)$. Using the Wiener-Khinchin theorem [38], we can find the power spectral density for the velocity

$$\begin{aligned} S_{vv}(\omega) &= \frac{1}{2\pi} \int_{-\infty}^{\infty} e^{-i\omega t} G(t) dt \\ &= \frac{1}{2\pi} \frac{1}{\gamma^2 + \omega^2}. \end{aligned} \tag{2.10}$$

Here we have used the property of the autocorrelation function $G(t) = G(-t)$. The full width at half maximum of the spectral density reads $\Delta\omega = 2\gamma$. We note the relation between the correlation time and the full width at half maximum for linear stochastic processes

$$\Delta\omega = \frac{2}{\tau_c}. \tag{2.11}$$

Next, we replace the Gaussian white noise $\xi(t)$ in Eq. (2.1) with an Ornstein-Uhlenbeck noise $\eta(t)$

$$\dot{v}(t) = -\gamma v(t) + \eta(t). \tag{2.12}$$

$\eta(t)$ is exponentially correlated

$$\langle \eta(t)\eta(s)\rangle = \frac{1}{2\tau}\exp\left(-\frac{|t-s|}{\tau}\right), \tag{2.13}$$

and τ denotes the correlation time of the noise. This noise is generated by an Ornstein-Uhlenbeck process

$$\dot{\eta}(t) = -\frac{\eta}{\tau} + \frac{\xi(t)}{\tau}. \tag{2.14}$$

Due to the correlation time of the noise τ, which can be interpreted as the memory of the noise, Eq. (2.12) describes a non-Markov process. Therefore, we cannot apply our previously used techniques to Eq. (2.12). By taking the limit $\tau \to 0$, the coloured noise becomes a white noise $\eta(t) \to \xi(t)$. The equivalent two-dimensional Markov process reads

$$\dot{v}(t) = -\gamma v(t) + \eta(t), \tag{2.15a}$$

$$\dot{\eta}(t) = -\frac{\eta}{\tau} + \frac{\xi(t)}{\tau}. \tag{2.15b}$$

The corresponding Fokker-Planck equation reads

$$\begin{aligned}\frac{\partial}{\partial t}P(v,\eta,t|v_0,\eta_0,t_0) &= \frac{\partial}{\partial v}(\gamma v - \eta)P(v,\eta,t|v_0,\eta_0,t_0) \\ &\quad + \frac{\partial}{\partial \eta}\left(\frac{\eta}{\tau} + \frac{1}{2\tau^2}\frac{\partial}{\partial \eta}\right)P(v,\eta,t|v_0,\eta_0,t_0).\end{aligned} \tag{2.16}$$

We can rewrite it as a continuity equation

$$\frac{\partial}{\partial t}P(v,\eta,t|v_0,\eta_0,t_0) = -\left(\frac{\partial}{\partial v}J_v(v,\eta) + \frac{\partial}{\partial \eta}J_\eta(v,\eta)\right) \tag{2.17}$$

with the components of the two-dimensional probability current $J(v,\eta)$

$$J_v(v,\eta) = (-\gamma v + \eta)P(v,\eta,t|v_0,\eta_0,t_0), \tag{2.18}$$

$$J_\eta(v,\eta) = \left(-\frac{\eta}{\tau} - \frac{1}{2\tau^2}\frac{\partial}{\partial \eta}\right)P(v,\eta,t|v_0,\eta_0,t_0). \tag{2.19}$$

In one dimension, it is quite straightforward to find the stationary solution, see Eqs. (2.2) - (2.5).

For two or more dimensions, the stationary probability current does not vanish in general. Only if the drift coefficients satisfy the so-called potential conditions, the stationary probability current vanishes everywhere and we can proceed as in one dimension to find the stationary distribution via a straightforward integration [82]. The potential conditions for the drift coefficients A_i read

$$\frac{\partial A_i}{\partial x_j} = \frac{\partial A_j}{\partial x_i}. \tag{2.20}$$

In Eq. (2.16) we have $A_v = -\gamma v + \eta$, $A_\eta = -\eta/\tau$, thus the conditions (Eq. (2.20)) are not fulfilled here. If these conditions do not hold, finding the stationary solution of the Fokker-Planck equation becomes more difficult as a straightforward integration is not possible and other analytical or numerical methods have to be applied.

The condition of a vanishing probability current is also known as a version of the condition of detailed balance. Roughly speaking detailed balance holds in system if each transition is balanced by the reverse transition. For a system described by a Fokker-Planck equation, detailed balance holds if the irreversible part of the stationary probability current vanishes [82]. The formulation of detailed balance in the framework of the Fokker-Planck equation has been developed by van Kampen [96,97] and Graham and Haken [45]. A detailed discussion including the application of these concepts to Kramers' equation (Brownian motion in a potential) [59] can be found in [82]. Kramers' equation is an example for a system, where the potential conditions do not hold, but the system satisfies detailed balance since the irreversible part of the probability current vanishes. Even more, the conditions of detailed balance can be used in this case to find the stationary distribution. However, systems including a coloured noise do not satisfy detailed balance [33, 47, 63].

Nevertheless, the stationary solution for Eq. (2.16) can be found analytically; it reads [82]

$$P(v,\eta) = \frac{\sqrt{\gamma\tau}(1+\gamma\tau)}{\pi} \exp\left[-\gamma(1+\gamma\tau)^2 v^2 + 2\gamma\tau(1+\gamma\tau)v\eta - \tau(1+\gamma\tau)\eta^2\right]. \tag{2.21}$$

The above expression can be derived using various methods, e.g. applying a double Fourier transform to both variables in the Fokker-Planck equation and then making use of the method of characteristics. Eq. (2.21) describes a correlated, bivariate normal distribution. The time-dependent solution $P(v,\eta,t|v_0,\eta_0,0)$ can be found

the same way, but we will not state this result here. The marginal probability distribution $P(v)$ can be obtained via an integration over η

$$\begin{aligned} P(v) &= \int_{-\infty}^{\infty} P(v,\eta)d\eta \\ &= \sqrt{\frac{\gamma(\gamma\tau+1)}{\pi}} \exp\left(-\gamma(\gamma\tau+1)v^2\right). \end{aligned} \tag{2.22}$$

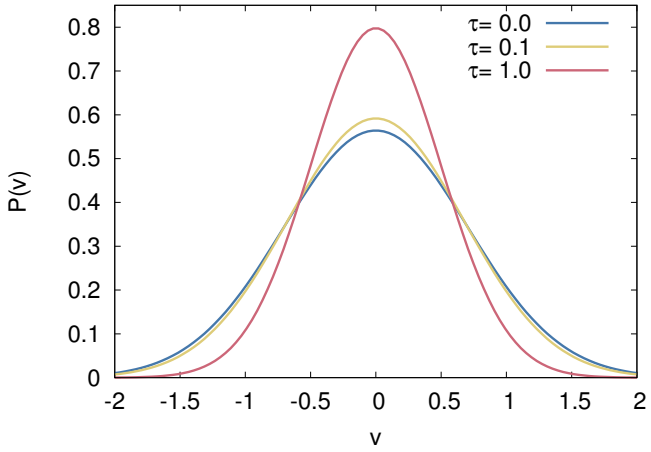

Figure 2.1: Stationary distribution $P(v)$ (Eq. (2.22)) for different values of the correlation time of the noise: $\tau = 0.0$ (blue), $\tau = 0.1$ (yellow), $\tau = 1$ (red). Further parameter: $\gamma = 1$.

In Fig. 2.1, we can observe that the probability distribution becomes narrower with increasing τ, as the variance scales $\sigma^2 \sim \tau^{-1}$. This result does not come as a surprise, as the amplitude of the noise $\eta(t)$ decreases when we increase the correlation of the noise. In the white noise limit $\tau \to 0$, we arrive at the known result for an Ornstein-Uhlenbeck process, see Eq. (2.5). In order to visualize that the system does not obey detailed balance, we calculate the stationary probability current (Eqs. (2.18) and (2.19))

$$J_v(v,\eta) = (-\gamma v + \eta)P(v,\eta), \tag{2.23a}$$

$$J_\eta(v,\eta) = \frac{\gamma(\eta\tau - (1+\gamma\tau)v)}{\tau} P(v,\eta), \tag{2.23b}$$

where $P(v,\eta)$ is the stationary joint probability density from Eq. (2.21).

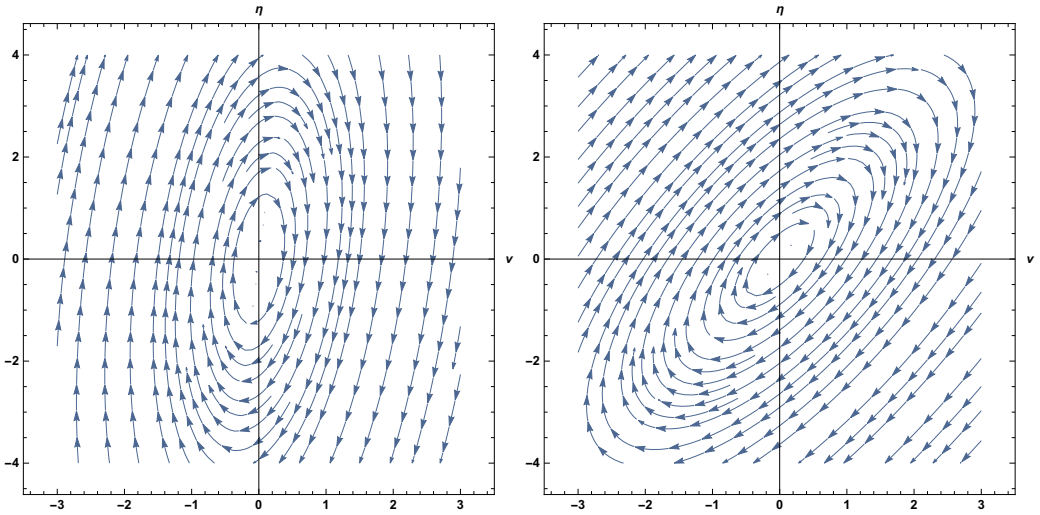

(a) $\tau = 0.1$ (b) $\tau = 1.0$

Figure 2.2: Stream plot of the stationary probability current for $\tau = 0.1$ (a) and $\tau = 1.0$ (b) according to Eqs. (2.23a) and (2.23b). Further parameter: $\gamma = 1$ in both figures. The stream plot displays the normalised vector field of the current.

Fig. 2.2 shows clearly that for a non-zero correlation time of the noise τ the stationary probability current does not vanish, which is a clear signature of the nonequilibrium character of this model. Furthermore, the coloured noise $\eta(t)$ induces an additional drift term (see Eq. (2.16)), which leads to the rotational form of the current.

To investigate the dynamical properties of the model, e.g. the power spectral density, we perform a Fourier transform of the equations of motion (Eqs. (2.15a) and (2.15b)):

$$-i\omega v(\omega) = -\gamma v(\omega) + \eta(\omega), \tag{2.24a}$$

$$-i\omega\eta(\omega) = -\frac{\eta(\omega)}{\tau} + \frac{\xi(\omega)}{\tau}. \tag{2.24b}$$

Rearranging the equations yields

$$v(\omega) = \frac{\eta(\omega)}{\gamma - i\omega}, \quad \eta(\omega) = \frac{\xi(\omega)}{1 - i\tau\omega}. \tag{2.25}$$

The power spectral density of a variable x can then be found via

$$\delta(\omega - \omega')S_{xx}(\omega) = \langle x(\omega)x^*(\omega')\rangle \tag{2.26}$$

where $x^*(\omega)$ denotes the complex conjugate of $x(\omega)$ [38]; thus, we obtain

$$S_{\eta\eta}(\omega) = \frac{1}{1+\tau^2\omega^2}, \tag{2.27a}$$

$$S_{vv}(\omega) = \frac{1}{(\gamma^2+\omega^2)(1+\tau^2\omega^2)}. \tag{2.27b}$$

We can observe that both power spectral densities are Lorentzian shaped; for $\tau \neq 0$ the spectrum for the noise variable η shows a ω^{-2} decay for high frequencies, whereas the spectrum for the velocity decays with ω^{-4}. Taking the white noise limit $\tau \to 0$, $S_{\eta\eta}(\omega)$ becomes a constant and $S_{vv}(\omega)$ changes towards a Lorentzian with ω^{-2} decay at high frequencies.

From Eqs. (2.27a) and (2.27b) we can find the full width at half maximum respectively

$$\Delta\omega_\eta = \frac{2}{\tau}, \tag{2.28a}$$

$$\Delta\omega_v = \sqrt{2\left(\frac{\sqrt{\gamma^4\tau^4+6\gamma^2\tau^2+1}-\gamma^2\tau^2-1}{\tau^2}\right)}. \tag{2.28b}$$

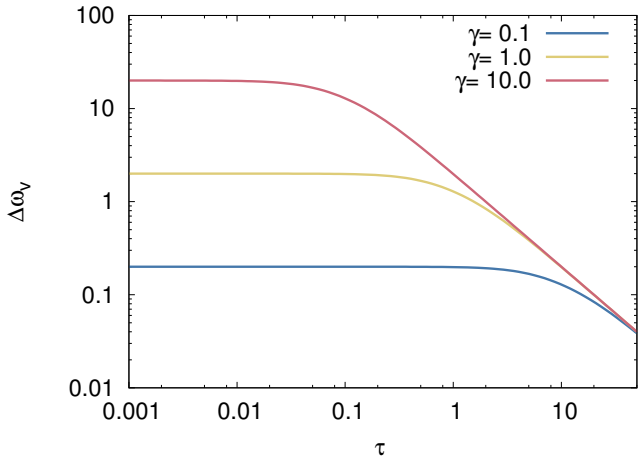

Figure 2.3: Full width at half maximum $\Delta\omega_v$ as a function of the noise correlation time τ for three different values of γ, obtained from Eq. (2.28b).

As $S_{\eta\eta}(\omega)$ becomes a constant in the white noise limit, it is not surprising that $\Delta\omega_\eta \to \infty$. $\Delta\omega_v$ approaches the value 2γ for $\tau \to 0$, which is in accordance with

the result for an Ornstein-Uhlenbeck process (Eq. (2.11)). In the high correlation limit ($\tau \to \infty$) $\Delta\omega_v$ decays towards zero with τ^{-1} as the asymptotic behaviour. In Fig. 2.3, the full width at half maximum (Eq. (2.28b)) is presented as a function of τ for different values of γ. We observe that for large values of τ the results for the three different cases of γ coincide.

The presented model Eq. (2.12) is one of the few examples in which it is possible to find exact analytical results despite the violation of detailed balance. Another similar linear model, which is tractable analytically, is the case of Brownian motion in a harmonic potential driven by coloured noise, see [52]. The same process with Gaussian white noise instead of the coloured noise is also known as Kramer's equation in the literature [38]. In general, however, exact analytical results in systems without detailed balance are difficult to find. Therefore, we often need to rely on numerical simulations or appropriate approximation schemes, see Sec. 2.2.

2.2 Unified coloured noise approximation

In this section, we want to provide an approximation scheme that enables us to obtain analytical expressions for models with coloured Gaussian noise. In this thesis we will only consider the so-called unified coloured noise approximation developed by Jung and Hänggi [55]. This particular approximation is simple to apply, enables direct analytical computations and overcomes many of the shortcomings of other approaches (e.g. restriction to small parameter ranges); see [47] for a detailed discussion. In the following, we recall the steps of this method along the lines of [55].

Consider the following one-dimensional stochastic differential equation

$$\dot{x}(t) = -f(x) + \eta(t) \tag{2.29}$$

where $f(x)$ denotes a drift, which can be nonlinear in x, and η describes the coloured noise with an exponential correlation $\langle \eta(t)\eta(s)\rangle = \frac{1}{2\tau} \exp\left(-\frac{|t-s|}{\tau}\right)$. This equation describes, as already seen in the previous section, a non-Markov process due to the correlation time of the noise. The equivalent two-dimensional systems reads,

similarly to Eqs. (2.15a) and (2.15b)

$$\dot{x}(t) = -f(x) + \eta(t), \tag{2.30a}$$

$$\dot{\eta}(t) = -\frac{\eta(t)}{\tau} + \frac{\xi(t)}{\tau}, \tag{2.30b}$$

where $\xi(t)$ is Gaussian white noise. As already mentioned in the previous section, in general, it is not possible to solve the Fokker-Planck equation corresponding to Eqs. (2.30a) and (2.30b), although we are dealing with a Markov process now. Therefore, we proceed by applying the approximation scheme that we have already mentioned above. Differentiating with respect to t in Eq. (2.30a) and using Eq. (2.30b) to eliminate $\eta(t)$ yields

$$\ddot{x}(t) + \dot{x}(t)\left(\frac{1}{\tau} + f'(x(t))\right) = -\frac{f(x(t))}{\tau} + \frac{\xi(t)}{\tau}. \tag{2.31}$$

Here $f'(x(t))$ denotes the derivative of $f(x(t))$ with respect to $x(t)$. We introduce a new timescale $\hat{t} = \tau^{-1/2}t$ taking into account the correlation time of the noise

$$\frac{\ddot{x}(\hat{t})}{\tau} + \frac{\dot{x}(\hat{t})}{\sqrt{\tau}}\left(\frac{1}{\tau} + f'(x(\hat{t}))\right) = -\frac{f(x(\hat{t}))}{\tau} + \frac{\xi(\hat{t})}{\tau^{5/4}}. \tag{2.32}$$

By rearranging, we get

$$\ddot{x}(\hat{t}) + \dot{x}(\hat{t})\beta(x(\hat{t}), \tau) = -f(x(\hat{t})) + \frac{\xi(\hat{t})}{\tau^{1/4}} \tag{2.33}$$

where we have introduced the damping factor

$$\beta(x(\hat{t}), \tau) = \left(\frac{1}{\sqrt{\tau}} + \sqrt{\tau} f'(x(\hat{t}))\right). \tag{2.34}$$

If we have $f'(x) > 0$, $\beta(x(\hat{t}), \tau)$ approaches infinity for $\tau \to 0$ (no correlation) and $\tau \to \infty$ (high correlation regime). Therefore, we can apply adiabatic elimination procedures (neglecting fast variables) when the condition $\beta(x, \tau) \gg 1$ applies; under this condition we are dealing with a quasi-overdamped system. Thus, we proceed by neglecting the $\ddot{x}(\hat{t})$ term in Eq. (2.33), which gives us the following multiplicative

stochastic process

$$\dot{x}(\hat{t}) = -\frac{f(x(\hat{t}))}{\beta(x(\hat{t}),\tau)} + \frac{\xi(\hat{t})}{\tau^{1/4}\beta(x(\hat{t}),\tau)}. \tag{2.35}$$

Thus, we have mapped a non-Markov process (Eq. (2.29)) to an effective Markov process (Eq. (2.35)).

Since we have arrived at a multiplicative stochastic process, we have to decide whether we will follow the Ito or Stratonovich interpretation. These two interpretations are equivalent and the underlying Langevin and Fokker-Planck equations differ only by a correction term for the drift [38]. In the original work involving the unified coloured noise approximation [55] and other related investigations [47], the Stratonovich interpretation has been chosen. Investigations of Horsthemke and Lefever, who considered Stratonovich calculus and coloured noise in the framework of a master equation [50], and the theorem of Wong and Zakai [101] indicate that the Stratonovich interpretation is chosen in the context of problems involving a coloured noise. The Wong-Zakai theorem states that if the white noise of a stochastic process is considered as a limit of a noise source with a small but non-zero correlation time, then the investigated process converges to a Stratonovich stochastic differential equation in the limit of vanishing correlation time. For example, if we consider the following system with a drift $f(x)$ and a variable-dependent diffusion $g(x)$

$$\dot{x}(t) = -f(x(t)) + g(x(t))\eta(t), \tag{2.36}$$

$$\dot{\eta}(t) = -\frac{\eta(t)}{\tau} + \frac{\xi(t)}{\tau}, \tag{2.37}$$

$x(t)$ satisfies the Stratonovich stochastic differential equation

$$\dot{x}(t) = -f(x(t)) + g(x(t))\xi(t) \tag{2.38}$$

in the limit $\tau \to 0$. A more recent discussion on the issue with Ito and Stratonovich can be found in [75]. As we follow along the lines of [55], we use the Stratonovich interpretation and therefore stick to normal calculus rules.

To derive the corresponding Fokker-Planck equation now, we recall the following expressions. Having a stochastic differential equation of the form

$$\dot{x}(t) = -A(x(t)) + B(x(t))\xi(t) \tag{2.39}$$

with a drift $A(x)$, a diffusion $B(x)$, which depends on the variable x and Gaussian white noise $\xi(t)$, we obtain the following Fokker-Planck equation (following the Stratonovich interpretation) [38]

$$\begin{aligned}\frac{\partial}{\partial t}P(x,t|x_0,0) &= \frac{\partial}{\partial x}\left[A(x)P(x,t|x_0,0)\right] + \frac{1}{2}\frac{\partial}{\partial x}\left[B(x)\frac{\partial}{\partial x}\left[B(x)P(x,t|x_0,0)\right]\right] \\ &= \frac{\partial}{\partial x}\left(A(x) + \frac{1}{2}B(x)\frac{\partial}{\partial x}[B(x)]\right)P(x,t|x_0,0) \\ &\quad + \frac{1}{2}\frac{\partial^2}{\partial x^2}\left[B^2(x)P(x,t|x_0,0)\right]. \end{aligned} \tag{2.40}$$

By inserting the corresponding expressions from Eq. (2.35) we end up with

$$\begin{aligned}\frac{\partial}{\partial t}P(x,t|x_0,0) &= \frac{\partial}{\partial x}\left(\frac{f(x)}{\beta(x,\tau)} - \frac{1}{2\sqrt{\tau}}\frac{\beta'(x,\tau)}{\beta^3(x,\tau)}\right)P(x,t|x_0,0) \\ &\quad + \frac{1}{2\sqrt{\tau}}\frac{\partial^2}{\partial x^2}\left(\frac{P(x,t|x_0,0)}{\beta^2(x,\tau)}\right). \end{aligned} \tag{2.41}$$

The stationary solution reads

$$\begin{aligned}P(x) &= N\exp\left(-2\int f(x)dx\right)\exp\left(-\tau f^2(x)\right)|1+\tau f'(x)| \\ &= NP_{\tau=0}(x)\exp\left(-\tau f^2(x)\right)|1+\tau f'(x)|. \end{aligned} \tag{2.42}$$

Eq. (2.42) shows that for $\tau \neq 0$ two correction terms enter the expression for the stationary distribution. In the limit $\tau \to 0$ we arrive again at the result for white noise, represented by $P_{\tau=0}(x)$ in Eq. (2.42). This approximation scheme is expected to give excellent results in the limits $\tau \to 0$ and $\tau \to \infty$, and for intermediate values of τ it is supposed to be a useful approximation. Deviations will be expected if the condition $\beta(x,\tau) \gg 1$ does not hold. This approximation can be extended to multiplicative stochastic processes subjected to coloured noise.

To illustrate this method, we apply this approximation to the Ornstein-Uhlenbeck process driven by coloured noise, see Eqs. (2.12) and (2.14), and we obtain

$$\dot{v}(t) = -\frac{v(t)}{\frac{1}{\sqrt{\tau}} + \sqrt{\tau}\gamma} + \frac{\xi(t)}{\tau^{1/4}\left(\frac{1}{\sqrt{\tau}} + \sqrt{\tau}\gamma\right)}. \tag{2.43}$$

As we have a linear drift function, i.e. γv, this stochastic process remains additive.

The stationary probability distribution reads (see Eq. (2.42))

$$\begin{aligned} P(v) &= N^{-1} \exp\left(-\gamma v^2\right) \exp\left(-\tau\gamma^2 v^2\right) (1+\gamma\tau) \\ &= \sqrt{\frac{\gamma\,(\gamma\tau+1)}{\pi}} \exp\left(-\gamma\,(\gamma\tau+1)\,v^2\right). \end{aligned} \tag{2.44}$$

This result coincides with the previously found expression (Eq. (2.22)). Thus, the approximation reproduces the exact result for the linear drift in v.

In [65], the authors generalised the unified coloured noise approximation to higher dimensional systems and applied it in the context of active particles. Furthermore, an extension of this method to problems with coloured Poisson noise has been suggested in [64].

2.3 Fokker-Planck approach to Brownian motion with dry friction

The problem of Brownian motion with additional dry friction can be solved to a large extent analytically by investigating the corresponding Fokker-Planck equation. In this section we recall the main calculations and results from [94].
We have a Langevin equation of the form

$$\dot{v}(t) = -A(v) + \xi(t), \tag{2.45}$$

where $A(v)$ is now a piecewise-smooth function. The corresponding Fokker-Planck equation is, in non-dimensional units (see Apps. B.3 - B.5),

$$\frac{\partial}{\partial t} P(v,t|v_0,0) = \frac{\partial}{\partial v} A(v) P(v,t|v_0,0) + \frac{\partial^2}{\partial v^2} P(v,t|v_0,0). \tag{2.46}$$

The stationary distribution is given by

$$P(v) = M^{-1} \exp\left(-\int A(v)dv\right) \tag{2.47}$$

with the normalisation constant

$$M = \int_{-\infty}^{\infty} \exp\left(-\int A(v)dv\right) dv. \tag{2.48}$$

In order to solve the time-dependent problem, we introduce the following separation ansatz for the propagator [82]

$$P(v,t) = \exp(-\Lambda t) u_\Lambda(v). \tag{2.49}$$

$u_\Lambda(v)$ and Λ are the corresponding eigenfunction and eigenvalue of the Fokker-Planck operator L_{FP} and we have the following eigenvalue equation

$$\begin{aligned} -\Lambda u_\Lambda(v) &= L_{FP} u_\Lambda(v) \\ &= \left(\frac{\partial}{\partial v} A(v) + \frac{\partial^2}{\partial^2 v}\right) u_\Lambda(v), \quad \Lambda \geq 0. \end{aligned} \tag{2.50}$$

Since the Fokker-Planck operator is not Hermitian because of the first derivative in Eq. (2.50), we have to take the adjoint problem into account as well

$$\begin{aligned} -\Lambda w_\Lambda(v) &= L_{FP}^\dagger w_\Lambda(v) \\ &= \left(-A(v)\frac{\partial}{\partial v} + \frac{\partial^2}{\partial^2 v}\right) w_\Lambda(v). \end{aligned} \tag{2.51}$$

$L_{FP}^\dagger$ denotes the adjoint operator of the Fokker-Planck operator L_{FP}. The eigenfunctions $u_\Lambda(v)$ are related to the eigenfunctions of the adjoint problem $w_\Lambda(v)$ via the stationary distribution

$$u_\Lambda(v) = w_\Lambda(v) \exp\left(-\int A(v)dv\right). \tag{2.52}$$

This relation arises from the symmetrization of the Fokker-Planck operator to transform it into a Hermitian operator L [82]

$$L = [P(v)]^{1/2} L_{FP} [P(v)]^{-1/2}, \tag{2.53}$$

where $P(v)$ denotes the stationary distribution (Eq. (2.47)). The two eigenfunctions

form a bi-orthogonal system

$$\int_{-\infty}^{\infty} u_\Lambda(v) w_{\Lambda'}(v) = \delta_{\Lambda\Lambda'}. \tag{2.54}$$

Since the duality of L_{FP} and its corresponding adjoint operator $L_{FP}^\dagger$ is equivalent to perform integration by parts, the following boundary conditions for the eigenfunctions can be found

$$u_\Lambda(v) w_\Lambda(v) \xrightarrow{|v|\to\infty} 0. \tag{2.55}$$

Thus, it necessary to check that not only the eigenfunction $u_\Lambda(v)$ fulfils the boundary conditions but the product of the two eigenfunctions does.

Since Eq. (2.46) is linear in $P(v,t|v_0,0)$ the general expression for the propagator reads (in the case of a discrete spectrum)

$$P(v,t|v_0,0) = \sum_\Lambda \frac{\exp(-\Lambda t)\, u_\Lambda(v) w_\Lambda(v_0)}{M_\Lambda} \tag{2.56}$$

where M_Λ denotes the normalisation factor

$$M_\Lambda = \int_{-\infty}^{\infty} u_\Lambda(v) w_\Lambda(v) dv. \tag{2.57}$$

Whether the underlying eigenvalue spectrum is purely discrete or not can be clarified via Elliott's theorem [50].

Since we are dealing with a piecewise-smooth problem, we first have to solve Eq. (2.50) for the positive and negative domain separately. Then we match these solutions at the origin, where we impose the continuity of the eigenfunctions and the probability current, which results in the following two conditions

$$u_\Lambda(0-) = u_\Lambda(0+), \tag{2.58a}$$

$$A(0-)u_\Lambda(0-) + \frac{\partial}{\partial v} u_\Lambda(v)\bigg|_{v=0-} = A(0+)u_\Lambda(0+) + \frac{\partial}{\partial v} u_\Lambda(v)\bigg|_{v=0+}. \tag{2.58b}$$

After these more general aspects, we consider several drift functions for $A(v)$ and apply the methods presented above. The case of pure dry friction

$$A(v) = \sigma(v) \tag{2.59}$$

represents the dynamics of a particle in a symmetric wedge potential. The corresponding Fokker-Planck operator exhibits a spectral gap and continuous spectrum [82]. Results for the propagator, which is available as an exact analytical expression, and the stationary probability distribution are shown in Sec. 1.1, see Eqs. (1.9) and (1.11); a detailed derivation can be found in [94].

Next, we consider the case with dry and viscous friction

$$A(v) = v + \mu\sigma(v), \tag{2.60}$$

where μ is the rescaled dry friction coefficient (see App. B.4). The eigenfunctions can be even or odd because of the symmetric potential. Therefore, it is sufficient to investigate the problem for non-negative velocities by imposing appropriate boundary conditions at the origin ($v = 0$) in accordance with Eqs. (2.58a) and (2.58b). For the drift in Eq. (2.60) these conditions are

$$u_\Lambda^{(o)}(0) = 0, \tag{2.61a}$$

$$\mu u_\Lambda^{(e)}(0) + \frac{\partial}{\partial v} u_\Lambda^{(e)}(v)\bigg|_{v=0} = 0, \tag{2.61b}$$

where $u_\Lambda^{(e)}(v)$ denotes the even eigenfunction and $u_\Lambda^{(o)}(v)$ the odd counterpart. With the drift function from Eq. (2.60), the eigenvalue equation (Eq. (2.50) becomes

$$\frac{\partial^2}{\partial v^2} u_\Lambda(v) + \frac{\partial}{\partial v}[(v+\mu)u_\Lambda(v)] + \Lambda u_\Lambda(v) = 0, \quad v > 0. \tag{2.62}$$

To find a solution, we apply the transformation

$$u_\Lambda(v) = \exp\left(-\frac{(v+\mu)^2}{4}\right) y_\Lambda(v) \tag{2.63}$$

and arrive at

$$\frac{\partial^2}{\partial v^2} y_\Lambda(v) + \left(\frac{1}{2} - \frac{(v+\mu)^2}{4} + \Lambda\right) y_\Lambda(v) = 0. \tag{2.64}$$

This equation is known as the Weber equation and can be solved by the following ansatz

$$y_\Lambda(v) = A_1 D_\Lambda(v+\mu) + A_2 D_\Lambda(-(v+\mu)). \tag{2.65}$$

$D_\Lambda(v+\mu)$ is the parabolic cylinder function (see App. C.1) and A_1, A_2 are coeffi-

cients. We need to choose the solution which decays at infinity $v \to \infty$. Due to the asymptotic behaviour of the parabolic cylinder function (see App. C.1) we choose $A_1 = 1$ and $A_2 = 0$. Thus, the expression for our eigenfunction $u_\Lambda(v)$ is

$$u_\Lambda(v) = \exp\left(-\frac{(v+\mu)^2}{4}\right) D_\Lambda(v+\mu). \tag{2.66}$$

To take the boundary conditions at the origin into account, we insert the result from Eq. (2.66) into Eqs. (2.61a) and (2.61b) and by using an identity for parabolic cylinder functions (Eq. (C.4b)), we arrive at the following characteristic equations for the odd and the even eigenvalues

$$D_{\Lambda_n^{(o)}}(\mu) = 0, \tag{2.67a}$$

$$\Lambda_n^{(e)} D_{\Lambda_n^{(e)}-1}(\mu) = 0. \tag{2.67b}$$

This result indicates that the odd and even eigenvalues are related via

$$\Lambda_n^{(e)} = \Lambda_n^{(o)} + 1. \tag{2.68}$$

The characteristic equations (Eqs. (2.67a) and (2.67b)) have to be solved numerically. In Fig. 2.4, odd and even eigenvalues from Eqs. (2.67a) and (2.67b) are shown as a function of the dry friction coefficient μ. For increasing dry friction the non-vanishing eigenvalues also increase, whereas the eigenvalue $\Lambda_0 = 0$ obviously does not change. The relation between the odd and even eigenvalues (Eq. (2.68)) is clearly visible. A further analysis for eigenvalues with large indices for large values of μ can be found in [94], where asymptotic properties of the parabolic cylinder functions are used to obtain analytical expressions for the eigenvalues. Finally, the spectral representation of the full propagator reads

$$\begin{aligned} P(v,t|v_0,0) &= P(v) + \sum_{n=1}^{\infty} \exp\left(-\Lambda_n^{(o)} t\right) \frac{u_n^{(o)}(v) w_n^{(o)}(v_0)}{M_n^{(o)}} \\ &\quad + \sum_{n=1}^{\infty} \exp\left(-\Lambda_n^{(e)} t\right) \frac{u_n^{(e)}(v) w_n^{(e)}(v_0)}{M_n^{(e)}}, \end{aligned} \tag{2.69}$$

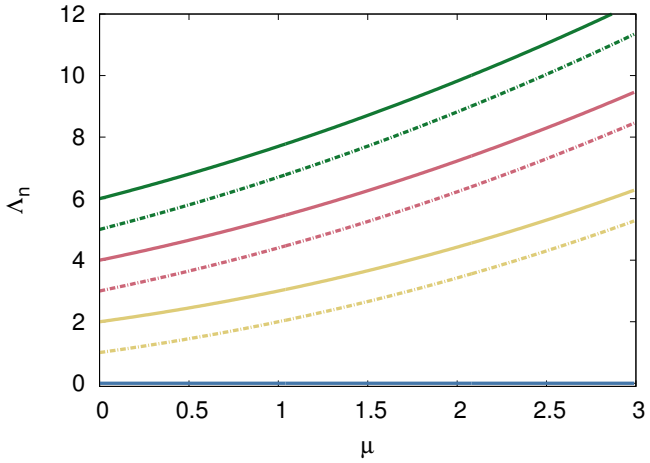

Figure 2.4: Eigenvalues for the case of dry and viscous friction (Eq. (2.60)), obtained numerically from Eqs. (2.67a) and (2.67b). The dot-dashed line and the solid line represent the odd and the even eigenvalues respectively for $n = 1$ (yellow), $n = 2$ (red), $n = 3$ (green). The blue solid line denotes the vanishing eigenvalue $\Lambda_0 = 0$.

where

$$P(v) = M_0^{-1} \exp\left(-\frac{(|v| + \mu)^2}{2}\right) \tag{2.70}$$

is the stationary solution. M_0, $M_n^{(o)}$, $M_n^{(e)}$ denote the respective normalisation constants (see Eqs. (2.48) and (2.57)).

For the case without dry friction $\mu = 0$, the drift function in Eq. (2.60) only contains the viscous friction and the resulting potential becomes quadratic. Then we arrive at the problem of the Ornstein-Uhlenbeck process. The eigenvalues become odd and even integers, see Fig. 2.4 for $\mu = 0$. Despite the absence of the dry friction, Eq. (2.68) still holds as a relation between odd end even eigenvalues. The parabolic cylinder functions can be represented via the Hermite polynomials as the indices become integers

$$D_n(v) = \exp\left(-\frac{v^2}{2}\right) \mathrm{He}_n(v). \tag{2.71}$$

The spectral representation of the propagator (Eq. (2.69)) can then be expressed in a closed analytical form by using Mehler's formula [31] and we arrive at the expression in Eq. (2.6) for $\gamma = 1$.

After discussing the case for two different types of friction, we extend our equa-

tions by a constant force. Thus, our drift function changes to

$$A(v) = v + \mu\sigma(v) - b, \tag{2.72}$$

where b denotes the constant force in non-dimensional units (see App. B.5). The eigenvalue equation (Eq. (2.50)) attains a similar form to Eq. (2.62)

$$\frac{\partial^2}{\partial^2 v} u_\Lambda(v) + \frac{\partial}{\partial v}[(v \pm \mu - b)u_\Lambda(v)] + \Lambda u_\Lambda(v) = 0, \quad v \gtrless 0. \tag{2.73}$$

Here, the $\pm$ signs denote the solution for the positive and negative domain respectively, as we can not classify the eigenfunctions according to their symmetry because of $b \neq 0$. We proceed as in Eqs. (2.63) - (2.66) and obtain the following expressions for the eigenfunction, which can again be written in terms of parabolic cylinder functions

$$u_\Lambda(v) = C_\pm \exp\left(-(v \pm \mu - b)^2/4\right) D_\Lambda(\pm v + \mu \mp b), \quad v \gtrless 0. \tag{2.74}$$

$C_\pm$ denote the coefficients for the respective half-space of v. The solution in Eq. (2.74) fulfils the boundary conditions at infinity. To check the matching conditions at the origin for our solutions (Eq. 2.74), we insert these expressions into the Eqs. (2.58a) and (2.58b) and by using an identity for parabolic cylinder functions (Eqs. (C.4b)) we get

$$C_- \exp\left(-(\mu + b)^2/4\right) D_\Lambda(\mu + b) = C_+ \exp\left(-(\mu - b)^2/4\right) D_\Lambda(\mu - b), \tag{2.75a}$$

$$C_- \Lambda \exp\left(-(\mu + b)^2/4\right) D_{\Lambda-1}(\mu + b) = -C_+ \Lambda \exp\left(-(\mu - b)^2/4\right) D_{\Lambda-1}(\mu - b). \tag{2.75b}$$

In order to have non-trivial solutions for $C_\pm$, these coefficients have to obey the following conditions

$$C_- = C_+ \frac{\exp\left(-(\mu - b)^2/4\right) D_\Lambda(\mu - b)}{\exp\left(-(\mu + b)^2/4\right) D_\Lambda(\mu + b)}, \tag{2.76a}$$

$$C_- = -C_+ \frac{\Lambda \exp\left(-(\mu - b)^2/4\right) D_{\Lambda-1}(\mu - b)}{\Lambda \exp\left(-(\mu + b)^2/4\right) D_{\Lambda-1}(\mu + b)}. \tag{2.76b}$$

We can derive from the above equations the following characteristic equation for the

eigenvalues Λ_n

$$\Lambda_n \left[D_{\Lambda_n}(\mu + b) D_{\Lambda_n - 1}(\mu - b) + D_{\Lambda_n}(\mu - b) D_{\Lambda_n - 1}(\mu + b) \right] = 0. \tag{2.77}$$

Fig. 2.5 shows the results for the first five non-vanishing eigenvalues from Eq. (2.77) as a function of the constant force b and for a fixed value of μ. We can observe that the eigenvalues decrease for high values of b. For $b > \mu$, the sliding motion is dominating the dynamics and therefore, the lower part of the spectrum attains an Ornstein-Uhlenbeck like spectrum where the eigenvalues are integers. For example the eigenvalues Λ_1 and Λ_2 approach the values 1 and 2 respectively, as we can see in Fig. 2.5. Furthermore, the distances between consecutive eigenvalues do not stay constant by varying b in comparison to the odd and even eigenvalues for the case without constant force (see Eq. (2.68)).

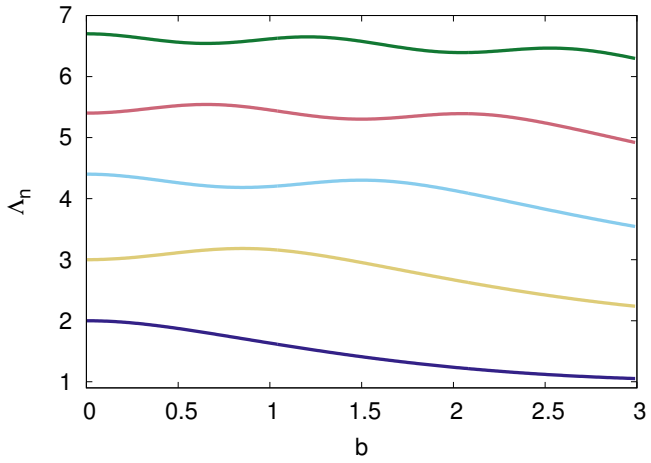

Figure 2.5: First non-vanishing eigenvalues, obtained numerically from Eq. (2.77) with $\mu = 1$. Λ_1 (blue), Λ_2 (yellow), Λ_3 (cyan), Λ_4 (red), Λ_5 (green).

Finally, the full propagator reads, similarly to Eq. (2.69)

$$P(v, t|v_0, 0) = P(v) + \sum_{n=1}^{\infty} \exp\left(-\Lambda_n t\right) \frac{u_n(v) w_n(v_0)}{M_n}. \tag{2.78}$$

The stationary solution is

$$P(v) = M_0^{-1} \exp\left(- \left(\frac{(|v| + \mu)^2}{2} - bv \right) \right). \tag{2.79}$$

Further details and results can be found in [94].

2.4 Filippov systems with noise

Here, we want to elaborate further the connection between the investigations of this thesis and the theory of piecewise-smooth dynamical systems, in particular Filippov systems. Therefore, we start by revising some definitions and concepts from [28]. Given an ordinary differential equation

$$\dot{x}(t) = F(x(t)) \tag{2.80}$$

with the smooth vector field $F(x(t))$, we have the flow $\Phi(x,t) = x(t)$, which describes the state of the system at time t, starting from the initial condition at $t = 0$. Thus, we find for the flow

$$\frac{\partial}{\partial t}\Phi(x,t) = F(\Phi(x,t)), \quad \Phi(x,0) = x(0). \tag{2.81}$$

Similarly, in the framework of piecewise-smooth dynamical systems one defines a piecewise-smooth flow, which is given by a finite set of ordinary differential equations

$$\dot{x}(t) = F_i(x(t)), \quad \text{for} \quad x(t) \in S_i, \tag{2.82}$$

where S_i denotes the respective region of x and we have $\bigcup_i S_i \subset \mathbb{R}^n$. Each vector field $F_i(x(t))$ is smooth and defines a smooth flow $\Phi_i(x,t)$ (see Eq. (2.81)). The non-empty intersection between the particular regimes (i.e. the intersection of the closures of the sets to be precise) is called discontinuity set or switching manifold. A further notion in this context is the degree of smoothness r at a point x_S on the switching manifold. It denotes the order of the Taylor series expansion of the flows $\Phi_i(x_S,t)$ and $\Phi_j(x_S,t)$ with respect to t, evaluated at $t = 0$, at which the difference between the two expressions is non-zero, i.e.

$$\frac{\partial^r}{\partial t^r}\left[\Phi_i(x_S,t) - \Phi_j(x_S,t)\right]_{t=0} \neq 0. \tag{2.83}$$

Systems with a degree of smoothness equal $r = 1$ are known as Filippov systems. Prominent examples are friction oscillators or relay control systems (see [28]).

To give a short example for a Filippov system, which is similar to the used dry friction model in this thesis, we consider the following system

$$\dot{x}(t) = \begin{cases} F_1(x(t)) & \text{if } x \in S_1, \\ F_2(x(t)) & \text{if } x \in S_2. \end{cases} \tag{2.84}$$

S_1 and S_2 denote the respective region of x. $F_1(x(t))$ generates a flow $\Phi_1(x,t)$ and $F_2(x(t))$ a flow $\Phi_2(x,t)$. If we have $F_1(x_S) \neq F_2(x_S)$, or to express it in terms of the piecewise-smooth flow $\frac{\partial}{\partial t}\left[\Phi_1(x_S,t) - \Phi_2(x_S,t)\right]_{t=0} \neq 0$) on the switching manifold, the degree of smoothness is one and Eq. (2.84) therefore describes a Filippov system. For further details, see [28].

In [88–90], Filippov systems with noise have been investigated. A small noise amplitude had been choosen to underline the perturbative character of the noise. Analytical results in asymptotic limits have been obtained by using the WKB method [38]. The investigations focussed on the impact of Gaussian white noise to the sliding dynamics near a switching manifold and close to periodic orbits, which involve segments of the discontinuity of the vector field.

The investigations in this thesis build on the studies on Brownian motion and dry friction, i.e. mainly the work by Hayakawa [48], de Gennes [27], and Touchette et al. [94]. Here, the focus lies more on solving the underlying Fokker-Planck problem and computing correlation functions than investigating aspects of stochastic perturbations. As previously mentioned in Secs. 2.1 and 2.2, we replace the Gaussian white noise by an exponentially correlated noise, which is characterised by its correlation time τ and it is generated by an Ornstein-Uhlenbeck process. Our interest lies in the impact of the correlation time of the noise to the system with dry friction.

The above mentioned noisy Filippov systems could be investigated in a similar way by replacing the Gaussian white noise with an Ornstein-Uhlenbeck noise and studying the impact of the correlation time τ for example to the stochastically perturbed sliding motion near a switching manifold or how the different phases of stochastic dynamics in a relay control system are affected. In general, it will be interesting to see changes in the dynamics if we go from zero correlation (white noise limit) to the high correlation limit.

Chapter 3

Pure dry friction and coloured noise

In this chapter, we investigate the impact of coloured noise in a piecewise-smooth stochastic system, which contains only a dry friction term. Our main goal is to find the differences compared to the case of Gaussian white noise and to show the characteristics of such a model. This simple model is chosen to allow at least a partial analytical treatment of the problem as it is the simplest case of a piecewise-smooth stochastic system without detailed balance.

This chapter is structured as follows. First, we introduce our dynamical equations and provide numerical results for the time series to show the main characteristics of our model. Section 3.2 focuses on finding analytical expressions for the marginal stationary distribution of the velocity v and the joint probability distribution of the velocity v and the noise η. An approximate expression for the marginal distribution $P(v)$ can be derived by using the unified coloured noise approximation. The stationary probability current is computed numerically to show the nonequilibrium character of our system. Furthermore, we investigate the dynamical properties of our model in Sec. 3.3. The power spectral density for the velocity is computed to investigate the impact of the noise correlation time τ on the correlations of the velocity v. Furthermore, we examine the sticking and sliding events and calculate their distributions. While the latter can only be found numerically, it is possible to use a semi-analytical approach for the sticking time distribution via the exit time problem for an Ornstein-Uhlenbeck process.

Finally, we summarise our findings in Sec. 3.4. The content of this chapter is published in [39].

3.1 The piecewise-smooth model

In Section 1.1, analytical results have been presented for the dynamics of particle, which are modelled by using a one-dimensional piecewise-smooth stochastic differential equation subjected to Gaussian white noise. The corresponding Fokker-Planck equation with suitable matching conditions ensuring continuity of the probability distribution and the probability current captures all aspects of the dynamics and has been studied intensely in the literature, see e.g. [27]. For the case of pure dry friction, it is possible to find an exact result for the time-dependent propagator [94] (see Sec. 1.1 as well).

An extension of this pure dry friction model subjected to Gaussian white noise, leading towards a two-dimensional stochastic nonequilibrium system, consists in studying the effect of coloured noise. We therefore replace the Gaussian white noise by an exponentially correlated Ornstein-Uhlenbeck noise, which is governed by the stochastic differential equation

$$\dot{\eta}(t) = -\frac{\eta(t)}{\tau} + \frac{\xi(t)}{\tau}. \tag{3.1}$$

Here, we have already rescaled the variables in our system and the noise correlation time τ remains the only effective parameter (see App. B.6). Since the process $\eta(t)$ can be viewed as a continuous function with a finite amplitude, some care is needed when introducing the dynamics of the particle. For forces smaller than the dry friction coefficient, $|\eta| < 1$, and $v = 0$ the particle will stick while otherwise we will observe sliding dynamics. Thus, we end up with the following equation

$$\dot{v}(t) = \begin{cases} 0 & \text{if } v = 0 \text{ and } |\eta(t)| < 1, \\ -\sigma_0(v(t)) + \eta(t) & \text{otherwise,} \end{cases} \tag{3.2}$$

with $\sigma_0(v(t)) = \sigma(v(t)) = \mathrm{sgn}(v)$. Alternatively we could use a regularized drift

$$\dot{v}(t) = -\sigma_\varepsilon(v(t)) + \eta(t) \tag{3.3}$$

and consider results in the limit $\varepsilon \to 0$; a candidate for this smoothed drift function could be

$$\sigma_\varepsilon(v(t)) = \tanh\left(\frac{v(t)}{\varepsilon}\right). \tag{3.4}$$

We will adopt both views throughout our exposition while we will, at the same time, avoid the considerable technical difficulties that would be related with a rigorous approach. Since we consider a noise with finite correlation time but a damping which does not involve a memory kernel, the system violates detailed balance and describes a nonequilibrium process [63]. On the contrary, the model in the white noise limit has a vanishing stationary probability current and describes a process in equilibrium (see Sec. 1.1).

For the model defined by Eq. (3.2) the static friction equals the kinetic friction. In real world the former exceeds the latter, and our assumption has to be considered as an idealisation from an experimental perspective. Our particular choice does not include any hysteresis, but it has the advantage that the piecewise-smooth dynamical system can be captured as a singular limit of the smooth dynamics Eq. (3.3). Above all the model captures stick-slip phenomena which will be a key ingredient of our analysis.

Before we enter a more detailed discussion let us just illustrate the main phenomenon by time traces obtained from numerical simulations. Throughout all our numerical investigations we apply an Euler-Maruyama scheme (see App. A for details) with step size $h = 10^{-3}$ for different values of τ. To take the discontinuity caused by dry friction into account (see Eq. (3.2)) we set $v = 0$ for $|v| < 10^{-3}$ and $|\eta| < 1$, as the particle sticks in this case at the origin. Time traces from the simulations are shown in Figs. 3.1 - 3.3.

For white noise, we can observe a random motion of the velocity (Fig. 3.1). For a numerical realisation of the Gaussian white noise the correlation time of the noise is made equal to the stepsize of the numerical integration. The effect of dry friction becomes visible for correlation times larger than $\tau = 0.1$. The particle sticks for considerable amounts of time at $v = 0$, as the stochastic force $\eta(t)$ is not large enough to move the particle, see Fig. 3.3. For Gaussian white noise, which has infinite variance, no sticking events can be observed since its amplitude is always larger than the dry friction coefficient [27]. Nevertheless, the interest in studying the dynamics of systems with dry friction and Gaussian white noise has

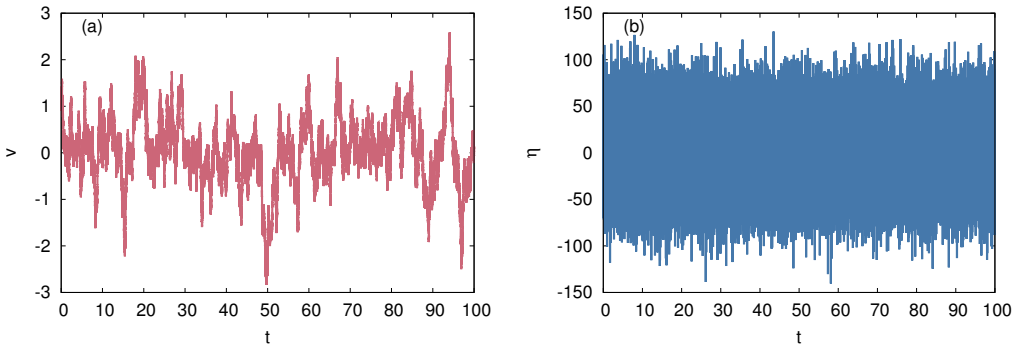

Figure 3.1: Time traces of the velocity $v(t)$ (a) and the Ornstein-Uhlenbeck noise $\eta(t)$ (b) of the dry friction model (Eqs. (3.1) and (3.2)) for $\tau = 0.001$.

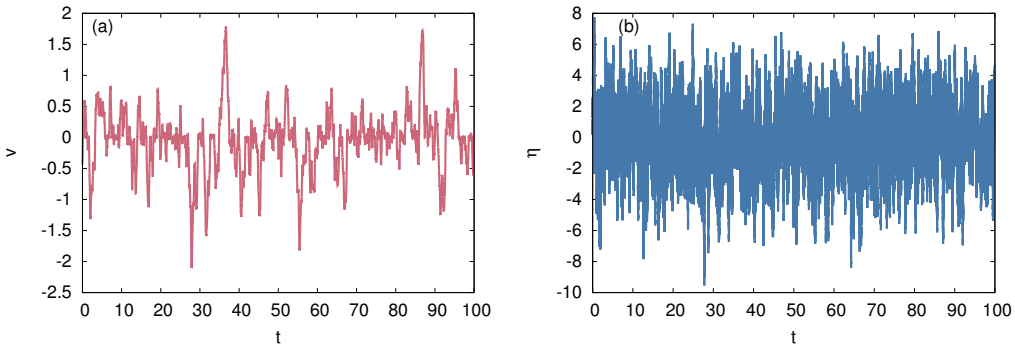

Figure 3.2: Time traces of the velocity $v(t)$ (a) and the Ornstein-Uhlenbeck noise $\eta(t)$ (b) of the dry friction model (Eqs. (3.1) and (3.2)) for $\tau = 0.1$.

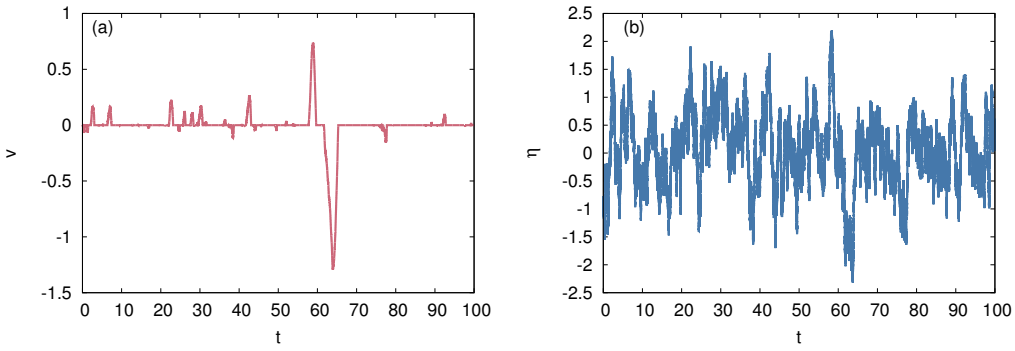

Figure 3.3: Time traces of the velocity $v(t)$ (a) and the Ornstein-Uhlenbeck noise $\eta(t)$ (b) of the dry friction model (Eqs. (3.1) and (3.2)) for $\tau = 1.0$.

been motivated by signatures of stick-slip motion, i.e. the cusp of the stationary probability distribution (see Eq. (1.11)) or stick-slip transitions, which are visible in the correlation function and the power spectral density [94, 95]. The observed stick-slip phenomenona and the related intermittent motion will be at the centre of our studies, being the key signature of our piecewise-smooth stochastic model with coloured noise.

3.2 Stationary distribution

Figure 3.3 exhibits stick-slip dynamics for a high correlation time of the noise, whereas we observe a random motion of the velocity for smaller correlation times (Fig. 3.2) and for the case with white noise (Fig. 3.1). Given these results from the time traces we expect the stationary probability distribution of the velocity to exhibit a singular component for high correlation times, which reflects the fact that the particle is sticking at $v = 0$. Thus, the corresponding stationary distribution is expected to consist of two contributions: a Dirac δ component at vanishing velocities and $|\eta| < 1$, and a regular part describing moving particles with finite velocities. The analysis will be further hampered by the lack of detailed balance so that closed-form analytic expressions are unlikely to be available.

3.2.1 Marginal distribution and unified coloured noise approximation

To make some analytical headway let us first have a look at the marginal velocity distribution

$$P(v) = \int_{-\infty}^{\infty} P(v, \eta) d\eta. \tag{3.5}$$

We are interested in possible differences compared with the white noise case (see e.g. Sec. 1.1 and [94]). We apply the unified coloured noise approximation (UCNA) (see Sec. 2.2 for details) to our system (Eqs. (3.1) and (3.3)). Here we use the smoothed version of the dry friction (Eq. (3.4)) to avoid technical difficulties with the discontinuous drift and its derivative. In the end we will consider the results in

the limit $\varepsilon \to 0$. We obtain the following multiplicative stochastic process

$$\dot{v}(\hat{t}) = -\frac{\sigma_\varepsilon(v(\hat{t}))}{\beta(v(\hat{t}),\tau)} + \frac{\xi(\hat{t})}{\tau^{1/4}\beta(v(\hat{t}),\tau)} \tag{3.6}$$

with

$$\beta(v(\hat{t}),\tau) = \tau^{-1/2} + \tau^{1/2}\sigma'_\varepsilon(v(\hat{t})), \tag{3.7}$$

and $\hat{t} = \tau^{-1/2}t$ denotes the new time scale which takes the correlation time of the noise into account. By using the Stratonovich interpretation (see discussion in Sec. 2.2 on the issue of the interpretation) the corresponding Fokker-Planck equation for the propagator $P(v,\hat{t}|v_0,0)$ reads

$$\begin{aligned}\frac{\partial}{\partial\hat{t}}P(v,\hat{t}|v_0,0) &= \frac{\partial}{\partial v}\left(\frac{\sigma_\varepsilon(v)}{\beta(v,\tau)} - \frac{1}{2\tau^{1/2}}\frac{\beta'(v,\tau)}{\beta^3(v,\tau)}\right)P(v,\hat{t}|v_0,0) \\ &\quad + \frac{1}{2\tau^{1/2}}\frac{\partial^2}{\partial v^2}\frac{P(v,\hat{t}|v_0,0)}{\beta^2(v,\tau)}.\end{aligned} \tag{3.8}$$

Since we have reduced the problem to a one-dimensional Fokker Planck equation the stationary distribution can be computed by straightforward integration

$$P(v) = N^{-1}\exp\left(-2\int\sigma_\varepsilon(v)dv - \tau\sigma_\varepsilon^2(v) + \ln\left(|1+\tau\sigma'_\varepsilon(v)|\right)\right). \tag{3.9}$$

We can observe that due to the correlation time of the noise two correction terms enter the expression, as already seen in Sec. 2.2 (Eq. (2.42)). In the dry friction limit $\varepsilon \to 0$, the contributions of Eq. (3.9) become

$$\sigma_0(v) = \mathrm{sgn}(v),\ \int\sigma_0(v)dv = |v|,\ \sigma'_0(v) \sim \delta(v). \tag{3.10}$$

Eq. (3.10) indicates that the probability distribution (Eq. (3.9)) consists of two parts in the dry friction limit: a regular part, which describes the sliding dynamics for $v \neq 0$ and a singular part, which contains the Dirac δ function reflecting the sticking phenomena with $v = 0$ when the stochastic force is not large enough to move the particle. In the following, we consider the two parts separately.

For the calculation of the normalisation constant N, we have

$$\begin{aligned} N &= \int_{-\infty}^{\infty} \exp\left(-2\int \sigma_\varepsilon(v)dv - \tau\sigma_\varepsilon^2(v) + \ln\left(|1+\tau\sigma_\varepsilon'(v)|\right)\right) dv \\ &= \underbrace{\int_{-\infty}^{\infty} \exp\left(-2\int \sigma_\varepsilon(v)dv - \tau\sigma_\varepsilon^2(v)\right) dv}_{N_{Reg}} \\ &\quad + \underbrace{\int_{-\infty}^{\infty} \exp\left(-2\int \sigma_\varepsilon(v)dv - \tau\sigma_\varepsilon^2(v)\right) \tau\sigma_\varepsilon'(v)dv}_{N_{Sing}} \\ &= N_{Reg} + N_{Sing} \end{aligned} \tag{3.11}$$

where N_{Reg} denotes the normalisation due to the regular part and N_{Sing} denotes the normalisation due to the singular part, which contains the term $\sigma_\varepsilon'(v)$. The first part of Eq. (3.11) reads in the dry friction limit (see Eq. (3.10))

$$\begin{aligned} N_{Reg} &= \int_{-\infty}^{\infty} \exp\left(-2|v| - \tau\sigma_0^2(v)\right) dv \\ &= \exp(-\tau). \end{aligned} \tag{3.12}$$

As we have a singular and a discontinuous contribution in the second term of Eq. (3.11), some care is needed and we proceed in a different way to compute the integral. Due to the $\sigma_\varepsilon'(v)$ term, which becomes the Dirac $\delta(v)$ function in the dry friction limit (Eq. (3.10)), we only have to consider the parts which give a nonzero contribution around $v = 0$

$$\begin{aligned} N_{Sing} &= \int_{-\infty}^{\infty} \exp\left(-\tau\sigma_\varepsilon^2(v)\right) \tau\sigma_\varepsilon'(v)dv \\ &= \int_{-\sqrt{\tau}}^{\sqrt{\tau}} \exp\left(-x^2\right) \sqrt{\tau}dx \\ &= \sqrt{\pi\tau}\mathrm{erf}(\sqrt{\tau}) \end{aligned} \tag{3.13}$$

where we have used the substitution $x = \sqrt{\tau}\sigma_\varepsilon(v)$ and the error function

$$\mathrm{erf}(z) = \frac{2}{\sqrt{\pi}} \int_0^z \exp(-y^2)dy. \tag{3.14}$$

Thus, the regular part of the stationary probability distribution reads

$$P_{Reg}(v) = \frac{\exp\left(-2|v| - \tau\sigma_0^2(v)\right)}{\exp\left(-\tau\right) + \sqrt{\pi\tau}\mathrm{erf}(\sqrt{\tau})}. \tag{3.15}$$

The accuracy of the perturbative approach can be confirmed by direct numerical simulations, see Figure 3.4 for the comparison of the UCNA with direct numerical simulations. For the numerical analysis, we again use the Euler-Maruyama scheme (see App. A) and sample the distribution with a resolution $\Delta v = 0.002$. By taking about 100 realisations of time traces of length $T = 10^4$, we observe good agreement for small correlation times. However, for values $\tau > 0.1$, deviations between numerics and analytics become visible. The largest discrepancy can be observed around the origin $v = 0$, as the analytical expression clearly underestimates the numerical result and does not correctly describe the transition from the regular part to the singular part. Although this is a shortcoming of the analytical approximation, it is not entirely clear why the deviations around the peak are the largest compared to the other parts of the distribution. Furthermore, for higher values of τ we observe a stronger decay of the tails and overall, the regular part of the distribution decreases.

In addition to the regular part (Eq. (3.15)), we consider the singular part of the probability distribution in Eq. (3.9). As already mentioned before, we only need to consider the terms which give a non zero contribution around $v = 0$. Therefore, we integrate in a small vicinity $[-a, a]$ around $v = 0$

$$\begin{aligned} \int_{-a}^{a} \exp\left(-\tau\sigma_\varepsilon^2(v)\right) \tau\sigma_\varepsilon'(v) dv &= \int_{-\sqrt{\tau}}^{\sqrt{\tau}} \exp\left(-x^2\right) \sqrt{\tau} dx \\ &= \sqrt{\pi\tau}\mathrm{erf}(\sqrt{\tau}) \end{aligned} \tag{3.16}$$

where we have used the same substitution as in Eq. (3.13). Thus, the singular part of the probability distribution is

$$P_{Sing}(v) = \frac{N_{Sing}}{N}\delta(v), \tag{3.17}$$

where $N = N_{Reg} + N_{Sing}$ is the normalisation constant (see Eqs. (3.11) - (3.13)). From this result we immediately obtain an estimate for the probability of sticking

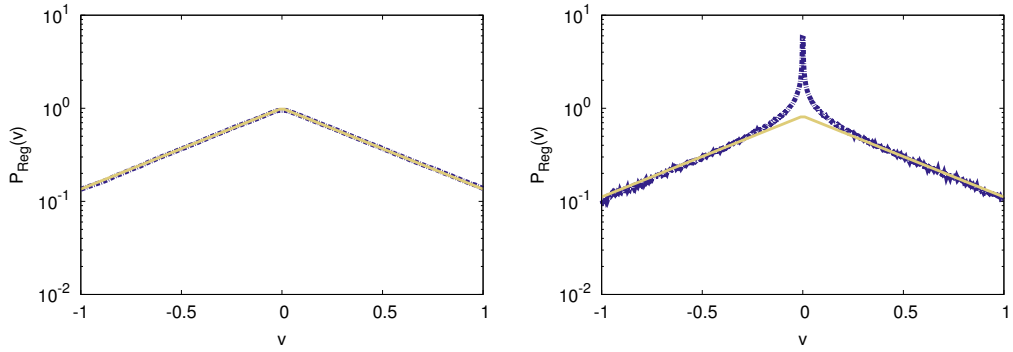

(a) $\tau = 0.0$ (b) $\tau = 0.1$

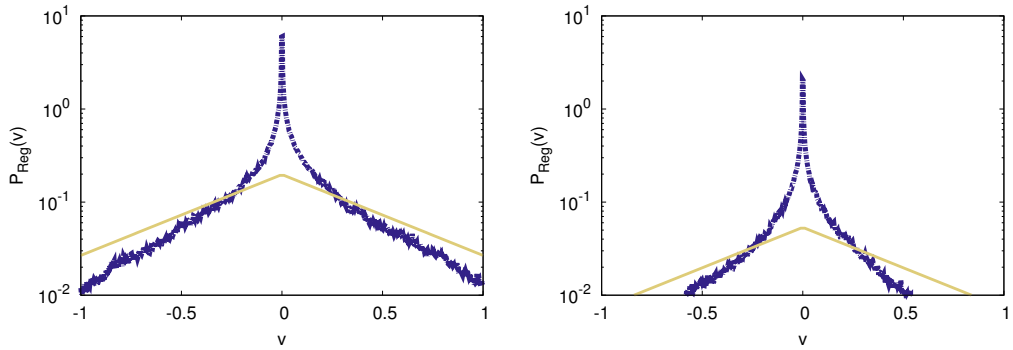

(c) $\tau = 1.0$ (d) $\tau = 2.0$

Figure 3.4: Regular part of the stationary distribution, i.e. distribution of the sliding events, obtained from numerical simulations (dashed lines) sampled as a histogram with resolution $\Delta v = 0.002$ and the analytical approximation, Eq. (3.15) (solid lines). Data have been displayed for different values of the correlation time $\tau = 0.0$ ($\tau = 0.001$ for the numerics) (a), $\tau = 0.1$ (b), $\tau = 1.0$ (c), $\tau = 2.0$ (d), cf. Figs. 3.1 - 3.3.

as a function of the noise correlation

$$P_{Stick}(\tau) = \frac{\sqrt{\pi\tau}\mathrm{erf}(\sqrt{\tau})}{\exp(-\tau) + \sqrt{\pi\tau}\mathrm{erf}(\sqrt{\tau})}. \tag{3.18}$$

Figure 3.5 shows the comparison of the analytical approximation with the simulations and we observe quite a good agreement, as the probability of sticking increases with increasing τ and approaches the value 1 in the limit of high correlation times. The differences between the two results, which are most visible in the intermediate range of the correlation time τ, seem to be a systematic overestimate from the approximation since different realisations of the numerical simulations give almost

identical outcomes. Therefore, the numerical results are presented without error bars.

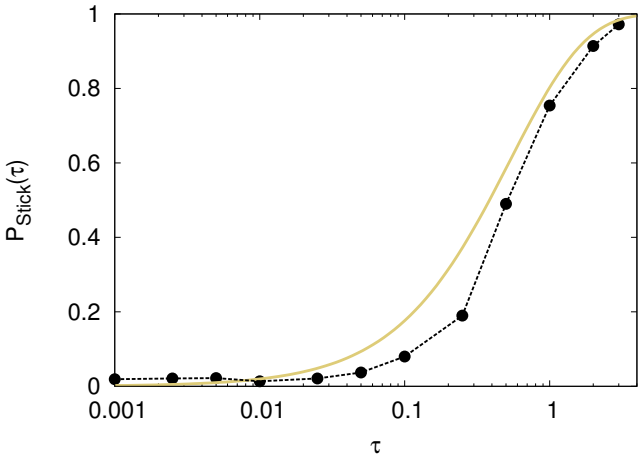

Figure 3.5: Probability of the sticking events as a function of the noise correlation time τ. The dots correspond to numerical simulations of Eqs. (3.1) and (3.2), the solid line corresponds to Eq. (3.18).

Taking the limit $\tau \to 0$, we see that we arrive at the stationary probability distribution for dry friction model subjected to Gaussian white noise as the corrections in Eq. (3.15) vanish and the expression in Eq. (3.17) becomes zero. For small correlation times of the noise, the sliding motion is dominating the dynamics. However, for high correlation times τ the sliding contribution decreases and the distribution is mainly determined by the delta peak. Thus, by increasing τ we observe a gradual transition from sliding to sticking motion. This can be understood by the fact that the probability of having $|\eta(t)| < 1$ increases (as the amplitude decreases for higher values of τ) and therefore it becomes more and more likely for the particle to stick.

Overall, the analytic approximation seems to work rather well, especially for small τ and also for high τ for P_{Stick}. Deviations become visible when the noise correlation time increases (see Fig. 3.4 for the case $\tau = 1.0$). To explain the deviations of the analytical approximation from the direct numerical simulations for the regular part, which represents the sliding events (Fig. 3.4), we need to take a look at the conditions of validity of the UCNA. This approximation agrees with numerical simulations for the case $\beta(v, \tau) \gg 1$. However, for higher values of τ, this approximation fails as in our case the contribution caused by the dry friction vanishes in

the limit $\varepsilon \to 0$, i.e., when considering the piecewise linear case. Nevertheless, this analytic approximation scheme provides very useful information of the underlying nonequilibrium dynamics of our model.

3.2.2 Joint probability distribution and probability current

To get more insight into the dynamics of our model, we study the two-dimensional equations of motion (3.1) and (3.2) with the aim of understanding the properties of the stationary probability distribution $P(v, \eta)$.

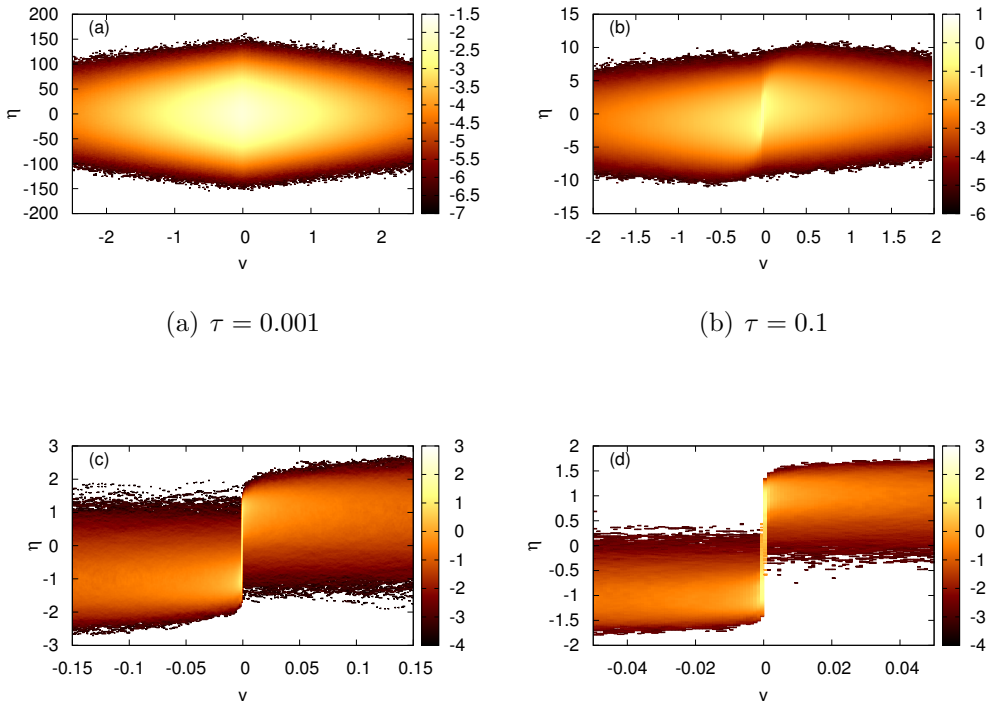

(a) $\tau = 0.001$ (b) $\tau = 0.1$

(c) $\tau = 1.0$ (d) $\tau = 2.0$

Figure 3.6: Logarithmic density plot of the joint stationary probability distribution, obtained from numerical simulations of Eqs. (3.1) and (3.2), for different values of the correlation time: $\tau = 0.001$ (a), $\tau = 0.1$ (b), $\tau = 1.0$ (c), $\tau = 2.0$ (d). The distribution has been sampled with a resolution of $\Delta v = 0.001$ and 300 bins in η-direction. Slices of the distribution at $v = 0$ can be found in Fig. 3.9.

To begin with we perform numerical simulations of the dynamics of Eqs. (3.1) and (3.2) (see App. A for details of the numerical integration scheme). Density plots

on a logarithmic scale of the full stationary distribution (regular and singular part) are shown in Fig. 3.6. For $\tau = 0.001$ the singular part hardly matters and results are almost indistinguishable from the white noise case within the resolution of our simulations. The regular distribution shows a Gaussian profile in the η direction as well as exponential decay in the v direction. By increasing τ, the distribution changes significantly as the singular part becomes noticeable (cf. Eq. (3.18) and Fig. 3.4). Furthermore, the regular part of the distribution becomes asymmetric as the two components in the half spaces $v > 0$ and $v < 0$ are relative to one another.

For further analytical insight we try to formulate the corresponding Fokker-Planck system. Using the regularized version of the equations of motion, Eqs. (3.1) and (3.3), the time-dependent Fokker-Planck equation reads

$$\frac{\partial}{\partial t}P(v,\eta,t|v_0,\eta_0,0) = \left[\frac{\partial}{\partial v}\left(\sigma_\varepsilon(v)-\eta\right) + \frac{\partial}{\partial \eta}\left(\frac{\eta}{\tau}+\frac{1}{2\tau^2}\frac{\partial}{\partial \eta}\right)\right] P(v,\eta,t|v_0,\eta_0,0)\,. \tag{3.19}$$

Since detailed balance is violated, it is difficult to find an exact solution for the stationary Fokker-Planck equation

$$\left[\frac{\partial}{\partial v}\left(\sigma_\varepsilon(v)-\eta\right) + \frac{\partial}{\partial \eta}\left(\frac{\eta}{\tau}+\frac{1}{2\tau^2}\frac{\partial}{\partial \eta}\right)\right] P(v,\eta) = 0\,. \tag{3.20}$$

Several different approaches to find an analytical solution for $P(v,\eta)$ were not successful. A Fourier transform of the velocity in Eq. (3.20) yields a convolution integral involving the smoothed dry friction and the probability distribution:

$$\mathcal{F}\left\{\frac{\partial}{\partial v}\sigma_\varepsilon(v)P(v,\eta)\right\} = -iq\left[\sigma_\varepsilon(q) * P(q,\eta)\right] \tag{3.21}$$

with

$$\left[\sigma_\varepsilon(q) * P(q,\eta)\right] = \int_{-\infty}^{\infty}\sigma_\varepsilon(q-h)P(h,\eta)dh. \tag{3.22}$$

Thus, Eq. (3.20) changes to an integro-differential equation for $P(q,\eta)$

$$-iq\left[\sigma_\varepsilon(q) * P(q,\eta)\right] + \left[iq\eta + \frac{\partial}{\partial \eta}\left(\frac{\eta}{\tau}+\frac{1}{2\tau^2}\frac{\partial}{\partial \eta}\right)\right] P(q,\eta) = 0, \tag{3.23}$$

which is hard to tackle analytically. If we consider only the positive half space ($v > 0$) for the Fokker-Planck equation (Eq. (3.20)) by using the exact dry friction

term

$$\left[\frac{\partial}{\partial v}(1-\eta)+\frac{\partial}{\partial \eta}\left(\frac{\eta}{\tau}+\frac{1}{2\tau^2}\right)\right]P(v,\eta)=0 \tag{3.24}$$

and if we perform a Laplace transform of the velocity, we obtain

$$(1-\eta)\left[sP(s,\eta)-P(v=0,\eta)\right]+\frac{\partial}{\partial \eta}\left(\frac{\eta}{\tau}+\frac{1}{2\tau^2}\right)P(s,\eta)=0. \tag{3.25}$$

The problem occurring here is that the term $P(v=0,\eta)$ is unknown, which makes it very difficult to obtain an exact expression for $P(v,\eta)$. Furthermore, we consider a perturbation expansion for small correlation times τ for the Fokker-Planck equation by rescaling the noise amplitude $\eta \to \tau^{-1/2}\eta$

$$\left[\frac{\partial}{\partial v}\left(\sigma_\varepsilon(v)-\frac{\eta}{\sqrt{\tau}}\right)+\frac{1}{\tau}\frac{\partial}{\partial \eta}\left(\eta+\frac{1}{2}\frac{\partial}{\partial \eta}\right)\right]P(v,\eta)=0. \tag{3.26}$$

We use the following ansatz for $P(v,\eta)$

$$P(v,\eta)=P_0(v,\eta)+\sqrt{\tau}P_1(v,\eta)+\tau P_2(v,\eta)+\mathcal{O}(\tau^{3/2}), \tag{3.27}$$

and we insert it into Eq. (3.26) to solve the equation for the different orders in τ. The problem with this approach is that the obtained expression not fulfil the required matching conditions for the velocity at $v=0$, thus we do not follow along the lines of such an approach here.

The marginal distribution for the noise amplitude is easily computed as

$$P_\eta(\eta)=\sqrt{\frac{\tau}{\pi}}\exp(-\tau\eta^2) \tag{3.28}$$

and does not depend on the regularisation. Hence Eq. (3.28) applies as well in the dry friction limit $\varepsilon \to 0$, which does not come as a surprise (cf. Eq. (3.1)). In the dry friction limit the expression

$$P(v,\eta)=\exp\left(-2|v|+2\tau\sigma_0(v)\eta-\tau\eta^2\right) \tag{3.29}$$

formally solves the stationary Fokker-Planck equation, see Eq. (3.19), in the limit $\varepsilon \to 0$, as long as v is nonzero. If we compute the marginal probability distribution

for the velocity from Eq. (3.29) we obtain

$$\begin{aligned} P(v) &= \int_{-\infty}^{\infty} \exp\left(-2|v| + 2\tau\sigma_0(v)\eta - \tau\eta^2\right) d\eta \\ &= \sqrt{\frac{\pi}{\tau}} \exp\left(-2|v| + \tau\sigma_0^2(v)\right). \end{aligned} \tag{3.30}$$

Eq. (3.30) differs from the regular part of the marginal in the framework of the UCNA (Eq. (3.15)) by the sign of the correction term $\tau\sigma_0^2(v)$. Certainly Eq. (3.29) does not provide an analytic solution for the stationary distribution as this expression does not obey the required matching conditions at $v = 0$. Nevertheless, if the impact of the stick-slip phenomenon at $v = 0$ remains localised then Eq. (3.29) provides the asymptotic behaviour for large values of velocities. This assertion can be verified by looking into the numerical data. In Fig. 3.7 slices of the regular distribution taken at constant values of the velocity show deviations from the Gaussian profile close to the singular component, i.e., at low velocities. However, the Gaussian profile according to Eq. (3.29) is restored when we increase the velocity, i.e., at regions in phase space further away from the sticking region. Deviations from the Gaussian profile, or strictly speaking, the asymmetry of the distribution in the η direction, can also be observed in Figs. 3.6(c) and 3.6(d) for a high noise correlation τ. A similar feature is displayed by slices taken at constant noise level, see Fig. 3.8.

The singular part of the distribution, i.e. the dynamics of sticking particles, is entirely governed by Eq. (3.1), i.e. by the Fokker-Planck equation of the Ornstein-Uhlenbeck process. However, natural boundary conditions do not apply as particles perform stick-slip transitions. For the singular part of the distribution at $v = 0$ we have already indicated that increasing the correlation time results in a considerable decrease of the probability of sliding particles. As a result, the main contribution to the marginal distribution, Eq. (3.28), will come from the distribution at $v = 0$ as, apart from a small contribution, particles become immobile. That is in quantitative agreement with direct simulations; see Fig. 3.9. For small values of the correlation time, considerable deviations from the normal distribution appear as on the one hand particles become mobile frequently and on the other hand there is a constant stream of mobile particles getting stuck (see as well Figs. 3.1 - 3.3).

In the region of the phase space close to the stick-slip transition the shape of the distribution is affected at intermediate values of the noise correlation. There is no

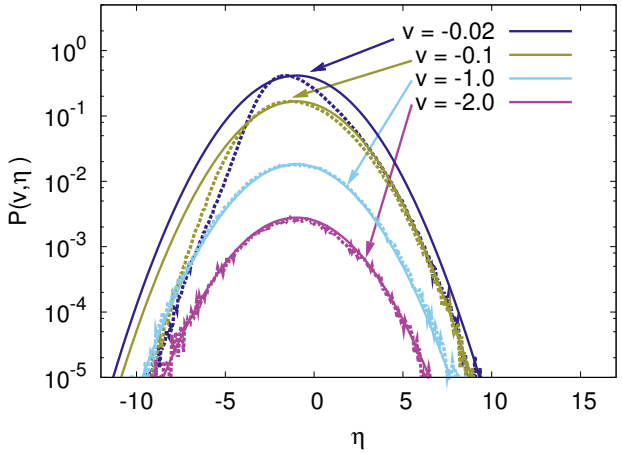

Figure 3.7: Regular component of the stationary probability distribution with $\tau = 0.1$. Dependence on the noise amplitude for different fixed values of the velocity v. Results of numerical simulations (dashed lines) and the analytic asymptotic expression (solid lines), Eq. (3.29). The normalisation of the analytics is fitted to the numerical data.

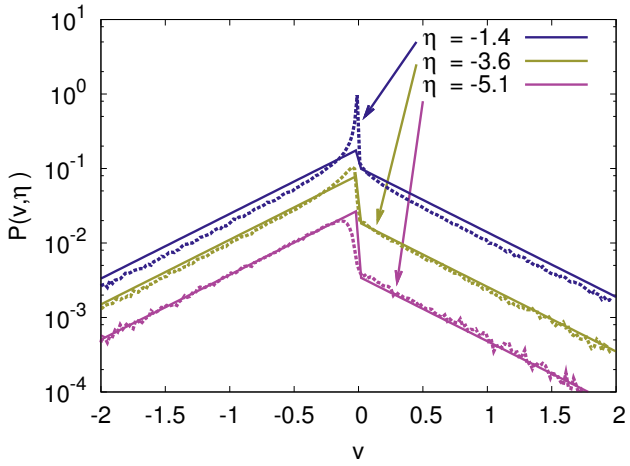

Figure 3.8: Regular component of the stationary probability distribution with $\tau = 0.1$. Dependence on the velocity for different fixed values of the noise amplitude η. Results of numerical simulations (dashed lines) and the analytic asymptotic expression (solid lines), Eq. (3.29). The normalisation of the analytics is fitted to the numerical data.

obvious way to tackle the issue by analytical means, e.g., with the matching conditions between the singular and the regular part. However, one can at least have a closer look at the probability current which is a clear signature of the nonequilibrium

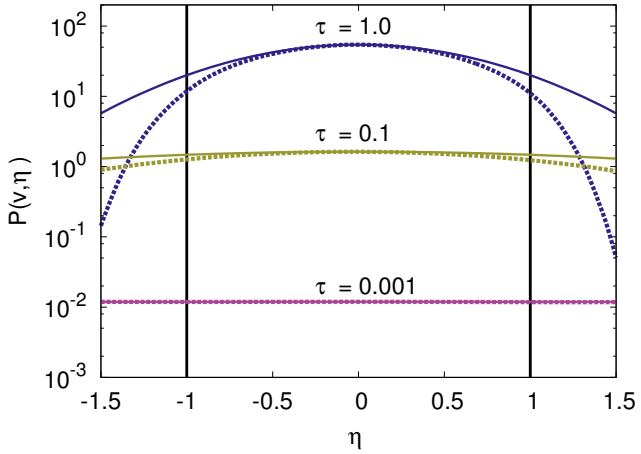

Figure 3.9: Slices of the stationary distribution at $v = 0$ in η direction, obtained from numerical simulations (dashed lines) and analytic results for the marginal distribution, Eq. (3.28) (solid lines) for different values of the noise correlation time. The vertical solid lines indicate the region of the singular part of the distribution (sticking regime). The normalisation of the analytics is fitted to the numerical data.

properties of our model. By using the method from [56] we compute the probability current directly from the time series of our model (Eqs. (3.1) and (3.2)) for different values of τ, see Figs. 3.10 and 3.11. The entire flow pattern is symmetric, and the main part of the current is concentrated in regions with low velocity v. For $\eta > 1$ the current predominantly points in the positive v-direction as particles are dragged by the external forcing. For larger positive values of v the current turns and finally approaches the sticking manifold, which lies at $v = 0$ and $|\eta| < 1$, where particles change from sliding to sticking mode. The probability current on the sticking manifold points in the positive or negative direction in η, away from the point $\eta = 0$, see Fig. 3.12. When reaching the critical value $|\eta| > 1$ particles start sliding again. In particular, the current on the sticking manifold, which is located at $v = 0$ and $|\eta| < 1$, and the current entering or leaving this manifold obey matching conditions.

Hence, for the piecewise-smooth dynamics one can write down a system of two coupled Fokker-Planck equations, one governing the sticking and one governing the sliding motion, with appropriate matching conditions and source terms. It is however not obvious whether such a formulation for the regular and the singular component of the probability distribution would give more insight than direct numerical simulations of the associated Langevin equation, let along providing a pathway for an

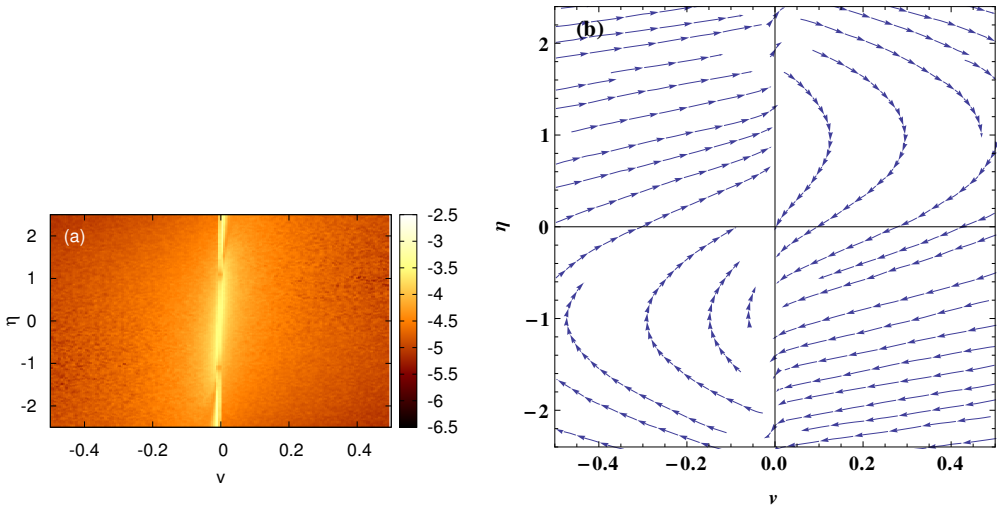

Figure 3.10: Logarithmic density plot (a) and stream plot (b) of the regular part of the stationary probability current of the system Eqs. (3.1) and (3.2) for $\tau = 0.1$, obtained from numerical simulations. The density plot shows the absolute value of the current in the (v, η) plane, whereas the stream plot displays the normalised vector field of the current.

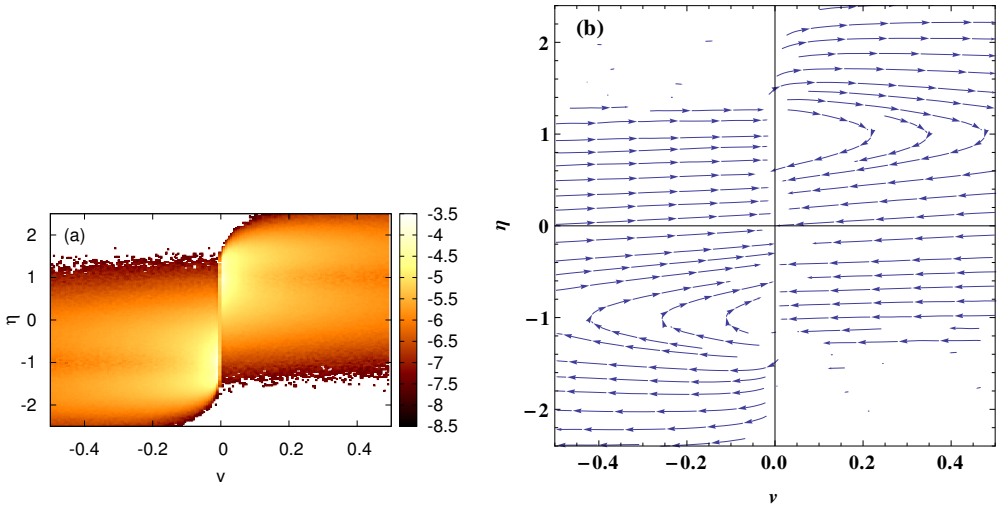

Figure 3.11: Logarithmic density plot (a) and stream plot (b) of the regular part of the stationary probability current of the system Eqs. (3.1) and (3.2) for $\tau = 1.0$, obtained from numerical simulations. The density plot shows the absolute value of the current in the (v, η) plane, whereas the stream plot displays the normalised vector field of the current.

analytic approach.

Figure 3.12 indicates a non-monotonic behaviour of the probability current on the sticking manifold by increasing the correlation time of the noise τ. As the sticking manifold is characterised by $v = 0$ and $|\eta| < 1$, the displayed η-component of the probability current represents the current on the sticking manifold for $\eta \in [-1, 1]$. For low values of τ, the current is very small, as we are close to the white noise limit. By increasing τ slightly to $\tau = 0.2$ the current on the sticking manifold increases also. Increasing τ further the current decreases and almost vanishes, see the results for $\tau = 3.0$ in Fig. 3.12. For high values of the noise correlation the probability current decays rapidly outside of the interval $\eta \in [-1, 1]$. In view of the particular structure of the stationary distribution this is hardly surprising, as the singular component of the distribution dominates for high correlation times, the dynamics is dominated by sticking particles, and only a small part of the probability distribution contributes to the sliding motion and finally to the probability current.

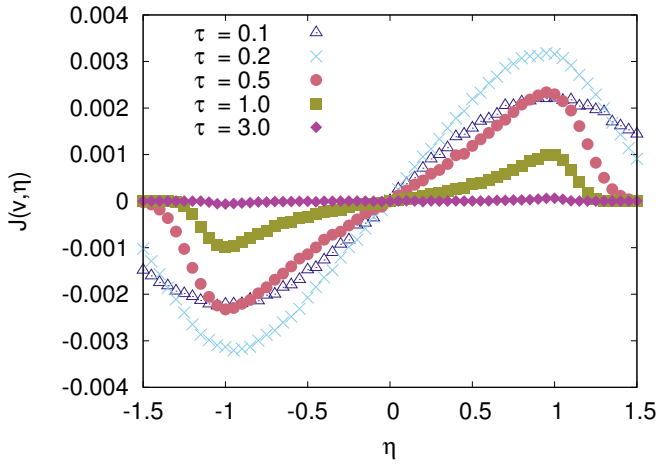

Figure 3.12: η-component of the stationary probability current at $v = 0$ for different values of the τ, obtained from numerical simulations of Eqs. (3.1) and (3.2).

3.3 Dynamical properties of the piecewise-linear model

Traditional correlation functions are a useful tool to study dynamical properties, in particular, within the context of linear response theories. From a theoretical per-

spective their analytical properties are related with the eigenvalue spectrum of the underlying equations of motion, e.g. with the spectrum of Fokker-Planck operators. As previously mentioned in Sec. 2.1, the autocorrelation function is connected to the power spectral density via the Wiener-Khinchin theorem [38]. Thus, by studying the power spectral density, we can extract some information about the non-vanishing eigenvalues of the underlying Fokker-Planck operator, especially in the absence of analytical results for the time-dependent propagator and the underlying eigenvalue spectrum. Furthermore, correlation functions are experimentally accessible and they allow one to introduce the concept of correlation times. As a shortcoming, correlation functions may not allow for the proper characterisation of intermittent behaviour, such as stick-slip transitions, which needs then to be addressed separately by a suitable statistical measure.

3.3.1 Power spectral density

To begin with, we want to investigate how the correlation time of the noise τ influences the correlations in our system. To be slightly more precise we will discuss the τ-dependence of the power spectral density of the velocity v, and the corresponding linewidth. The latter provides insight into the structure of the eigenvalue spectrum of an underlying Fokker-Planck operator governing the dynamics of the system. For the pure dry friction model with white noise, where analytical results for the eigenvalue spectrum are accessible, a spectral gap can be found between $\Lambda_0 = 0$ and a continuous spectrum of the other eigenvalues [82, 94]. In [95] a closed expression for the power spectral density of the velocity has been derived based on the Laplace transform of the propagator for a model including dry friction, viscous friction and constant bias.

Since we have a noise with finite correlation time we mainly rely on numerical investigations since analytic expression for the stationary probability distribution are unknown. We calculate the power spectral density of the velocity v by averaging over 800 numerically generated time traces of length $T = 10^4$. We base our analysis on the autocorrelations of the velocity. Hence, the corresponding power spectral density predominantly probes properties of the sliding phase as velocities vanish in the sticking phase.

Figure 3.13 shows the numerical results of the normalised spectral densities for

different values of τ. The normalisation has been done by setting $S_N(0) = 1$. The normalised power spectral densities $S_N(\omega)$ have a single central peak at $\omega = 0$ indicating an exponential decay of the corresponding autocorrelation function. For small values of τ, and in accordance with the white noise limit, $S_N(\omega)$ is a Lorentzian with a power law behaviour ω^{-2} at an intermediate frequency range. Such decay changes when we increase the noise correlation time τ: the decay changes to a ω^{-4} behaviour at medium frequencies. The corresponding analytic behaviour indicates a smooth autocorrelation function at time zero. The observed change in the decay seems to be a feature of linear stochastic systems subjected to coloured noise, as such a result that has also been observed for the Ornstein-Uhlenbeck process driven by coloured noise, see Sec. 2.1 and in particular Eq.(2.27b).

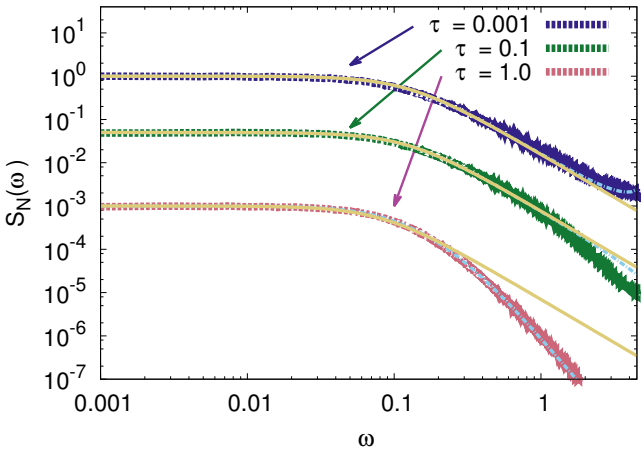

Figure 3.13: Double-logarithmic plot of the power spectral density of the v-variable for $\tau = 0.001,\ 0.1,\ 1.0$ (from top to bottom) and different fit functions. Spectra have been normalised by the condition $S_N(0) = 1$ and shifted respectively. Numerical simulations (dashed lines), Lorentzian fit ($\sim 1/(1+\omega^2)$) (yellow solid lines), quartic spectral fit ($\sim 1/(1 + a\omega^2 + b\omega^4)$) (cyan dot-dashed lines).

For power spectral densities with a well defined central peak, the full width at half maximum $\Delta\omega$ can be related to the correlation time of the system t_{corr} via the Wiener-Khinchin theorem. Following results for linear stochastic processes (see Eq. (2.11)) we define here a correlation time by $t_{corr} = 1/\Delta\omega$. Using a fit function of the form $1/(1 + a\omega^2 + b\omega^4)$ for the power spectral densities $S_N(\omega)$ we evaluate the correlation time for different values of the noise correlation time, see Fig. 3.14.

The correlation time t_{corr} essentially coincides with the value of the white noise

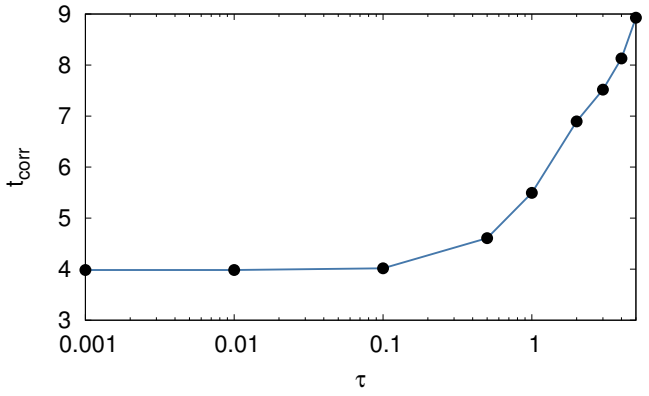

Figure 3.14: Correlation time t_{corr} as a function of the noise correlation time τ, obtained from numerical simulations of the spectral density and estimating the full width at half maximum by using a quartic spectral fit, see Fig. 3.13.

limit as long as $\tau < 0.1$. This value can be found also analytically via the autocorrelation function (see [94]). While there is no sharp transition, t_{corr} experiences a significant monotonic increase when the noise correlation time exceeds a "critical" value of $\tau = 0.1$. Hence, signatures of the stick-slip transition become dynamically visible above such a critical value. The transition-like feature is in accordance with the findings concerning the stationary distribution reported in the previous section, e.g. see Fig. 3.5, where the probability of sticking starts to increase if the correlation time of the noise exceeds the value $\tau = 0.1$. The increase of the correlation time of the velocity does not come as a surprise, because with a higher correlation time of the noise τ the stochastic perturbations decrease, which leads to more unperturbed dynamics and therefore a higher correlation of the velocity.

3.3.2 Distribution of sticking and sliding periods

After discussing the properties of our model concerning the spectral gap of the Fokker-Planck operator, we want to focus here on statistical measures for stick-slip transitions. The time series shown in Figs. 3.1 - 3.3 suggest a closer relation of the dynamics to intermittency phenomena. To probe directly the dynamical features of the stick-slip transition we look at the distribution of sticking and sliding times, i.e., the distribution of time intervals the particle spends in states $v = 0$ and $v \neq 0$.

We start our investigations with the analysis of the sticking time events. We recall the conditions for sticking from Eq. (3.2): if the particle has velocity $v = 0$ and the absolute value of the noise amplitude $\eta(t)$ is smaller than one, the particle sticks. However, if the particle was at rest and $|\eta(t)|$ exceeds the value 1, it starts sliding again. Thus, if we have the situation that $v = 0$ and the noise amplitude attains a value $|\eta_0| < 1$ (which can be considered as an initial value), we have to wait a specific time period T until the noise amplitude η attains again a value which lies outside the interval $\eta \in [-1, 1]$. This time period T, i.e. the sticking time period, depends only on the dynamics of the noise amplitude $\eta(t)$. Therefore, we can relate the dynamics of a sticking particle to the exit time problem of the Ornstein-Uhlenbeck process. Here we need to consider an escape from the interval $[-1, 1]$.

As a first step, we discuss the choice of the inital value η_0. Since every value within the interval $[-1, 1]$ can be an initial value for the exit time problem (as the sticking condition is $v = 0$ and $|\eta(t)| < 1$), there is no distinguished value for η_0 from the dynamics of our model. Therefore, we perform numerical simulations of the dynamical equations (Eqs. (3.1) and (3.2)) to find the distribution $P(\eta_0)$, i.e. those values for η when we have $v = 0$ at the beginning of each particular sticking time period. The results for different values of the noise correlation time τ are shown in Fig. 3.15. We observe that for small correlation times, the distribution of

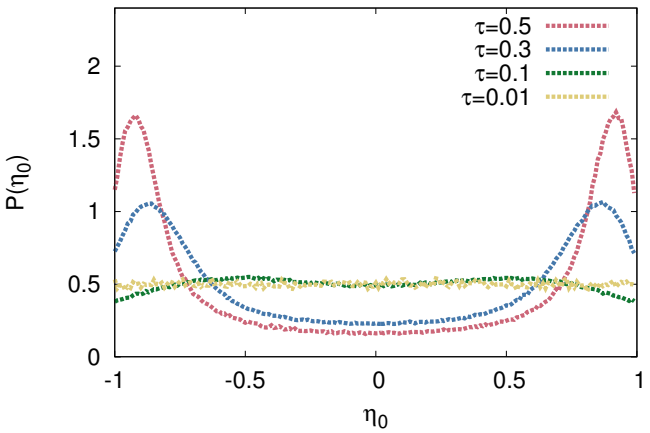

Figure 3.15: Distribution of initial values $P(\eta_0)$, obtained numerically for different values of the noise correlation time: $\tau = 0.01$ (yellow), $\tau = 0.1$ (green), $\tau = 0.3$ (blue), $\tau = 0.5$ (red).

initial values is uniformly distributed over the interval $[-1,1]$. However, for values $\tau > 0.1$ we observe a transition to a bimodal distribution and the two maxima of the distribution are moving towards the boundaries of the interval $[-1,1]$ for increasing correlation time τ.

Next, we aim to find an analytical expression for the exit time distribution. Since we consider an Ornstein-Uhlenbeck process, the related exit time problem can be treated by analytical means, e.g. see [25]. The Laplace transform of the exit time distribution for an Ornstein-Uhlenbeck process like Eq. (3.1) with symmetric absorbing boundaries at $-\alpha$ and α and an initial value $|\eta_0| < \alpha$ reads

$$\tilde{f}(s,\eta_0) = \frac{D_{-s\tau}\left(\sqrt{2\tau}\eta_0\right) + D_{-s\tau}\left(-\sqrt{2\tau}\eta_0\right)}{D_{-s\tau}\left(\sqrt{2\tau}\alpha\right) + D_{-s\tau}\left(-\sqrt{2\tau}\alpha\right)} \exp\left(\frac{\tau}{2}(\eta_0^2 - \alpha^2)\right). \tag{3.31}$$

Here $D_{-s\tau}\left(\sqrt{2\tau}\eta_0\right)$ is the parabolic cylinder function (see App. C.1). A detailed derivation of the exit time distribution in Eq. (3.31) can be found in App. D. We can rewrite Eq. (3.31) in a more compact way by using hypergeometric functions

$$\tilde{f}(s,\eta_0) = \frac{{}_1F_1\left(\frac{s\tau}{2};\frac{1}{2};\eta_0^2\tau\right)}{{}_1F_1\left(\frac{s\tau}{2};\frac{1}{2};\alpha^2\tau\right)}. \tag{3.32}$$

Here ${}_1F_1\left(\frac{s\tau}{2};\frac{1}{2};\alpha^2\tau\right)$ denotes the confluent hypergeometric function and we have used specific relations between parabolic cylinder functions and the confluent hypergeometric function to arrive at Eq. (3.32) (see Eqs. (C.24) and (C.25) for details). We set $\alpha = 1$ because the regime, where the particle is sticking, is the interval $[-1,1]$, which reflects the value of the rescaled dry friction coefficient.

In the following, we consider two different approaches to evaluate Eq. (3.32) with respect to η_0. As we have a uniform distribution for small correlation times τ (see Fig. 3.15), we integrate Eq. (3.32) over all possible initial conditions within the interval $\eta_0 \in [-1,1]$

$$\begin{aligned}
\tilde{f}(s) &= \int_{-1}^{1} P(\eta_0)\tilde{f}(s,\eta_0)d\eta_0 \\
&= \frac{1}{2}\int_{-1}^{1} \frac{{}_1F_1\left(\frac{s\tau}{2};\frac{1}{2};\eta_0^2\tau\right)}{{}_1F_1\left(\frac{s\tau}{2};\frac{1}{2};\tau\right)}d\eta_0 \\
&= \frac{{}_1F_1\left(\frac{s\tau}{2};\frac{3}{2};\tau\right)}{{}_1F_1\left(\frac{s\tau}{2};\frac{1}{2};\tau\right)}.
\end{aligned} \tag{3.33}$$

Details of the integration in Eq. (3.33) can be found in the appendix (see Eqs. (C.26) - (C.32)). We expect this result to be appropriate for small correlation times of the noise. To deal with higher correlation times τ we use the expression from Eq. (3.32) (with $\alpha = 1$) and insert the numerically obtained value of η_0, where the distribution of initial conditions $P(\eta_0)$ attains one of its maxima (see Fig. 3.15). For example for $\tau = 0.5$, we choose $\eta_0 = 0.92$. Since the interval and the distribution are symmetric around $\eta_0 = 0$ and the expression in Eq. (3.32) is quadratic in η_0, it does not matter wich maximum of the distribution is taken.

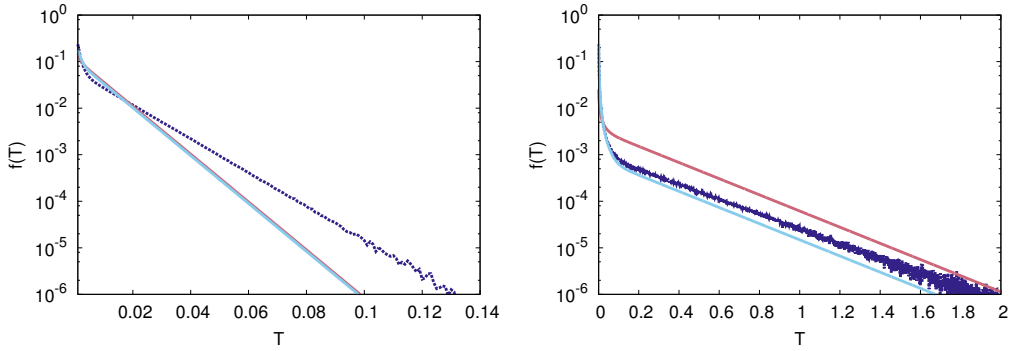

(a) $\tau = 0.1$ (b) $\tau = 0.5$

(c) $\tau = 1.0$ (d) $\tau = 3.0$

Figure 3.16: Distribution of sticking time intervals, $f(T)$, on a semi-logarithmic scale, obtained numerically (blue dashed line) and semi-analytically from the exit time problem for the Ornstein-Uhlenbeck process for different values of the noise correlation time τ. The solid red line denotes the inverse Laplace Transform of $\tilde{f}(s)$ (Eq. (3.33)) and the solid cyan line is the inverse Laplace Transform of $\tilde{f}(s, \eta_0)$ (Eq. (3.32)) with $\alpha = 1$ and the following values for the inital value η_0: $\eta_0 = 0.5$ (a), $\eta_0 = 0.92$ (b), $\eta_0 = 0.96$ (c), $\eta_0 = 0.98$ (d).

As it is not possible to derive an analytical result for the inverse Laplace transform of Eqs. (3.32) and (3.33), we use the Talbot method to invert the exit time distribution numerically [1, 91]. The analytical estimates are inverted numerically over a specific time interval and normalised with respect to the obtained values within this time interval. A comparison between the semi-analytical approach and direct numerical simulations for a few values of the noise correlation time τ is shown in Fig. 3.16.

One observes a localised peak in the distribution at $T = 0$, and for moderate to large times a simple exponential decay. For small correlation times, the noise amplitude is still large enough that the particle will not stick for a long time. Therefore, the decay of the distribution is strong. For higher correlation times we observe from Fig. 3.15 that it is more likely for $\eta(t)$ to attain values closer to the boundaries of the sticking interval $[-1, 1]$ and therefore, a quick escape from the interval is possible. On the other hand, it also becomes more likely for the particle to stick as it may take some time until the noise amplitude is large enough that the particle starts sliding again. This is in accordance with the results in the previous sections, e.g. the increase of the probability of sticking for increasing correlation time τ (Eq. (3.18) and Fig. 3.5).

For small correlation times ($\tau = 0.1$), we observe deviations from the numerics to the two semi-analytical results as the purely numerical result decays slower for larger time periods T than the analytical estimates (Fig. 3.16(a)). If we increase the correlation time of the noise, the semi-analytical result, which includes the numerically computed initial value (Eq. (3.32)), fits very well with the purely numerical results (see Figs. 3.16(b) - 3.16(d)). The other analytical estimate (Eq. (3.33)), in which we have averaged over the initial values assuming a uniform distribution, only gives a qualitative result as it underestimates the peak at $T = 0$ and shows a slightly different exponential decay (see Fig. 3.16(b)).

For the remainder of this chapter we focus on the statistics of the sliding events. This analysis is done only numerically, as an analytical counterpart could not be identified in contrast to the sticking time events, where semi-analytical results could be obtained from the exit time problem of the Ornstein-Uhlenbeck process. We evaluate the time series such that we count the time intervals from the point the trajectory leaves the sticking manifold until it arrives back at the sticking manifold. Fig. 3.17 show the numerically obtained distributions over a wide range of noise

correlation times.

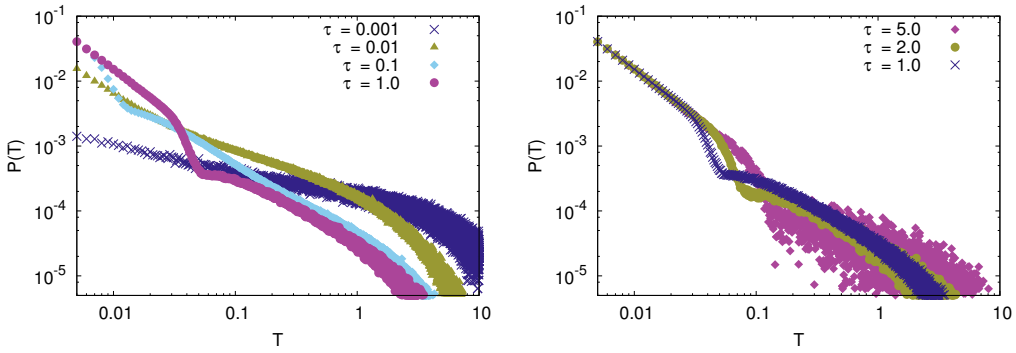

(a) (b)

Figure 3.17: Distribution of sliding time intervals, $P(T)$, on a double-logarithmic scale for different values of the noise correlation time, obtained from numerical simulations.

For small noise correlation times the distributions are unimodal with a power law decay from small times T to an intermediate range and an exponential cut-off for very large sliding times T. By increasing the noise correlation time τ the maximum of the distributions increases, but only up to a certain value. Furthermore, the exponent of the power law decay also increases for higher noise correlation times. However, the most surprising result is that we observe some kind of universal behaviour of the distributions at short sliding times T for large correlation times $\tau \geq 0.1$, see Fig. 3.17(b). The distributions above this value of τ exhibit three different regimes of decay over the whole range of sliding times T: for small sliding times we have a power law decay, for a small range of intermediate values of T one observes a strong exponential decay and for large T we still have an exponential decay but it decreases slower than before. This described behaviour is visualised in Fig. 3.18. Furthermore, the intermediate range with the strong exponential decay is shifted towards higher sliding times by increasing the noise correlation time τ, see Fig. 3.17(b).

To underline our observations we evaluate some of our the numerical data; we estimate the power law decay and the exponential decay roughly for the distributions with the correlation times $\tau = 0.001$ and $\tau = 1.0$. Our obtained fit functions are

$$\rho_1(T) \sim T^{-9/20}, \tag{3.34a}$$

$$\rho_2(T) \sim T^{-4/3} \exp\left(-(25T)^3\right), \tag{3.34b}$$

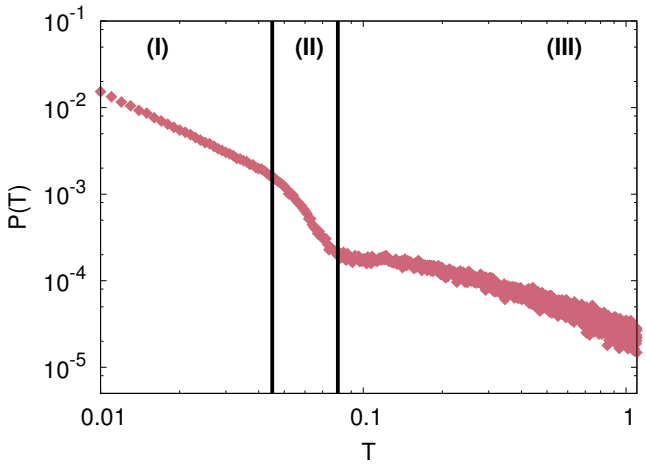

Figure 3.18: Sliding time distribution for $\tau = 1.0$ to visualize the three regimes with different decay behaviour of the distribution: (I) power law decay, (II) strong exponential decay, (III) weak exponential decay. See also Eqs. (3.34a), (3.34b) and Fig. 3.19.

where $\rho_1(T)$ fits the power law decay for $\tau = 0.001$, whereas $\rho_2(t)$ is used to fit the power law decay and the strong exponential decay for $\tau = 1.0$. These results are shown in Fig. (3.19).

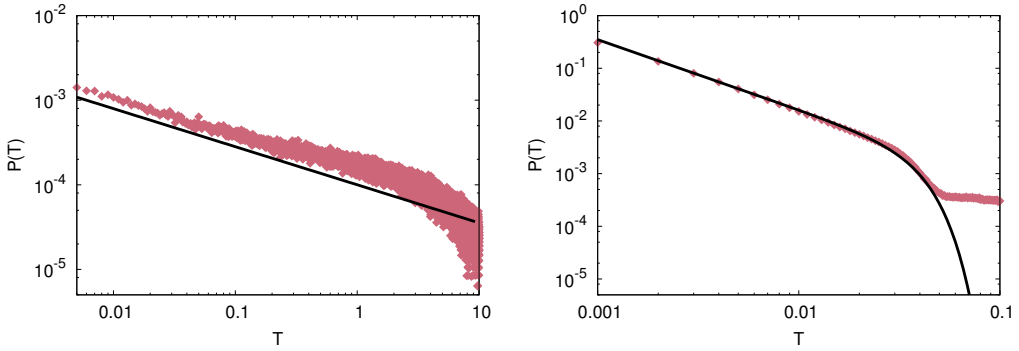

(a) $\tau = 0.001$ (b) $\tau = 1.0$

Figure 3.19: Distribution of sliding time intervals, $P(T)$, on a double-logarithmic scale for $\tau = 0.001$ (a) and $\tau = 1.0$ (b). Numerics (red diamonds) and the fit functions (black solid lines) $\rho_1(T)$ (Eq. (3.34a)) and $\rho_2(T)$ (Eq. (3.34b)).

We observe the described power law decay in Fig. 3.19(a) and the exponential cut-off for large times T. In comparison, the exponent from the power law decay in the case of a higher correlation time τ is larger, and for intermediate sliding times,

the contribution from the exponential function becomes visible (see Eq. (3.34b) and Fig. 3.18 as well). As already mentioned, the observed on-off (stick-slip) dynamics of our model suggest a relation to intermittency. In [49], where on-off intermittency has been studied, the authors observed a power law decay of the form $T^{-3/2}$. In the context of our model the role of the "on" and of the "off" state are interchanged as here the observed power law is connected to the sliding events. Furthermore, the above found exponent is also fractional, but here we have a behaviour of the form $T^{-4/3}$. So far, we have not found an intuitive explanation for this universal behaviour of the sliding times for high noise correlation times.

As already mentioned, a related analytical model has not yet been found. The most suitable candidate for such a model would be the exit time problem for a stochastic process with constant drift and coloured noise with an absorbing boundary at the origin. For Gaussian white noise instead of an Ornstein-Uhlenbeck noise, this problem can be solved analytically, see e.g. [67]. The exit time distribution shows an asymptotic behaviour of the form $P(T, v_0) \sim T^{-3/2} \exp\left(-(T - v_0)^2/2T\right)$ in this case. However, exact analytical results for an exit time problem including coloured noise and very specific boundary conditions are very difficult to obtain. Furthermore, if we set the absorbing boundary condition at $v = 0$ and only natural boundary conditions for η apply, such a description will not capture all possible sliding events appropriately. To visualize this shortcoming of such an approach, we compute two different realisations for the sliding dynamics in the (v, η) plane, see Fig. 3.20.

The realisation in Fig. 3.20(a) could be captured by an exit time problem with absorbing boundary at $v = 0$. The trajectory starts at the blue dot and evolves towards the negative velocities before it turns back and arrives at $v = 0$ but within the sticking interval $\eta \in [-1, 1]$. On the contrary, the realisation in Fig. 3.20(b) shows that the trajectory makes a transition from negative towards positive velocities but here at $\eta > 1$. That means it does not reach the sticking manifold and the particle continues to slide until it reaches the sticking manifold later. From the perspective of an exit time problem, as described, only the time until reaching $v = 0$ will be considered as a time interval, which would underestimate the actual length of the sliding time period.

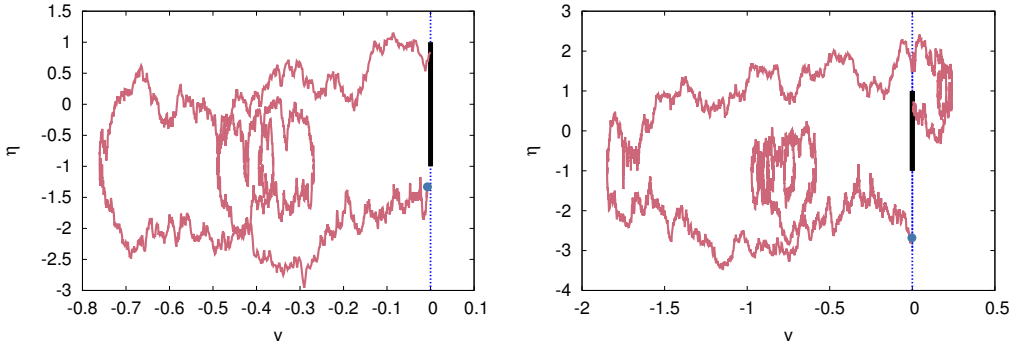

(a) (b)

Figure 3.20: Two different realisations for the sliding dynamics in the (v, η) plane, starting from the blue dot and evolving towards the negative half space of the velocity. The dashed blue line seperates the two half spaces of the velocity whereas the thick black line denotes the sticking manifold ($v = 0$ and $\eta \in [-1, 1]$). These representations have been obtained numerically from Eqs. (3.1) and (3.2).

3.4 Summary of the chapter

We investigated a dry friction model subjected to coloured noise with the emphasis on nonequilibrium properties in a noisy piecewise-smooth dynamical system. By applying the unified coloured noise approximation (UCNA), we obtained an analytical expression of the stationary probability distribution for the velocity. The white noise limit $\tau \to 0$ reproduces the exact results, e.g., see [27]. As the noise correlation time increases, the stationary distribution develops a delta peak, as particles become more and more stuck at $v = 0$. Thus, by varying τ, a transition from sliding to sticking dynamics could be observed. By considering the equivalent two-dimensional system we were able to derive an asymptotic expression for the stationary distribution which is valid for large velocities and large noise amplitudes, far away from the stick-slip region. There was no obvious way to obtain a full analytic expression for the joint probability distribution $P(v, \eta)$ containing all the required matching conditions at $v = 0$ as detailed balance is violated. The latter has been clearly demonstrated by computing the non-vanishing stationary probability current.

Furthermore we studied the power spectral density numerically to obtain information about the velocity correlations, the corresponding correlation time, and the spectral gap of the underlying Fokker-Planck operator. Below a "critical value" one

recovers the result for the white noise limit. Increasing the noise correlation further, the full width at half maximum decreases, which is connected to a higher velocity correlation in the system. This decrease of the spectral width comes together with a change in shape of the power spectrum. For low values of τ the power spectral density has the shape of a Lorentz profile for values $\tau > 0.1$ the shape changes to a ω^{-4} decay for intermediate frequencies.

To complete our studies, we investigated the sliding and sticking time distribution as the time traces indicated a connection to intermittent dynamics. Results for the sticking time distribution were accessible via the exit time problem for an Ornstein-Uhlenbeck process with symmetric absorbing boundary conditions. For the sliding dynamics the related exit time problem with coloured noise and a constant drift is very hard to find and to tackle; thus, we had to rely on numerical simulations. For high noise correlation times a surprising power law decay of the form $T^{-4/3}$ occurs for short sliding times T, followed by an exponential decay for intermediate and long sliding time periods.

Some of the observed results for our model seem to be key features of dry friction models subjected to noise and of general piecewise-smooth stochastic dynamics. Intermittent dynamics and a singular part of the probability distribution have also been found in the framework of the Boltzmann-Lorentz equation by investigating the so-called independent kick model [92, 93], in studies of dry friction subjected to Non-Gaussian noise in the high friction limit [58], and in an experiment of a rotating probe, which is in contact to a granular gas [41]. It is important to mention that despite the similarities in the dynamics there is no mathematical link between the Boltzmann-Lorentz equation and the investigated dry friction model subjected to coloured noise.

Chapter 4

Dry friction models including viscous friction and constant bias

In this chapter, we extend our previously studied model with pure dry friction and coloured noise (Eq. (3.2)) by adding viscous friction and a constant bias (or constant force). We want to explore the impact of the correlation time of the noise τ in a system, which contains two different types of friction (dry and viscous). In addition, as the total applied force subjected to the system has now an additional deterministic contribution, we are interested in how aspects of the dynamics change, e.g. sticking phenomena. The additional bias induces a stick-slip bifurcation in the deterministic system. Therefore, the viscous friction is needed to keep the velocity at finite values. As the full stochastic system does not obey detailed balance, analytical calculations might be become very difficult. However, as this model is still piecewise linear, we hope to be able to derive some results analytically, if necessary with the help of suitable approximation schemes, e.g. the unified coloured noise approximation.

First, in Sec. 4.1, we show time traces of our extended model by performing numerical simulations and we study the new features of our extended system. In addition, some aspects of the corresponding deterministic system are discussed (Sec. 4.1.1), i.e. signatures of stick-slip dynamics. In Section 4.2.1, the unified coloured noise approximation (see Secs. 2.2 and 3.2.1) is used to obtain an analytical expression for the marginal probability density of the velocity $P(v)$. For parameter values close to the deterministic stick-slip transition, the probability of sticking exhibits a non-monotonic behaviour as a function of the noise correlation

time τ. Furthermore, we compute the joint stationary probability density and the probability current numerically. These results are discussed in Section 4.2.2. Dynamical features of this extended model are elaborated in Section 4.3 by computing the power spectral density and the correlation time of the velocity. The analysis is done for different values of the viscous friction while we study the impact of the correlation time of the noise τ on the correlations of the velocity. In addition, we investigate the sticking and sliding time distributions, similarly to Section 3.3.2. However, in this chapter, these investigations are done only numerically. A summary of the chapter can be found in Section 4.4.

4.1 Piecewise-linear dry friction model

Equation (1.2) represents the full model with dry friction, viscous friction, a constant force and Gaussian white noise. Here we will replace the white noise by an Ornstein-Uhlenbeck noise. Thus, the equation of motion for the velocity changes to

$$\dot{v}(t) = \begin{cases} 0 & \text{if } |b + \eta(t)| < 1 \text{ and } v = 0, \\ -\gamma v(t) - \sigma_0(v(t)) + b + \eta(t) & \text{otherwise,} \end{cases} \tag{4.1}$$

where γ is the viscous friction coefficient and b denotes the rescaled constant force (see App. B.7 for details). $\sigma_0(v(t))$ is the sign function representing the dry friction. The subscript 0 in the expression $\sigma_0(v)$ is assigned to the sign function, whereas a subscript ε will refer to a smoothed version of the dry friction (see Eq. (3.4)). Thus, we could rewrite Eq. (4.1)

$$\dot{v}(t) = -\gamma v(t) - \sigma_\varepsilon(v(t)) + b + \eta(t) \tag{4.2}$$

and consider results in the limit $\varepsilon \to 0$ (see Eq. (3.3) as well). $\eta(t)$ describes the Ornstein-Uhlenbeck noise, whose dynamics is governed by the following equation:

$$\dot{\eta} = -\frac{\eta(t)}{\tau} + \frac{\xi(t)}{\tau}, \tag{4.3}$$

where τ represents the correlation time of the noise. In comparison to the previous chapter, the total applied force to the particle is now $b + \eta(t)$, consisting of an

additional deterministic part b and the stochastic contribution $\eta(t)$. Therefore, we need to adjust the conditions when the particle is sticking and when it is sliding (compare Eq. (4.1) with Eq. (3.2)). If the total applied force is smaller than the rescaled dry friction coefficient, $|b + \eta(t)| < 1$, and the particle has velocity zero $v = 0$ at the same time, then it sticks. Note that if we have $|b + \eta(t)| < 1$ but the velocity is non-zero $v \neq 0$, then the particle is still sliding: it relaxes towards $v = 0$ or towards the fixed point of the sytem, depending on the value of b. On the other hand, if the total applied force is larger than the dry friction coefficient, $|b + \eta(t)| > 1$, then the particle starts sliding again if it was previously at rest. Thus, we arrive at the sticking conditions in Eq. (4.1). The adjusted condition can be rewritten if one wants to consider a condition only for the stochastic force $\eta(t)$. Then, from $|b + \eta(t)| < 1$, we can express the sticking condition as follows

$$-1 - b < \eta(t) < 1 - b. \tag{4.4}$$

Thus, the sticking interval, i.e. which is the interval of values of η such that the total applied force is not large enough to move the particle (here $\eta \in [-1-b, 1-b]$), is shifted depending on the sign and the absolute value of the constant force. For $b = 0$, we arrive again at the known result from the previous chapter.

4.1.1 Deterministic dynamics

Before we present numerical results for the time traces of our stochastic model (Eqs. (4.1) and (4.3)), we discuss some aspects on the corresponding deterministic model to motivate our choices for the parameter values used in this chapter. In the absence of the noise ($\eta(t) = 0$ in Eq. (4.1)), the deterministic equation of motion for the velocity reads

$$\dot{v}(t) = \begin{cases} 0 & \text{if } |b| < 1 \text{ and } v = 0, \\ -\gamma v(t) - \sigma(v(t)) + b & \text{otherwise.} \end{cases} \tag{4.5}$$

For the sake of convenience we have dropped the subscript 0 for the dry friction here ($\sigma_0(v) = \sigma(v) = \mathrm{sgn}(v)$), since we do not consider a smoothed friction term here in Sec. 4.1.1. The above discussion concerning sticking and sliding applies here as well, the only difference being that the total applied force consists only of the constant

force b. We can write down the solution for the velocity from Eq. (4.5) if we take the two different dynamics, caused by the dry friction term, for the respective half spaces into account ($\sigma(\pm v(t)) = \pm 1$)

$$v^+(t) = v_0 \exp(-\gamma(t - t_0)) + \frac{b-1}{\gamma}\left[1 - \exp(-\gamma(t - t_0))\right], \quad v_0 \geq 0, \tag{4.6a}$$

$$v^-(t) = v_0 \exp(-\gamma(t - t_0)) + \frac{b+1}{\gamma}\left[1 - \exp(-\gamma(t - t_0))\right], \quad v_0 \leq 0. \tag{4.6b}$$

If the velocity becomes zero, one has to take into account the sticking condition in Eq. (4.5). Eq. (4.6a) applies for $v_0 = 0$ only if $b > 1$, otherwise we just have $v_0 > 0$. Similarly for Eq. (4.6b), we have $v_0 = 0$ only if $b < -1$, otherwise $v_0 < 0$. We illustrate the dynamics of the deterministic model (Eq. (4.5)) in Fig. 4.1, where the time evolution according to Eqs. (4.6a) and (4.6b) is shown for two different values of the constant force b and a positive initial velocity v_0.

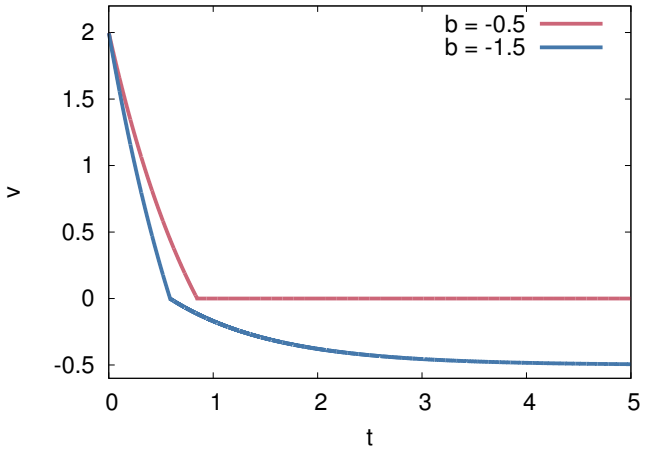

Figure 4.1: Time evolution for the velocity $v(t)$ of the deterministic model (Eqs. (4.5) - (4.6b)) for different values of the constant bias $b = -0.5$ (red solid line) and $b = -1.5$ (blue solid line) with the initial condition $v(0) = v_0 = 2$. Further parameter $\gamma = 1$.

For $b = -0.5$ (red solid line in Fig. 4.1), the velocity decreases towards zero according to Eq. (4.6a). If $v(t)$ reaches $v = 0$, the velocity stays zero, as we have $|b| < 1$ (see Eq. (4.5)). For $b = -1.5$ (blue solid line in Fig. 4.1), the velocity decreases as well towards zero, which also can be described by Eq. (4.6a) with $v_0 = 2$ and $t_0 = 0$. As the velocity attains the value zero, it does not stay zero here,

since we have $|b| > 1$. Thus, the velocity becomes negative and follows Eq. (4.6b) then. Note that we have in Eq. (4.6b) $v_0 = 0$ and $t_0 = t'$, where t' denotes the time when the velocity reaches zero after evolving from its initial value $v_0 = 2$ at $t_0 = 0$. t' can be computed from Eq. (4.6a) by inserting all the parameters (see caption of Fig. 4.1 as well)

$$2\exp(-t') - 2.5\,[1 - \exp(-t')] = 0 \tag{4.7}$$

and we obtain here $t' = -\log\left(\frac{5}{9}\right) \approx 0.587$. Then Eq. (4.6b) shows that the velocity approaches the fixed point v^* of the system in Eq. (4.5), which is negative here.

In general, we find that the fixed point v^* of our model (Eq. (4.5)) is given by

$$v^* = \begin{cases} 0 & \text{if } |b| \leq 1, \\ \sigma(b)\frac{|b|-1}{\gamma} & \text{if } |b| > 1. \end{cases} \tag{4.8}$$

Here $\sigma(b)$ denotes the sign function. From Eq. (4.8) we can see that a transition between two different dynamical regimes takes place at $|b| = 1$, which is the deterministic stick-slip transition. We will denote the regime where the constant force attains values smaller than the dry friction coefficient ($|b| < 1$) as the sticking regime, whereas the other dynamical regime with $|b| > 1$ is addressed as the sliding regime. Note also that the fixed point v^* of the deterministic system depends not only on the constant force b, but on the viscous friction coefficient γ as well. For example for the blue curve in Fig. 4.1, the fixed point is $v^* = -0.5$ as we have $\gamma = 1.0$ and $b = -1.5$. Therefore, in the analysis of our stochastic model (Eq. (4.1)) we will focus our investigations on parameter values below ($|b| \leq 1$) and above ($|b| > 1$) this stick-slip transition and resulting effects. As in the previous chapter, we set the static and kinetic friction equal and therefore the considered system does not show hysteresis.

If these two friction coefficients were not the same and the kinetic friction μ_S is smaller than the static friction μ_C (as it is in most cases), the following scenario for hysteresis could be observed: to move an object, which was initally at rest ($v = 0$), an applied force F needs to be larger than the static friction coefficient $F > \mu_S$. When the object starts moving the stationary velocity will not increase gradually but it will jump towards a value $v^* \sim F - \mu_C > F - \mu_S$, since the kinetic friction has to be applied for the situation that the velocity is non-zero. If the applied force is

then decreased, the object only relaxes towards $v = 0$ if the applied force is smaller than the kinetic friction ($F < \mu_C$). Therefore we could have the situation, where $F < \mu_S$ but $v^* \neq 0$. Further thoughts in this direction can be found in Chapter 6.

4.1.2 Stochastic dynamics

After the discussion on the deterministic system, we want to compare the new features of our extended stochastic model with the previously shown results for the pure dry friction model (see Sec. 3.1). We perform numerical simulations and show time traces of the velocity for different parameter values of γ, b and τ. We use an Euler-Maruyama scheme (see App. A) with step size $h = 10^{-3}$ for our numerical analysis. In the same way, we take the impact of the dry friction into account by setting $v = 0$ for $|v| < 10^{-3}$ and $|b + \eta| < 1$. It is important to mention that for our investigations in this chapter the sign of the constant force b does not matter as it can be absorbed in a coordinate transform $v \to -v$. Quantities related to the stick-slip transition, e.g. the probability of sticking, stay invariant under a change of the sign for b. But this invariance does not hold in general for all statistical quantities; e.g. conditional probabilities could exhibit a different behaviour for $-b$ and b depending on the initial value v_0.

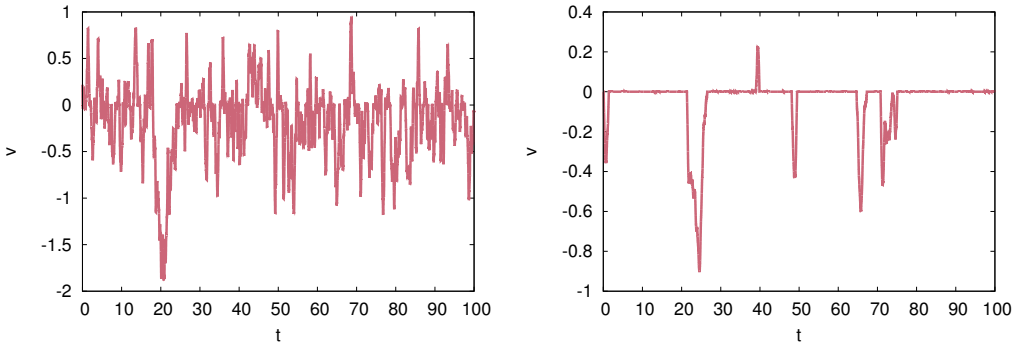

(a) $\tau = 0.1$ (b) $\tau = 1.0$

Figure 4.2: Time traces of the velocity $v(t)$ (Eq. (4.1)) with $\gamma = 1$ and $b = -0.5$ for different values of the noise correlation time: $\tau = 0.1$ (a), $\tau = 1.0$ (b).

In Fig. 4.2(a), we observe a random motion of the velocity, which is similar to Fig. 3.2. For a higher noise correlation time $\tau = 1.0$, sticking phenomena become visible (Fig. 4.2(b)), as already observed for the pure dry friction case, see Fig. 3.3.

This does not come as a surprise since the value of the constant force is smaller than the rescaled dry friction coefficient ($b < 1$) and lies therefore in the sticking regime. In addition, due to the increased correlation time of the noise τ, the stochastic contribution of the total applied force $b + \eta(t)$ attains values which are mostly within in the range $|b + \eta(t)| < 1$. Therefore, it becomes less likely that the total force attains values which are larger than the dry friction coefficient. Thus, we expect the sticking phenomena to dominate the dynamics in the high correlation time limit of τ.

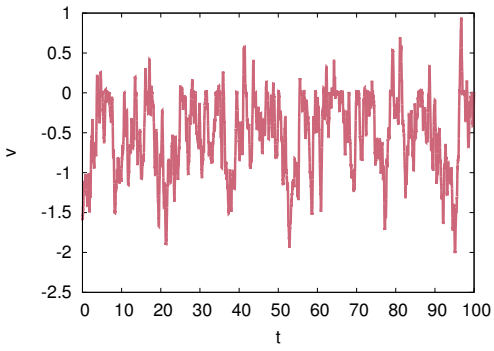

(a) $\tau = 0.1$

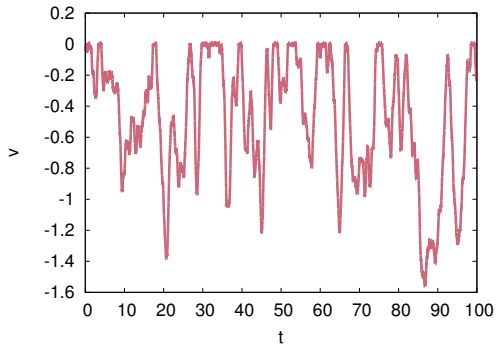

(b) $\tau = 1.0$

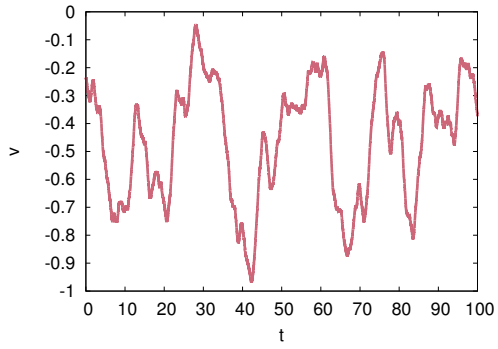

(c) $\tau = 5.0$

Figure 4.3: Time traces of the velocity $v(t)$ (Eq. (4.1)) with $\gamma = 1$ and $b = -1.5$ for different values of the noise correlation time: $\tau = 0.1$ (a), $\tau = 1.0$ (b), $\tau = 5.0$ (c).

On the other hand, for a value above this transition, we expect that the particle never sticks for a long time as the constant force alone can overcome the dry friction coefficient, thus it is large enough to move the particle. This can be observed in Figs. 4.3(a) - 4.3(c), where results are shown for $b = -1.5$. For a small correlation

time, we see a random motion of the velocity as the applied force is large enough to move the particle if it sticks (Fig. 4.3(a)). Short sticking time periods can be observed by further increasing the noise correlation time τ (Fig. 4.3(b)). If we then increase τ even further, the sticking time periods vanishes (Fig. 4.3(c)) and the velocity fluctuates around its deterministic fixed point, which is $v^* = -0.5$ here (see Eq. (4.8), Fig. 4.1 and the parameter values in Fig. 4.3(c)).

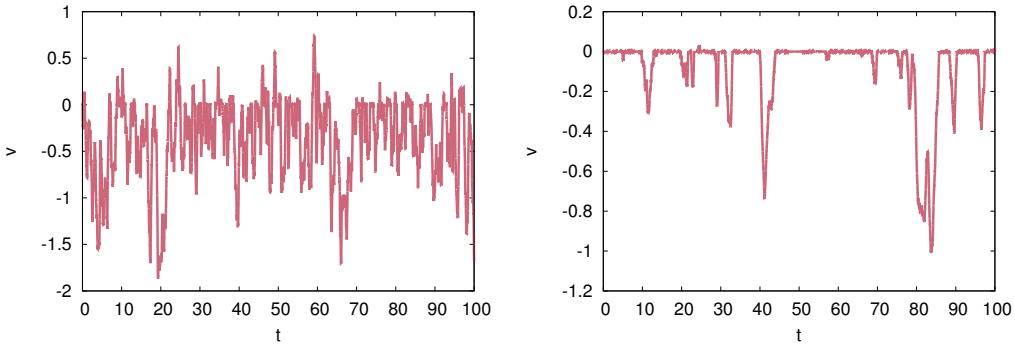

(a) $\tau = 0.1$ (b) $\tau = 1.0$

(c) $\tau = 10.0$ (d) $\tau = 50.0$

Figure 4.4: Time traces of the velocity $v(t)$ (Eq. (4.1)) with $\gamma = 1$ and $b = -1.1$ for different values of the noise correlation time: $\tau = 0.1$ (a), $\tau = 1.0$ (b), $\tau = 10.0$ (c), $\tau = 50.0$ (d).

To investigate the appearance and the vanishing of the sticking time periods for an increasing correlation time of the noise further, we choose a parameter value for the constant force closer to the deterministic stick-slip transition, but still larger than the dry friction coefficient. Figure 4.4 shows time traces of the velocity for $b = -1.1$ and we again vary the noise correlation time τ. For $\tau = 0.1$, we observe a random motion of the velocity, as already seen for $b = -0.5$ (Fig. 4.2(a)) and

$b = -1.5$ (Fig. 4.3(a)). By increasing the noise correlation time further to $\tau = 1.0$, sticking time periods appear (Fig. 4.4(b)), as the total applied force $b+\eta(t)$ seems not to be large enough to move the particle if it has velocity zero. If we then increase τ even further, the sticking time periods become less (Fig. 4.4(c)) until they vanish for very high noise correlation time (Fig. 4.4(d)). Here we could see that the sticking time periods still remain for higher correlation times of the noise if the value of the constant force b is closer to the deterministic stick-slip transition. Overall, the observed phenomenon is quite counterintuitive as one would expect that the total applied force is actually large enough to overcome the dry friction coefficient if we choose a value of the constant force which lies above the stick-slip transition.

To understand this phenomenon in more detail, we investigate the behaviour of the total applied force $b+\eta(t)$ as a function of the correlation time of the noise τ. We recall that $\eta(t)$ describes an Ornstein-Uhlenbeck process (Eq. (4.3)) and is therefore Gaussian distributed with a zero mean $\langle \eta(t) \rangle = 0$ ($\langle \cdots \rangle$ denotes the average over all realisations). Therefore we can conclude that the total applied force is Gaussian distributed around the mean value b. The corresponding dynamical equation for the total applied force is an Ornstein-Uhlenbeck process with an additional constant term (compare to Eq. (4.3))

$$\dot{\eta}(t) = -\frac{\eta(t) - b}{\tau} + \frac{\xi(t)}{\tau}. \tag{4.9}$$

From the corresponding Fokker-Planck equation we can compute the stationary probability density, which reads

$$P_b(\eta) = \sqrt{\frac{\tau}{\pi}} \exp\left(-(\eta - b)^2 \tau\right). \tag{4.10}$$

Eq. (4.10) describes a Gaussian distribution with mean $\langle \eta(t) \rangle = b$ and variance $\langle (\eta - \langle \eta \rangle)^2 \rangle = \frac{1}{2\tau}$. In the white noise limit $\tau \to 0$ and for small correlation times of the noise, the variance is large and therefore the fluctuations $\eta(t)$ around the constant force b can attain large values. By increasing the correlation time τ, the variance of the distribution becomes smaller and the fluctuations around the mean b also decrease. For high correlation times of the noise, the entire dynamic takes place in a small region around the mean b of the total applied force as $\eta(t)$ almost vanishes.

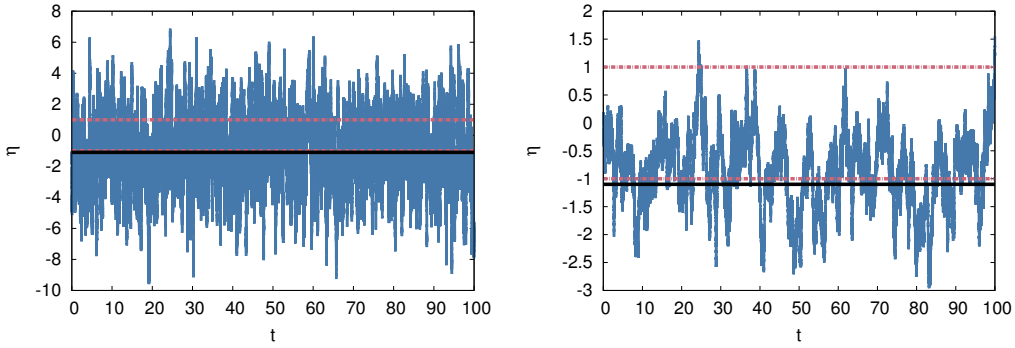

(a) $\tau = 0.1$

(b) $\tau = 1.0$

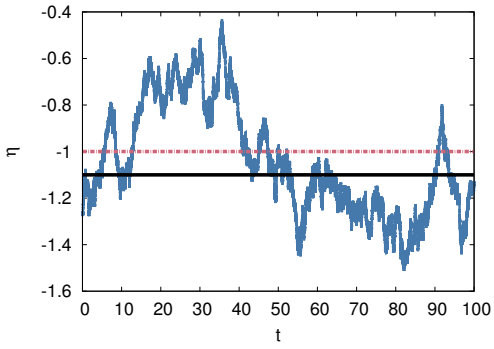

(c) $\tau = 10.0$

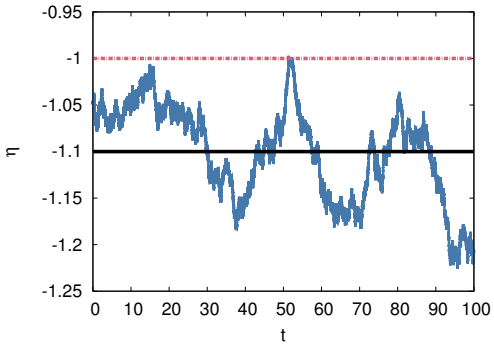

(d) $\tau = 50.0$

Figure 4.5: Time traces of the applied force $b + \eta(t)$ (Eq. (4.9)) with $b = -1.1$ for different values of the noise correlation time τ, obtained numerically. The red dot-dashed lines at -1 and 1 represent the boundaries of the sticking interval, where the attained values are not large enough to move the particle, if it has velocity zero. The black solid line represents the value of b, which is the mean of the total applied force (see Eq. (4.10)).

To visualize this, we show time traces of the total applied force $b + \eta(t)$ for increasing correlation times of the noise τ in Fig. 4.5. For small correlation times (here $\tau = 0.1$), the total applied force attains high values as already mentioned, see Fig. 4.5(a). If it attains values within the sticking interval $[-1, 1]$ (represented by the red lines in Fig. 4.5), usually at one of the next time steps it has left this region and therefore the particle does not stick or sticks only for a very short time. This gives rise to a random motion of the velocity, as already seen in Fig. 4.4(a). Increasing the correlation time τ further (see Fig. 4.5(b)), we observe that the dynamics of the total applied force takes place for longer times within the sticking interval $[-1, 1]$,

which results in the rise of sticking phenomena, see Fig. 4.4(b). By increasing τ even further to $\tau = 10.0$, the total applied force attains only values which lie around the lower bound of the already mentioned interval $[-1, 1]$ and enters it only occasionally. That is why we still can observe sticking phenomena, but for shorter time intervals compared to the case of $\tau = 1.0$, see Figs. 4.4(b) and 4.4(c). And for very high values of τ, the dynamics of the force does not take place anymore within the interval, but only outside in a small range around the mean $b = -1.1$, which is represented by the black line in all Figs. 4.5(a) - 4.5(d). Therefore the particle does not stick anymore, and the velocity attains values close to the deterministic fixed point, which is $v^* = -0.1$ here (see Fig. 4.4(d) and Eq. (4.8)).

In the above discussion, we did not include changes in the viscous friction parameter γ. If we were to increase the values of the viscous friction, we would expect the velocity to attain smaller values. Furthermore, it is reasonable to expect more sticking time periods to occur as the particle is more likely to have zero velocity and the dynamics of the total applied force $b + \eta(t)$ takes place for long times within the above mentioned interval $[-1, 1]$. For low viscous friction, we would expect the opposite. We will investigate the role that γ plays related to the sticking phenomena in the following sections.

4.2 Stationary behaviour

After the discussion on the results from numerical simulations for the time traces and having explored the appearance and the vanishing of sticking time periods, we want to proceed by investigating the stationary properties of our stochastic model. In particular, we calculate the stationary probability distributions, i.e. the marginal distribution $P(v)$ and the joint distribution $P(v, \eta)$. In addition, we compute the probability current from numerical simulations. Taking into account the previously shown results in Sec. 4.1 and from Chapter 3, we expect again a Dirac δ contribution in the expression for the marginal distribution, which represents the appearance of sticking events. However, for values of the constant force b above the deterministic stick-slip transition this contribution might undergo some changes depending on the value of the correlation time of the noise τ. Thus, we want to investigate whether the observed phenomenon concerning the sticking time events is reflected in the results

for the stationary probability distributions.

4.2.1 Marginal probability distribution

To obtain an analytical expression for the stationary marginal probability density $P(v)$, we apply again the unified coloured noise approximation (see Secs. 2.2 and 3.2.1 for detailed calculations) to our system (Eqs. (4.2) and (4.3)) and we obtain

$$\begin{aligned} P(v) &= N^{-1} \exp\left[-2\int (\sigma_\varepsilon(v) + \gamma v - b)\, dv - \tau(\sigma_\varepsilon(v) + \gamma v - b)^2\right] \\ &\quad \times \left[1 + \tau(\gamma + \sigma'_\varepsilon(v))\right] \end{aligned} \tag{4.11}$$

where N is the normalisation constant. The computation of the normalisation constant is a bit more tedious than in the previous chapter. We start again with the regular part, which does not include the term $\sigma'_\varepsilon(v)$ as this term reflects the singular contribution of the density. For the regular part, we can perform the dry friction limit $\varepsilon \to 0$ and integrate the expression in the exponent of Eq. (4.11) (see Eq. (3.12) as well). Thus, to obtain the normalisation constant corresponding to the regular part of the distribution, we have to compute

$$\begin{aligned} N_{Reg} &= \int_{-\infty}^{\infty} \exp\left[-2\left(|v| + \frac{\gamma}{2}v^2 - bv\right) - \tau(\sigma_0(v) + \gamma v - b)^2\right](1 + \tau\gamma)dv \\ &= \int_{0}^{\infty} \exp\left[-2\left(v + \frac{\gamma}{2}v^2 - bv\right) - \tau(1 + \gamma v - b)^2\right](1 + \tau\gamma)dv \\ &\quad + \int_{-\infty}^{0} \exp\left[-2\left(-v + \frac{\gamma}{2}v^2 - bv\right) - \tau(-1 + \gamma v - b)^2\right](1 + \tau\gamma)dv. \end{aligned} \tag{4.12}$$

Since these integrals include Gaussian functions, we obtain straightforwardly for the positive half space

$$\int_0^\infty \exp\left(-\alpha_1 v^2 + \alpha_2 v + \alpha_3\right) dv = \frac{\sqrt{\pi}}{2\sqrt{\alpha_1}} \exp\left(\frac{\alpha_2^2}{4\alpha_1} + \alpha_3\right) \operatorname{erfc}\left(\frac{-\alpha_2}{2\sqrt{\alpha_1}}\right) \tag{4.13}$$

with the coefficients

$$\alpha_1 = \gamma^2\tau + \gamma,\ \alpha_2 = 2(-1 + b - \gamma\tau + b\gamma\tau),\ \alpha_3 = -\tau(1 - 2b + b^2). \tag{4.14}$$

For the negative half-space we have

$$\int_{-\infty}^{0} \exp\left(-\beta_1 v^2 + \beta_2 v + \beta_3\right) dv = \frac{\sqrt{\pi}}{2\sqrt{\beta_1}} \exp\left(\frac{\beta_2^2}{4\beta_1} + \beta_3\right) \operatorname{erfc}\left(\frac{\beta_2}{2\sqrt{\beta_1}}\right) \tag{4.15}$$

with the coefficients

$$\beta_1 = \gamma^2\tau + \gamma,\ \beta_2 = 2(1 + b + \gamma\tau + b\gamma\tau),\ \beta_3 = -\tau(1 + 2b + b^2) \tag{4.16}$$

and we have used the complementary error function

$$\begin{aligned} \operatorname{erfc}(z) &= 1 - \operatorname{erf}(z) \\ &= \frac{2}{\sqrt{\pi}} \int_z^{\infty} e^{-y^2} dy. \end{aligned} \tag{4.17}$$

Finally, we obtain

$$\begin{aligned} N_{Reg} &= \frac{\sqrt{\pi}}{2}\sqrt{\tau + \frac{1}{\gamma}} \left[\exp\left(\frac{(b-1)^2}{\gamma}\right) \operatorname{erfc}\left((1-b)\sqrt{\tau + \frac{1}{\gamma}}\right)\right. \\ &+ \left. \exp\left(\frac{(b+1)^2}{\gamma}\right) \operatorname{erfc}\left((b+1)\sqrt{\tau + \frac{1}{\gamma}}\right)\right]. \end{aligned} \tag{4.18}$$

To check the consistency of Eq. (4.18) with the previous chapter, we consider the result for vanishing viscous friction and vanishing constant force. Performing the limit $b \to 0$ gives

$$\lim_{b\to 0} N_{Reg} = \sqrt{\pi} \exp\left(\frac{1}{\gamma}\right) \sqrt{\tau + \frac{1}{\gamma}} \operatorname{erfc}\left(\sqrt{\tau + \frac{1}{\gamma}}\right). \tag{4.19}$$

To facilitate the computation of the limit $\gamma \to 0$, we substitute $\vartheta = \frac{1}{\gamma}$ and compute the limit $\vartheta \to \infty$

$$\begin{aligned} \lim_{\vartheta\to\infty} N_{Reg} &= \sqrt{\pi} \exp(\vartheta) \sqrt{\tau + \vartheta} \operatorname{erfc}\left(\sqrt{\tau + \vartheta}\right) \\ &= \sqrt{\pi} \exp(\vartheta) \sqrt{\tau + \vartheta} \frac{\exp(-\tau - \vartheta)}{\sqrt{\tau + \vartheta}\sqrt{\pi}} \\ &= \exp(-\tau), \end{aligned} \tag{4.20}$$

which is the same result as in Sec. 3.2.1, see Eq. (3.12). Here, we have used the

asymptotic expression of the complementary error function

$$\lim_{x\to\infty} \operatorname{erfc}(x) = \frac{\exp\left(-x^2\right)}{x\sqrt{\pi}}. \tag{4.21}$$

For the normalisation of the singular part of the distribution in Eq. (4.11), we have to calculate

$$N_{Sing} = \int_{-\infty}^{\infty} \exp\left[-2\left(|v| + \frac{\gamma}{2}v^2 - bv\right) - \tau(\sigma_\varepsilon(v) + \gamma v - b)^2\right] \tau\sigma'_\varepsilon(v)dv. \tag{4.22}$$

Similarly to Sec. 3.2.1, some care is needed in this calculation as in the dry friction limit a singular and a discontinuous contribution are present (see Eq. (3.10)). As this integral gives only a contribution around $v = 0$ due to the singular part, we just need to compute

$$N_{Sing} = \int_{-\infty}^{\infty} \exp\left[-\tau(\sigma_\varepsilon(v) - b)^2\right] \tau\sigma'_\varepsilon(v)dv. \tag{4.23}$$

Since the value of the integral in Eq. (4.23) should be the same for the smoothed expression and for the expression in the dry friction limit $\varepsilon \to 0$, we have to perform the limit for the entire integrand and not for each part of the expression independently. We substitute $\sqrt{\tau}(\sigma_\varepsilon(v) - b) = x$ and obtain

$$\begin{aligned} N_{Sing} &= \int_{\sqrt{\tau}(-1+b)}^{\sqrt{\tau}(1+b)} \sqrt{\tau}\exp\left[-x^2\right] dx \\ &= \int_{0}^{\sqrt{\tau}(1+b)} \sqrt{\tau}\exp\left[-x^2\right] dx - \int_{0}^{\sqrt{\tau}(-1+b)} \sqrt{\tau}\exp\left[-x^2\right] dx \\ &= \frac{\sqrt{\pi\tau}}{2}\left(\operatorname{erf}\left[\sqrt{\tau}(1+b)\right] - \operatorname{erf}\left[\sqrt{\tau}(-1+b)\right]\right). \end{aligned} \tag{4.24}$$

Here, we have used again the error function

$$\operatorname{erf}(z) = \frac{2}{\sqrt{\pi}}\int_0^z e^{-y^2}dy. \tag{4.25}$$

This result does not depend on γ, as only the parameters b and τ are connected to the total applied force and therefore related to the stick-slip transitions.

Thus, our complete normalisation constant reads

$$\begin{aligned} N &= N_{Reg} + N_{Sing} \\ &= \frac{\sqrt{\pi}}{2}\sqrt{\tau+\frac{1}{\gamma}}\left[\exp\left(\frac{(b-1)^2}{\gamma}\right)\operatorname{erfc}\left((1-b)\sqrt{\tau+\frac{1}{\gamma}}\right)\right. \\ &\quad + \left.\exp\left(\frac{(b+1)^2}{\gamma}\right)\operatorname{erfc}\left((b+1)\sqrt{\tau+\frac{1}{\gamma}}\right)\right] \\ &\quad + \frac{\sqrt{\pi\tau}}{2}\left(\operatorname{erf}\left[\sqrt{\tau}(1+b)\right]-\operatorname{erf}\left[\sqrt{\tau}(-1+b)\right]\right). \end{aligned} \tag{4.26}$$

The normalised regular part of the probability distribution in the dry friction limit $\varepsilon \to 0$ is therefore

$$P_{Reg}(v) = N^{-1}\exp\left[-2\left(|v|+\frac{\gamma}{2}v^2-bv\right)-\tau(\sigma_0(v)+\gamma v-b)^2\right](1+\tau\gamma). \tag{4.27}$$

In Figs. 4.6 and 4.7, the comparison between the regular part of the analytical estimate (Eq. (4.27)) for the stationary probability density and numerical simulations is shown. In Fig. 4.6 we set $\gamma = 1.0$ in all subfigures and in Fig. 4.7 we have $\gamma = 10.0$. In the left column of both figures the correlation time τ is fixed to $\tau = 0.1$ and we vary the constant force b. In the right column of both figures τ is fixed as well, but here we have $\tau = 1.0$ and we vary the constant force. Thus, in each of the columns the correlation time is fixed, whereas in each of the rows the constant force is fixed. Both figures exhibit three different cases for the constant force b: the subfigures (a) and (b) show the case of $b = 0$, (c) and (d) represent the case of $b = -0.5$ (sticking regime), and (e) and (f) denotes the case of $b = -1.5$ (sliding regime). For the correlation time we just show results for $\tau = 0.1$ and $\tau = 1.0$ as the expression from Eq. (4.27) becomes exact in the white noise limit $\tau \to 0$.

The approximation works quite well for moderate viscous friction and gives promising results, although deviations become visible between numerics and analytics for $\tau = 1.0$ and for $\tau = 0.1$ around $v = 0$, where we have the transition between the regular and the singular part of the probability distribution. In the case of high viscous friction, we observe an even better agreement between the numerical and analytical results. Although deviations around $v = 0$ are clearly visible for $\tau = 0.1$, as we increase the correlation time of the noise further, the results match more or less perfectly. The reason for the better performance of the approximation

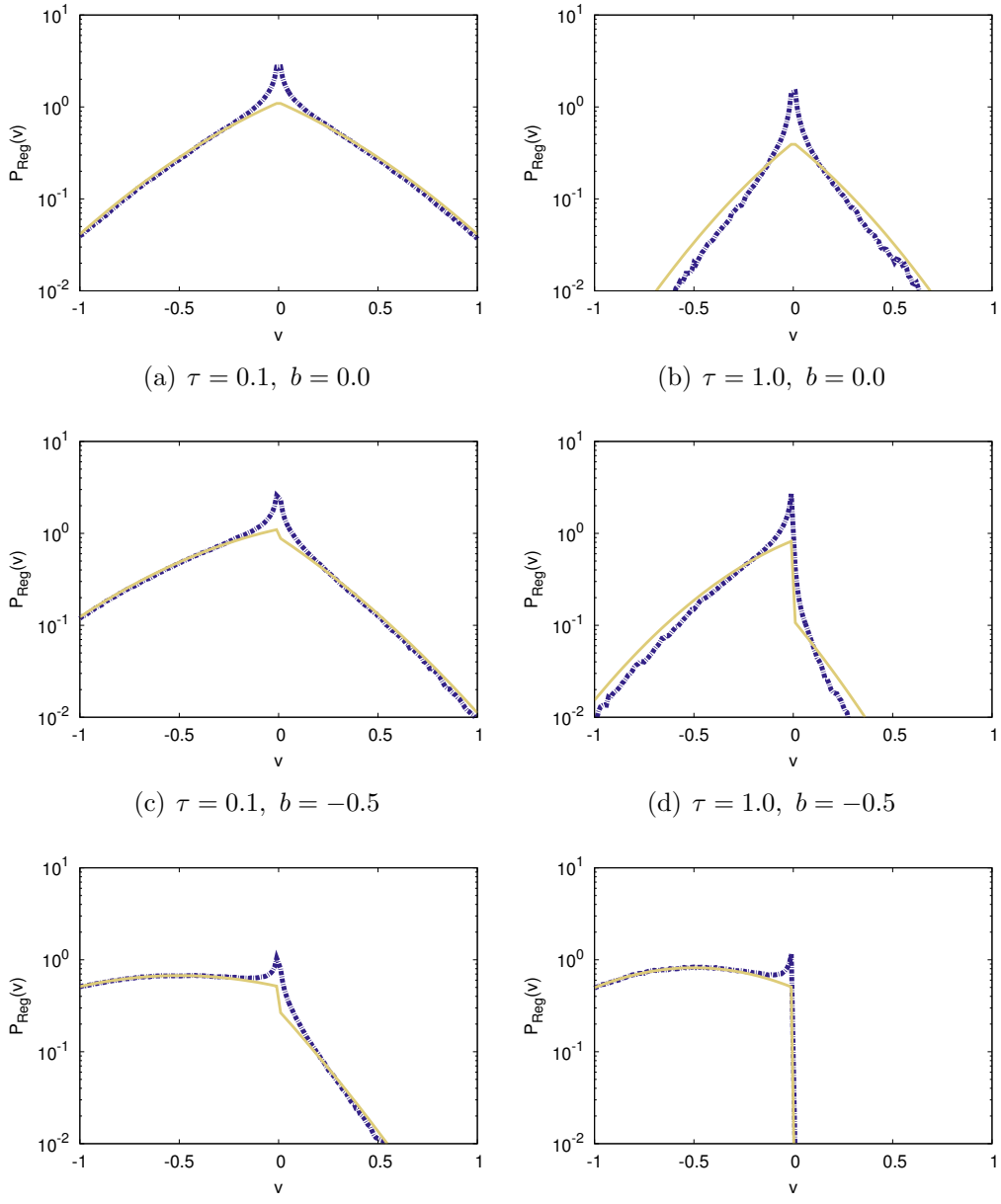

(a) $\tau = 0.1,\ b = 0.0$ (b) $\tau = 1.0,\ b = 0.0$

(c) $\tau = 0.1,\ b = -0.5$ (d) $\tau = 1.0,\ b = -0.5$

(e) $\tau = 0.1,\ b = -1.5$ (f) $\tau = 1.0,\ b = -1.5$

Figure 4.6: Regular part of the stationary probability density $P_{Reg}(v)$, from the analytical estimate (Eq. (4.27)), yellow solid line) and numerically calculated (Eqs. (4.1) and (4.3), blue dot-dashed line) for different values of the constant force: $b = 0.0$ (a),(b), $b = -0.5$ (c),(d), $b = -1.5$ (e),(f) and different values of the noise correlation time $\tau = 0.1$ (left column), $\tau = 1.0$ (right column) and moderate viscous friction $\gamma = 1.0$.

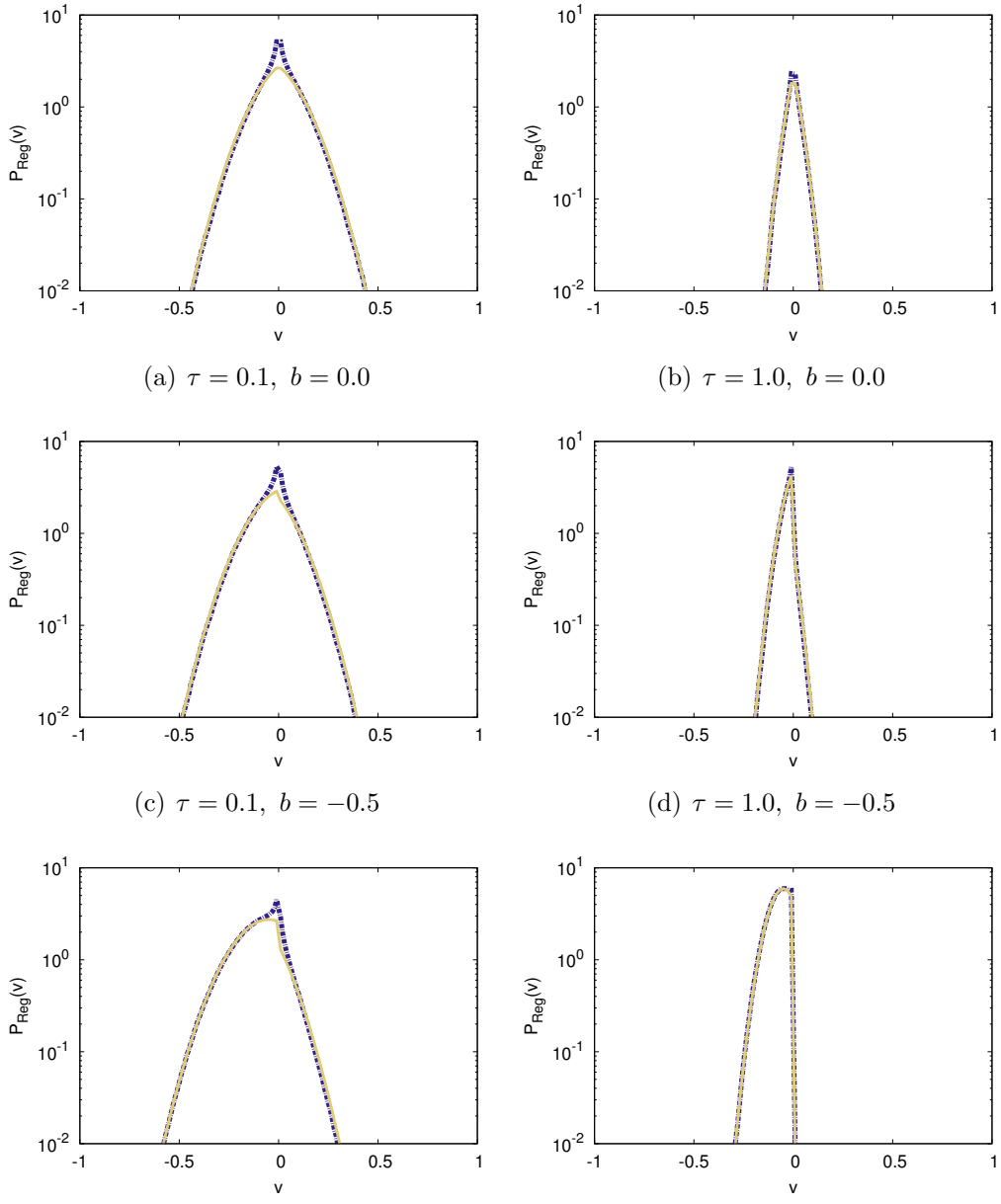

(a) $\tau = 0.1,\ b = 0.0$ (b) $\tau = 1.0,\ b = 0.0$

(c) $\tau = 0.1,\ b = -0.5$ (d) $\tau = 1.0,\ b = -0.5$

(e) $\tau = 0.1,\ b = -1.5$ (f) $\tau = 1.0,\ b = -1.5$

Figure 4.7: Regular part of the stationary probability density $P_{Reg}(v)$, from the analytical estimate (Eq. (4.27)), yellow solid line) and numerically calculated (Eqs. (4.1) and (4.3), blue dot-dashed line) for different values of the constant force: $b = 0.0$ (a),(b), $b = -0.5$ (c),(d), $b = -1.5$ (e),(f) and different values of the noise correlation time $\tau = 0.1$ (left column), $\tau = 1.0$ (right column) and high viscous friction $\gamma = 10.0$.

for high viscous friction is very likely to be found if we have a look at the artificial damping factor β from the unified coloured noise approximation (Eq. (2.34)). Here, it is given by

$$\beta(v,\tau) = \frac{1}{\sqrt{\tau}} + \sqrt{\tau}(\gamma + \sigma_\varepsilon'(v)). \tag{4.28}$$

As mentioned in the Secs. 2.2 and 3.2.1, we expect the approximation to work well if the condition $\beta(v,\tau) \gg 1$ is fulfilled. For the pure dry friction case ($\gamma = 0$), we observed deviations for values of the correlation time of the noise $\tau \geq 0.1$. The same applies for the case $\gamma = 1.0$, see Fig. 4.6. For high viscous friction $\gamma = 10.0$, the numerical and analytical results almost match perfectly, see Fig. 4.7. In this case, the damping factor (Eq. (4.28)) becomes much larger, therefore the very good agreement does not come as surprise.

For the cases without constant force $b = 0$ (see Figs. 4.6(a), 4.6(b), 4.7(a), 4.7(b)) the influence of the viscous friction becomes visible in comparison to the pure dry friction case (Fig. 3.4) as the tails of the distribution change towards a Gaussian shape (see the v^2 contributions in the exponent in Eq. (4.27)) and decay rapidly for high viscous friction. However, for small velocities v the cusp of the distribution, which is a characteristic of a system with dry friction, is still visible. In the pure dry friction case the distribution is of simple exponential type (see (Fig. 3.4) and Eq. (3.15)).

For the singular part of the distribution (Eq. (4.11)), we only consider the parts, which give a contribution in a small region around $v = 0$

$$P_{Sing} = N^{-1} \exp\left[-\tau(\sigma_\varepsilon(v) - b)^2\right] \tau\sigma_\varepsilon'(v). \tag{4.29}$$

In the same way as in Sec. 3.2.1, we need to find the right pre factor for the Dirac δ function ($\lim_{\varepsilon\to 0} \sigma_\varepsilon'(v) \sim \delta(v)$). Thus, we integrate the expression from Eq. (4.29) in a small region $[-a, a]$ around $v = 0$

$$\begin{aligned} \int_{-a}^{a} \exp\left[-\tau(\sigma_\varepsilon(v) - b)^2\right] \tau\sigma_\varepsilon'(v)dv &= \int_{\sqrt{\tau}(-1+b)}^{\sqrt{\tau}(1+b)} \sqrt{\tau} \exp\left[-x^2\right] dx \\ &= N_{Sing} \end{aligned} \tag{4.30}$$

by again using the substitution $\sqrt{\tau}(\sigma_\varepsilon(v) - b) = x$ and performing the same steps

of the calculation as in Eq. (4.24). The singular part of the distribution is therefore

$$P_{Sing} = \frac{N_{Sing}}{N}\delta(v) \tag{4.31}$$

and the probability of sticking as a function of the correlation time of the noise is

$$P_{Stick}(\tau) = \frac{\sqrt{\pi\tau}}{2N}\left(\mathrm{erf}\left[\sqrt{\tau}(1+b)\right] - \mathrm{erf}\left[\sqrt{\tau}(-1+b)\right]\right). \tag{4.32}$$

N is again the full normalisation constant from Eq. (4.26), including the regular and the singular contributions.

In the following analysis of Eq. (4.32), we first fix $\gamma = 1.0$ and consider scenarios for different values of b. Then, we consider some cases where we keep the constant force fixed and elaborate the influence of the viscous friction by varying γ.

In Figs. 4.8 and 4.9, the analytical estimate (Eq. (4.32)) is compared to numerical simulations for different values of the constant force b and moderate viscous friction ($\gamma = 1$). Again, the approximation works quite well as we can observe a very

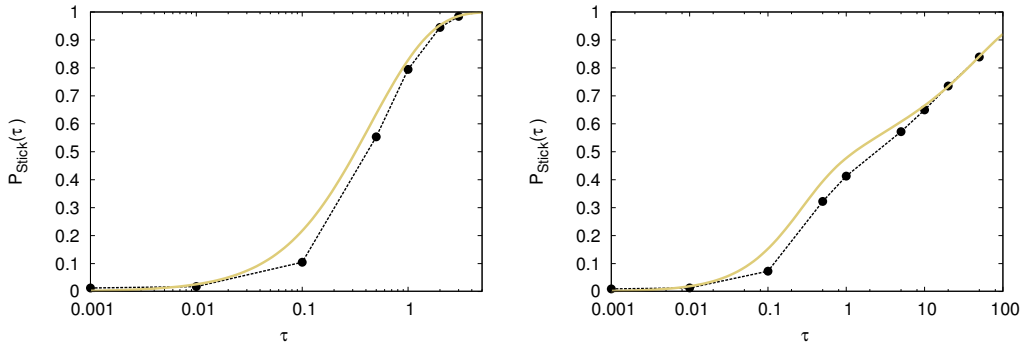

(a) $b = 0.0$ (b) $b = -0.9$

Figure 4.8: Probability of sticking $P_{Stick}(\tau)$ as a function of the correlation time τ for different values of the constant force, $b = 0.0$ (a) and $b = -0.9$ (b). The yellow solid line shows the analytical estimate (Eq. (4.32)), whereas the black dots result from numerical simulations of Eqs. (4.1) and (4.3). Further parameter $\gamma = 1.0$.

good agreement between the analytical results and the numerical simulations. For the values of the constant force b which lie in the sticking regime (Fig. 4.8), the probability of sticking approaches 1 in the high correlation limit. If there is no constant force at present, this happens already at intermediate correlation times τ,

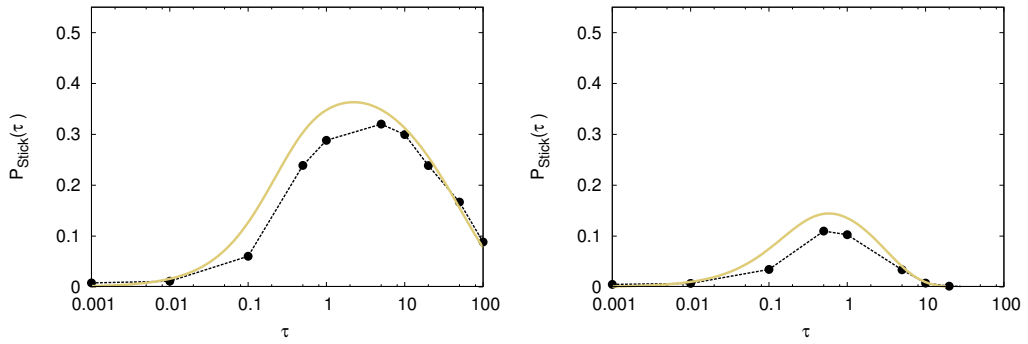

(a) $b = -1.1$ (b) $b = -1.5$

Figure 4.9: Probability of sticking $P_{Stick}(\tau)$ as a function of the correlation time τ for different values of the constant force, $b = -1.1$ (a) and $b = -1.5$ (b). The yellow solid line shows the analytical estimate (Eq. (4.32)), whereas the black dots result from numerical simulations of Eqs. (4.1) and (4.3). Further parameter $\gamma = 1.0$.

whereas if we increase the constant force towards the value of the stick-slip transition, the increase of the sticking probability is much slower, compare Figs. 4.8(a) and 4.8(b). If we compare the case of $b = 0$ and $\gamma = 1$ (Fig. 4.8(a)) with the pure dry friction case (Fig. 3.5) no big difference can be observed from the two figures separately. If these two curves were plotted in one figure, they would only marginally differ for intermediate correlation times.

For values above the transition $|b| > 1$, we observe a non-monotonic behaviour of the probability of sticking as a function of the noise correlation time. In the white noise limit $\tau \to 0$, the probability of sticking is more or less zero. By increasing the correlation time of the noise τ, the $P_{Stick}(\tau)$ increases up to a certain value at an intermediate correlation time τ. If we then increase τ even further, the probability decreases again towards zero. The closer the value of b is to the stick-slip transition ($|b| = 1$), the more pronounced is this phenomenon, compare Figs. 4.9(a) and 4.9(b). Such a behaviour has already been indicated by the results for the time traces in Sec. 4.1, i.e. the appearance and the vanishing of sticking phenomena, see Figs. 4.3 - 4.5.

Next, we want to investigate how the observed non-monotonic behaviour of the probability of sticking is affected by varying the viscous friction coefficient γ. The viscous friction contributes to probability of sticking through the regular normalisation constant N_{Reg} (Eq. (4.18)). In Figs. 4.10(a) and 4.10(b), we show the results

for values of the constant force b above the stick-slip transition, but now for different values of the viscous friction coefficient γ. For low friction ($\gamma = 0.1$), the observed phenomenon is less pronounced and the value of the correlation time τ, where the sticking probability attains its maximum, is shifted towards higher values of τ compared with the intermediate and high viscous friction, see Fig. 4.10(a). If we increase the constant force further, the effect basically vanishes for low friction, see Fig. 4.10(b). On the other hand, for high viscous friction ($\gamma = 10.0$) the non-monotonic behaviour is strongly pronounced. Here, the value of the correlation time τ is shifted towards smaller values of τ compared to the cases of lower friction. Moreover, even if we move away from the stick-slip transition by increasing the constant force b, the effect is still very visible, see Fig. 4.10(b).

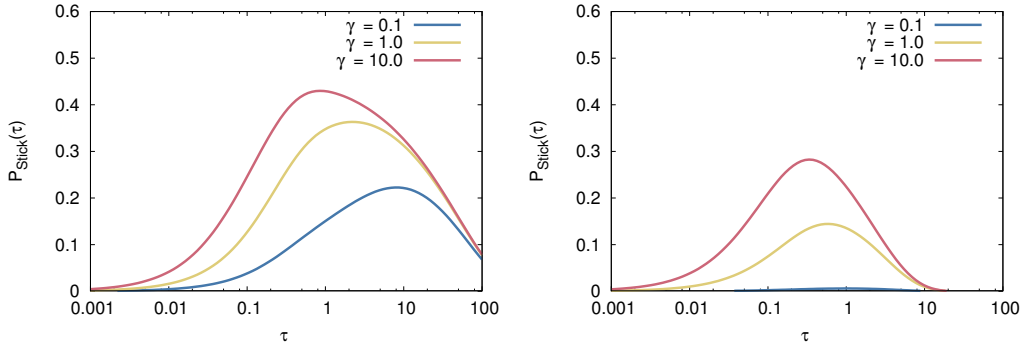

(a) $b = -1.1$ (b) $b = -1.5$

Figure 4.10: Probability of sticking $P_{Stick}(\tau)$ as a function of the correlation time τ for different values of the constant force, $b = -1.1$ (a) and $b = -1.5$ (b). In both figures analytical results from Eq. (4.32) are shown for three different values of the viscous friction coefficient: $\gamma = 10$ (red), $\gamma = 1.0$ (yellow), $\gamma = 0.1$ (blue).

From these results the question arises as to what scenario could be observed for very large viscous friction. Thus, we compute the probability of sticking in the limit $\gamma \to \infty$. The viscous friction enters the probability of sticking via the normalisation

of the regular part of the probability distribution (Eq. (4.18)). Thus, we compute

$$\begin{aligned}\lim_{\gamma\to\infty} N_{Reg} &= \lim_{\gamma\to\infty} \frac{\sqrt{\pi}}{2}\sqrt{\tau+\frac{1}{\gamma}}\left[\exp\left(\frac{(b-1)^2}{\gamma}\right)\operatorname{erfc}\left((1-b)\sqrt{\tau+\frac{1}{\gamma}}\right)\right. \\ &\quad \left. + \exp\left(\frac{(b+1)^2}{\gamma}\right)\operatorname{erfc}\left((b+1)\sqrt{\tau+\frac{1}{\gamma}}\right)\right] \\ &= \frac{\sqrt{\pi\tau}}{2}\left[2+\operatorname{erf}(\sqrt{\tau}(b-1)-\operatorname{erf}(\sqrt{\tau}(b+1))\right]. \end{aligned} \tag{4.33}$$

Here we have used the relations

$$\operatorname{erfc}(-x) = 1 + \operatorname{erf}(x). \tag{4.34}$$

The latter follows since the error function is an odd function. The probability of sticking (Eq. (4.32)) changes therefore to

$$\begin{aligned} P_{Stick}(\tau) &= \frac{N_{Sing}}{N_{Reg}+N_{Sing}} \\ &= \frac{1}{2}\left[\operatorname{erf}\left(\sqrt{\tau}(1+b)\right)-\operatorname{erf}\left(\sqrt{\tau}(-1+b)\right)\right]. \end{aligned} \tag{4.35}$$

A comparison between this result and previously obtained results (Eq. (4.32) and Fig. 4.10) is shown in Fig. 4.11. We observe that the overall difference between the result for $\gamma = 10$ and $\gamma \to \infty$ is small. For small correlation times τ a difference is clearly visible but the larger the correlation time τ the better the curves for different γ coincide, thus the value of γ hardly matters in the high correlation regime. Eq. (4.35) and Fig. 4.11 show that the influence of γ towards a higher probability of sticking is limited, i.e. $P_{Stick}(\tau)$ cannot be increased further and further by increasing γ.

If the viscous friction is very high, the velocity decreases and only small values in the area around the origin $v(t) = 0$ can be observed. If the correlation time of the noise τ lies in a parameter region such that the total applied force $b + \eta(t)$ attains more likely values, which are within the sticking interval (see Eqs. (4.9) and (4.10) and Fig. 4.5 as well), then the probability that the particle sticks ($v(t) = 0$) is increased compared to the cases of lower viscous friction. Therefore, the observed non-monotonic behaviour is more strongly pronounced for high viscous friction.

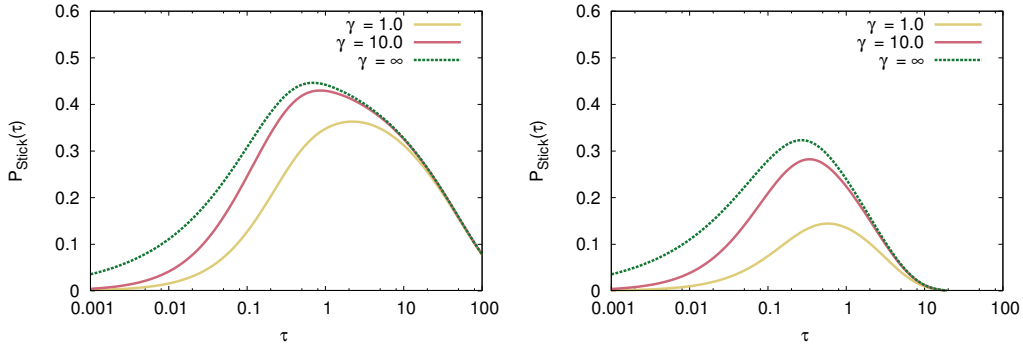

(a) $b = -1.1$ (b) $b = -1.5$

Figure 4.11: Probability of sticking $P_{Stick}(\tau)$ as a function of the correlation time τ for different values of the constant force, $b = -1.1$ (a) and $b = -1.5$ (b). In both figures analytical results from Eq. (4.32) are shown for two different values of the viscous friction coefficient: $\gamma = 10$ (red), $\gamma = 1.0$ (yellow). In addition the result for the limit $\gamma \to \infty$ from Eq. (4.35) is presented (green dashed line).

4.2.2 Joint probability distribution and probability current

After investigating the properties of the marginal distribution of the velocity, we want to proceed with the two-dimensional model (v, η). As in Sec. 3.2.2, we first compute the joint probability distribution numerically as analytical calculations are hampered due to the lack detailed balance. We present results for the case of white noise ($\tau = 0.001$) and for a high correlation time ($\tau = 1.0$). Figs. 4.12 and 4.13 show logarithmic density plots of the full joint probability distribution, i.e. the regular and the singular part. The figures are similarly organised as Figs. 4.6 and 4.7. In each column the correlation time is fixed, whereas in each row we have the same value of the constant force. Fig. 4.12 results are shown for $\gamma = 1.0$, whereas we have $\gamma = 10.0$ in Fig. 4.13.

For $b = 0$ and $\tau = 0.001$ (Figs. 4.12(a) and 4.13(a)), we have a Gaussian distribution in the η direction and the distribution in v is $\sim \exp(-2|v| - \gamma v^2)$. If we increase the correlation time of the noise τ, the two parts in the half spaces are shifted against each other, as already seen for the pure dry friction case (see Fig. 3.6). For $\tau = 1.0$, the position of the distribution in the (v, η) plane changes as well due to the additional viscous friction. For pure dry friction, the regular part of the probability distribution attains its maximum value more or less around the same value in η (to be more precise it is around $\eta = \sigma(v) = \pm 1$) as we move away from

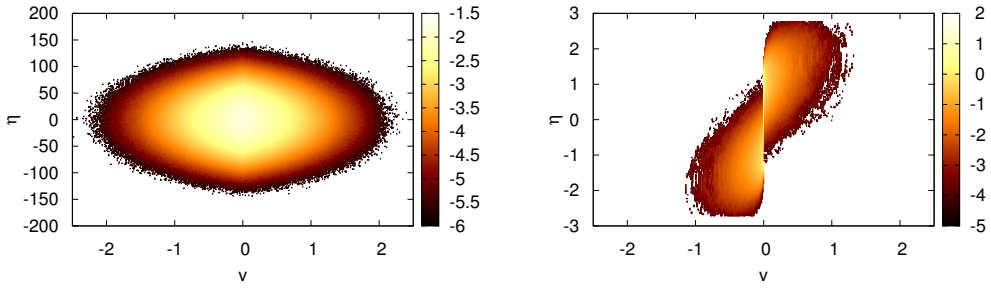

(a) $\tau = 0.001,\ b = 0.0$

(b) $\tau = 1.0,\ b = 0.0$

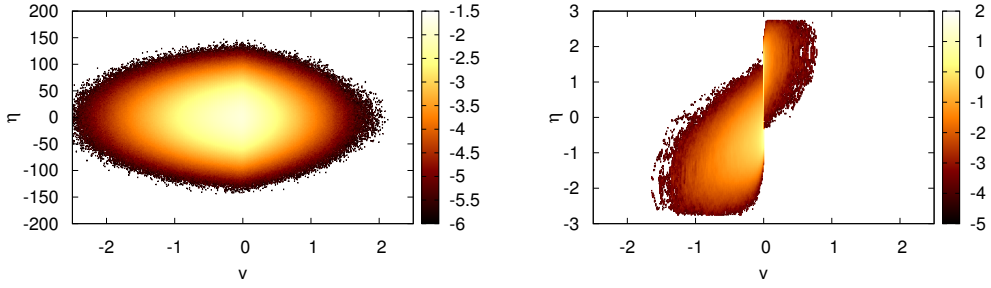

(c) $\tau = 0.001,\ b = -0.5$

(d) $\tau = 1.0,\ b = -0.5$

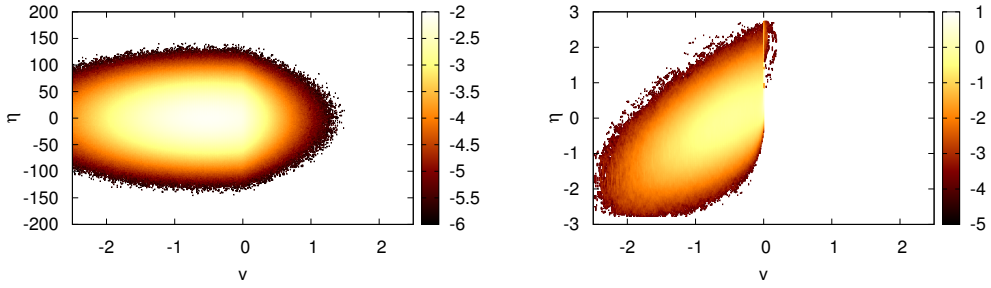

(e) $\tau = 0.001,\ b = -1.5$

(f) $\tau = 1.0,\ b = -1.5$

Figure 4.12: Logarithmic density plot of the stationary probability distribution, obtained from numerical simulations of Eqs. (4.1) and (4.3) for different values of the correlation time $\tau = 0.001$ (left column), $\tau = 1.0$ (right column) and different values of the constant bias: $b = 0.0$ (a),(b), $b = -0.5$ (c),(d), $b = -1.5$ (e),(f). Further parameter $\gamma = 1.0$.

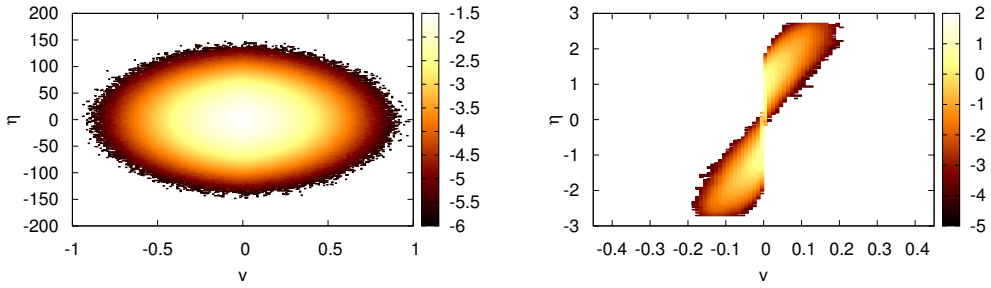

(a) $\tau = 0.001,\ b = 0.0$ (b) $\tau = 1.0,\ b = 0.0$

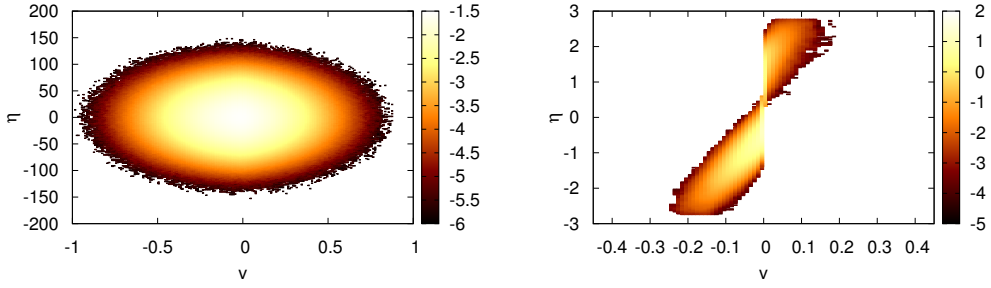

(c) $\tau = 0.001,\ b = -0.5$ (d) $\tau = 1.0,\ b = -0.5$

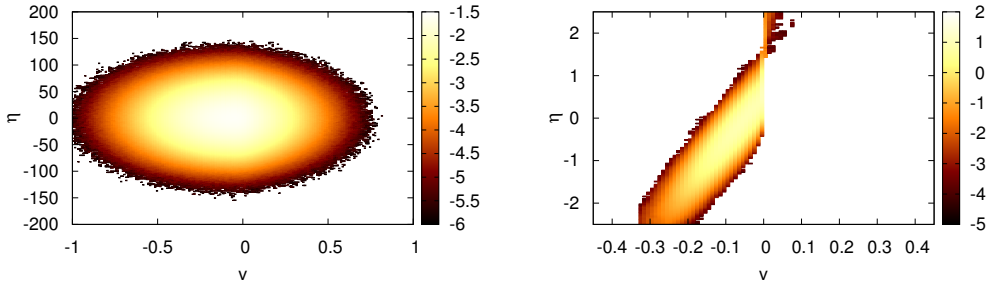

(e) $\tau = 0.001,\ b = -1.5$ (f) $\tau = 1.0,\ b = -1.5$

Figure 4.13: Logarithmic density plot of the stationary probability distribution, obtained from numerical simulations of Eqs. (4.1) and (4.3) for different values of the correlation time $\tau = 0.001$ (left column), $\tau = 1.0$ (right column) and different values of the constant bias: $b = 0.0$ (a),(b), $b = -0.5$ (c),(d), $b = -1.5$ (e),(f). Further parameter $\gamma = 10.0$.

the discontinuity located at $v = 0$, see Fig. 3.6(c). In the case of the viscous friction, the maximum value of the regular part of the distribution changes its position in η to more positive or more negative values as we move away from the discontinuity, either towards positive velocities or negative velocities. This effect becomes clearly visible for $b \neq 0$, see Fig. 4.12(f).

Another obvious impact of the additional viscous friction compared to the pure dry friction case is that the higher the values of γ, the smaller the possible values for the velocity. For example in Fig. 4.13(a) (with $\gamma = 10.0$), the distribution is more or less zero for velocities larger than $v = \pm 1$. For $\gamma = 1.0$ in Fig. 4.12(a), the range of the probability distribution, where results are visible from the numerical simulation, is $v \in [-2, 2]$. Moreover, for pure dry friction (Fig. 3.6(a)) the range of the distribution goes even beyond $v = \pm 2$.

In general, the dynamics is biased towards one of the half spaces for $b \neq 0$, depending on the sign of the constant force b; here it is towards the negative velocity domain. For a higher noise correlation time we observe that the stronger the constant force, the more the dynamics takes place in the respective half space or the lesser the dynamics takes place in the other half space, e.g. see Fig. 4.12(f), where almost the entire joint probability distribution is located in the negative velocity domain. The results for high viscous friction (Fig. 4.13) exhibit the same changes of the joint probability distribution, previously described for moderate viscous friction. Furthermore, the distribution is located at lower values of the velocity, as already mentioned before and seen for the marginal distribution in Fig. 4.7.

Having discussed results from numerical simulations, we want to obtain some more insight with the focus on analytical results. As the two-dimensional system in (v, η) represents a Markov process, we can write down the corresponding Fokker-Planck equation. From Eqs. (4.2) and (4.3)) we get

$$\begin{aligned} \frac{\partial}{\partial t} P(v, \eta, t | v_0, \eta_0, 0) &= \frac{\partial}{\partial v} (\sigma_\varepsilon(v) + \gamma v - b - \eta) P(v, \eta, t | v_0, \eta_0, 0) \\ &\quad + \frac{\partial}{\partial \eta} \left(\frac{\eta}{\tau} + \frac{1}{2\tau^2} \frac{\partial}{\partial \eta} \right) P(v, \eta, t | v_0, \eta_0, 0). \end{aligned} \tag{4.36}$$

We have used the smoothed version of the dry friction here (see Eq. (3.4)). Due to the lack of detailed balance, there is no straightforward method to solve Eq. (4.36). We have tried similar attempts as in Sec. 3.2.2 to find the stationary probability

distribution but without success. However, similarly to Eq. (3.29), it is possible to find an expression for the stationary joint distribution $P(v, \eta)$, which formally solves Eq. (4.36) in the dry friction limit $\varepsilon \to 0$

$$P(v,\eta) = \exp\left[-2(\gamma\tau+1)^2(|v|-bv) + 2\eta\left(\gamma\tau^2+\tau\right)(\sigma_0(v)-b) \right. \\ \left. +2\eta v\left(\gamma^2\tau^2+\gamma\tau\right) - \eta^2\left(\gamma\tau^2+\tau\right) - \gamma v^2(\gamma\tau+1)^2\right]. \tag{4.37}$$

Unfortunately, this expression does not obey the required matching conditions at $v = 0$. Nevertheless, it turns out that it is a useful analytical estimate for large values of velocity v and large noise amplitudes η. A comparison to numerical simulations is shown in Figs. 4.14 and 4.15, where slices at constant velocity and slices for constant noise amplitude are taken to check the validity of the expression from Eq. (4.37). The normalisation constant cannot be computed as the result in Eq. (4.37) only takes the sliding dynamics for large velocities and large noise amplitudes into account. However, the full probability distribution contains also a singular part, which contributes to the normalisation as well, see e.g. Eq. (4.26).

As a check of consistency we observe that for $b = 0$ and $\gamma = 0$, Eq. (4.37) changes to Eq. (3.29), which is the pure dry friction case. Furthermore, for $b = 0$ and without the contributions of the dry friction, i.e. $|v|$ and $\sigma_0(v)$, Eq. (4.37) coincides with the result for the Ornstein-Uhlenbeck process driven by coloured noise (Eq. (2.21)).

In both figures, we observe that the expression from Eq. (4.37) coincides very well for the case of large velocity and large noise amplitude. The closer we approach the discontinuity at $v = 0$, the more deviations between numerical and analytical results become visible. In Fig. 4.14 the numerical result closest to the discontinuity exhibits a stronger decay than the analytical estimate and the shape of the distribition becomes asymmetric around its maximum value. For constant noise amplitudes in Fig. 4.15, the analytical expressions fit quite nicely with the numerical results in the negative half space, but they fail to give a valid result for the positive domain with the exception of the case for the largest negative noise amplitude.

To close this section, we compute the stationary probability current numerically with the previously used algorithm [56]. This quantity clearly shows the nonequilibrium character of our system as it does not vanish for $\tau \neq 0$. Here we only present results for moderate viscous friction ($\gamma = 1.0$), high constant bias ($b = -1.5$) and two different values of the noise correlation time (stream plots in Fig. 4.16 and

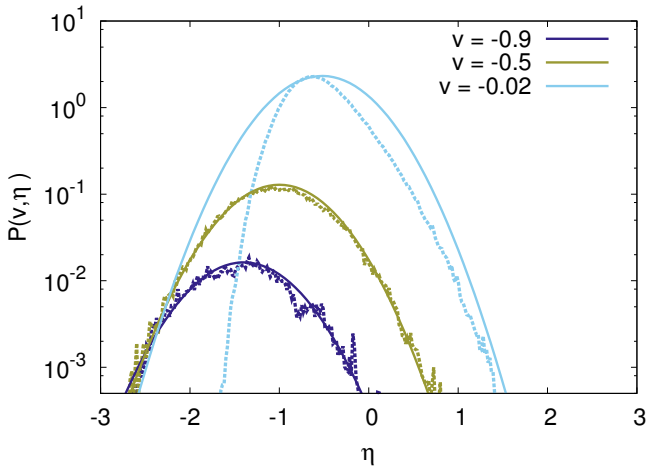

Figure 4.14: Regular component of the stationary probability distribution at fixed values of the velocity v for $\tau = 1.0$, $\gamma = 1.0$ and $b = -0.5$. The numerical simulations (dashed lines) are compared with the analytical estimate (solid lines) (Eq. (4.37)). The normalisation of the analytics is fitted to the numerical data.

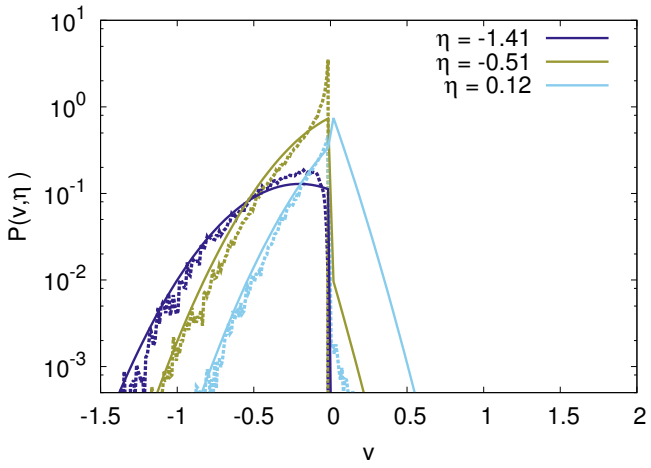

Figure 4.15: Regular component of the stationary probability distribution at fixed values of the noise amplitude η for $\tau = 1.0$, $\gamma = 1.0$ and $b = -0.5$. The numerical simulations (dashed lines) are compared with the analytical estimate (solid lines) (Eq. (4.37)). The normalisation of the analytics is fitted to the numerical data.

logarithmic density plots in Fig. 4.17). Due to the negative value of the constant force, the larger part of the dynamics takes place in the negative half space. The flow pattern seems to circulate around the point $(v, \eta) = (-0.5, 0)$ (see Fig. 4.16). This looks similar to the case of the Ornstein-Uhlenbeck process driven by coloured

noise, see Fig. 2.2 in Sec. 2.1, where the probability current rotates around the origin $(0, 0)$ in the (v, η) plane. The difference between these two pictures is obviously the impact of the discontinuity at $v = 0$. Note that the sticking interval is located at $v = 0$ and $\eta \in [0.5, 2.5]$.

For negative values of η and small negative velocities v the probability current points towards larger negative velocities and larger negative noise amplitudes. Due to the impact of the viscous friction the particle gets decelerated. If η becomes now smaller and changes its sign, it somehow opposes the constant force. Therefore, the current points towards larger positive values of η and more importantly towards $v = 0$. As the particle reaches $v = 0$ the particle enters the sticking manifold if we have $\eta \in [0.5, 2.5]$ (as the sticking condition in Eq. (4.4) is fulfilled then). On the sticking manifold, the current points towards the positive or negative direction depending on the value of η, see Fig. 4.18 for the probability current on the sticking manifold. If η attains again a value outside the aforementioned sticking interval, the particle starts sliding again. In the case of $\tau = 1.0$ (Fig. 4.16(b)), the probability current is more or less only located in the negative half space of the velocity, whereas for $\tau = 0.1$, the particle can enter the positive half space for the velocity.

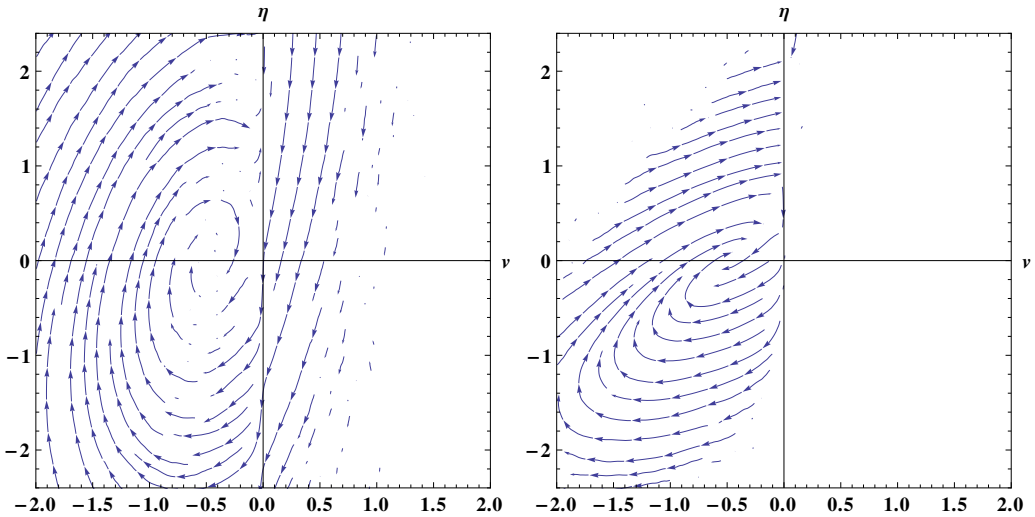

(a) $\tau = 0.1$ (b) $\tau = 1.0$

Figure 4.16: Stream plot of the regular part of the stationary probability current from numerical simulations for $\gamma = 1.0$, $b = -1.5$, $\tau = 0.1$ (a) and $\tau = 1.0$ (b). The stream plot shows the normalised vector field of the current in the (v, η) plane.

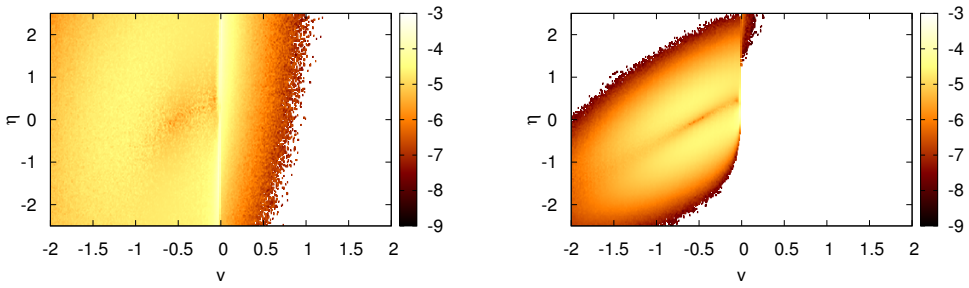

(a) $\tau = 0.1$ (b) $\tau = 1.0$

Figure 4.17: Logarithmic density plot of the regular part of the stationary probability current from numerical simulations for $\gamma = 1.0$, $b = -1.5$, $\tau = 0.1$ (a) and $\tau = 1.0$ (b). The density plot exhibits the absolute value of the current in the (v, η) plane.

Next, we want to investigate further whether the constant force b has an impact on the probability current on the sticking manifold, i.e. the η-component of the stationary probability current $J(v, \eta)$ at $v = 0$ and $\eta \in [-1-b, 1-b]$ (see Eq. (4.4)). As in Fig. 3.12, we consider results for the current on the sticking manifold by varying the correlation time of the noise τ. Numerical results are shown for two different values of the constant force b, one in the sticking regime (Fig. 4.18(a)) and one in the sliding regime (Fig. 4.18(b)).

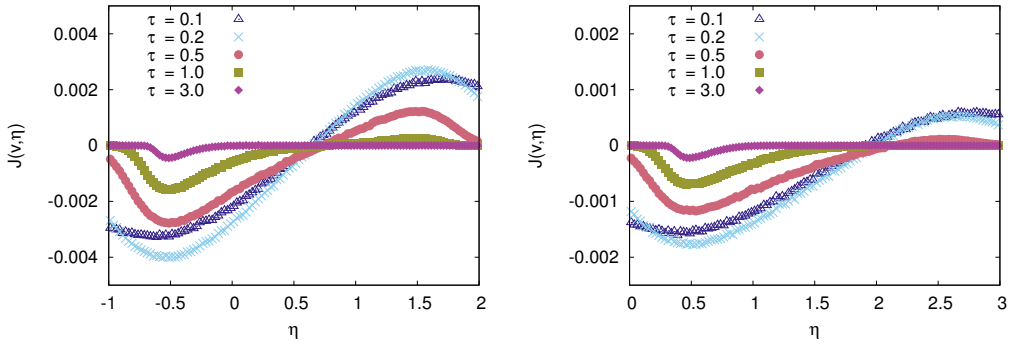

(a) $b = -0.5$ (b) $b = -1.5$

Figure 4.18: η component of the stationary probability current at $v = 0$ for different values of the noise correlation time τ, for a constant force below ($b = -0.5$ (a)) and above ($b = -1.5$ (b)) the deterministic stick-slip transition. The respective sticking intervals are $\eta \in [-0.5, 1.5]$ (a) and $\eta \in [0.5, 2.5]$ (b).

We observe that the sticking interval is shifted, depending on the value of the constant force b, as already mentioned in Sec. 4.1, see Eq. (4.4). For $b = -0.5$ the sticking interval is $\eta \in [-0.5, 1.5]$ (Fig. 4.18(a)) whereas for $b = -1.5$ we have $\eta \in [0.5, 2.5]$ (Fig. 4.18(b)). By varying the correlation time of the noise τ, a non-monotonic behaviour for the probability current on the sticking manifold can be observed, similarly to the pure dry friction case (see Fig. 3.12). For small τ, the probability current on the sticking manifold is very small. If we then increase the correlation time of the noise up to values around $\tau = 0.2$, the current also becomes larger. By further increasing τ towards $\tau = 3.0$, the probability current decreases and disappears almost completely. Due to the constant force b, the two contributions of the probability current on the sticking manifold, which point away from the midpoint of the respective sticking interval to the positive or negative direction, are not equally large. For example in Fig. 4.18(a) the midpoint is at $\eta = 0.5$ and the absolute value of the contribution of the probability current for values smaller than the midpoint is larger than the part, which lies above the midpoint. As we increase τ, the part above the midpoint vanishes quicker than the other. For $\tau = 3.0$, there is no contribution left in the upper half of the sticking interval, but a small contribution still remains in the lower half. For the case of the sliding regime (Fig. 4.18(b)), the contribution in the upper half of the sticking interval vanishes even earlier. For high correlation times, the probability current on the sticking manifold decreases rapidly outside the sticking interval, as we have already seen for the case of pure dry friction.

4.3 Dynamical behaviour

Having discussed the stationary properties of our model, we now turn towards its dynamical characteristics. First, we focus on the power spectral density. We are interested in the interplay of the correlation time of the noise τ, the viscous friction γ and the constant force b and their impact on the correlations of the velocity. In the case of a Gaussian white noise (Eq. (1.2)) the power spectral density can be expressed in terms of a closed analytic formula via the Laplace transform of the propagator [95]. In this framework, asymptotic expressions for the sticking and the sliding regime could be derived for large parameter values of the dry friction coefficient and the constant force. In Sec. 3.3, where the pure dry friction case with

coloured noise has been discussed, we could observe that the correlation time of the velocity t_{corr} increases around a "critical value" of the correlation time of the noise τ. We will investigate how this result changes due to the impact of viscous friction and a constant bias.

Afterwards, the sticking and sliding time periods or, more precisely, their distributions are studied. The obtained results for the time traces in Sec. 4.1 and the non-monotonic behaviour of the probability of sticking suggest that the sticking time distribution might exhibit a related behaviour depending on the values of the correlation time of the noise τ and the constant force b in the sliding and the sticking regime. Finally, the impact of viscous friction and a constant force on the sliding time intervals is probed.

4.3.1 Power spectral density

As exact analytical results are neither available for the stationary probability distribution nor for the propagator of the Fokker-Planck equation (Eq. (4.36)), we have to rely on numerical simulations to compute the power spectral density of the velocity $S(\omega)$. Similarly as in Sec. 3.3.1, we compute 800 time traces of the length $T = 10^4$ numerically and average over them to estimate the power spectral density. The focus of our analysis lies again on the correlations of the velocity. Fig. 4.19 shows the results for the power spectral densities for different values of the constant bias b and for different values of the correlation time of the noise, whereas we keep the viscous friction fixed ($\gamma = 0.1$). In Fig. 4.19(a), we fix the correlation time of the noise at $\tau = 0.001$, which represents the case of white noise. Results for an intermediate correlated noise ($\tau = 1.0$) are shown in Fig. 4.19(b).

As already observed in [95], the spectral density develops a peak for $b \neq 0$. The larger the constant force, the higher the peak in the spectrum. This can be explained via the stationary autocorrelation function, which is related to the power spectral density via the Wiener-Khinchin theorem [38], see Sec. 2.1 in particular Eqs. (2.8) and (2.10). For $b = 0$, the expectation value of the velocity is zero, but for $b \neq 0$ we have $\langle v \rangle \neq 0$. Therefore, by performing a Fourier transform of the autocorrelation function to obtain the power spectral density, a Dirac δ peak arises at $\omega = 0$. Furthermore, we can observe in Fig. 4.19 that the decay of the spectral density becomes larger with increasing constant force. Therefore, we expect the full

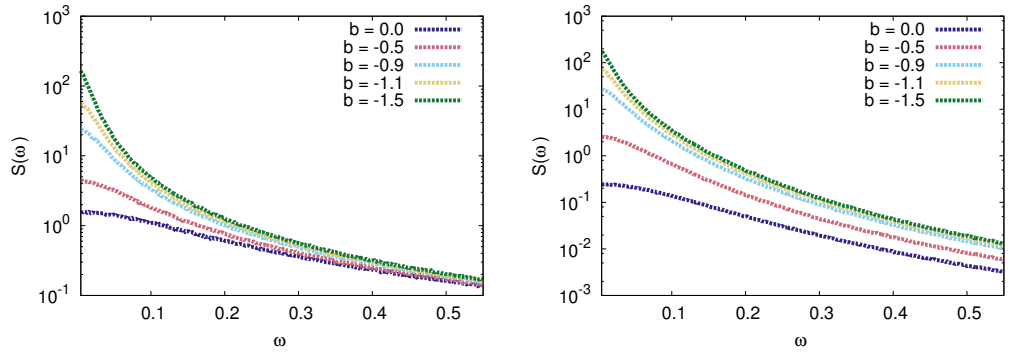

(a) $\tau = 0.001$ (b) $\tau = 1.0$

Figure 4.19: Semi-logarithmic plot of the power spectral density $S(\omega)$, obtained from numerical simulations for different values of the constant bias ($b = 0.0$ (dark blue), $b = -0.5$ (red), $b = -0.9$ (cyan), $b = -1.1$ (yellow), $b = -1.5$ (green)) and two different values of the noise correlation time $\tau = 0.001$ (a) and $\tau = 1.0$ (b). Further parameter $\gamma = 0.1$.

width at half maximum to be smaller the larger the constant force is. In addition to the δ peak, the higher the constant force, the larger the values the spectral density attains. This can be related to the stationary variance of the velocity, which is proportional to the total spectral weight $\Delta v^2 \sim \int_{-\infty}^{\infty} S(\omega) d\omega$. The variance of the velocity Δv^2 decreases for $b = 0$ and increasing correlation time τ (see the dark blue curve in Fig. 4.19(a)). For $b \neq 0$ and especially $|b| > 1$ the variance also decreases but not that strongly as the spectral density for $b = -1.5$ in Fig. 4.19(b) (green curve) is still quite large.

As already seen in Sec. 3.3.1 for the pure dry friction model subjected to coloured noise, the power spectral density changes its shape from a Lorentzian with ω^{-2} decay at large frequencies to a quartic spectral shape with a ω^{-4} decay if we increase the correlation time of the noise (see Fig. 3.13). In Fig. 4.20, we can observe the same transition in the spectral density for the model with viscous friction and constant bias if we increase the correlation time of the noise.

By using the quartic spectral fit function (see caption of Fig. 4.20), we compute the correlation time of the velocity, which we define again as $t_{corr} = \frac{1}{\Delta\omega}$, compare Sec. 3.3.1 and Eq. (2.11). First, we investigate only the impact of viscous friction ($b = 0$) on the correlations of the velocity. Thus, we compute the correlation time of the velocity from the power spectral density for four different values of the viscous

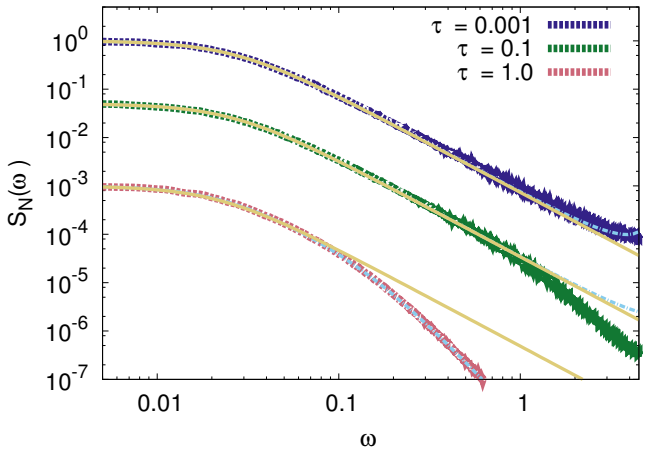

Figure 4.20: Double-logarithmic plot of the power spectral density of the velocity, obtained from numerical simulations (dashed lines). The Spectra have been normalised by cutting out the δ peak at $\omega = 0$ and by the condition $S_N(\omega_{min}) = 1$ (with $\omega_{min} \neq 0$) and shifted respectively for a better visualization. Numerical simulations (dashed lines, $\tau = 0.001$ (dark blue), $\tau = 0.1$ (green), $\tau = 1.0$ (red)), the Lorentzian fit $\sim 1/(1+\omega^2)$ (yellow solid line) and a quartic spectral fit function $\sim 1/(1 + a\omega^2 + b\omega^4)$ (cyan dot-dashed line). Further parameters $b = -1.1$ and $\gamma = 0.1$.

friction coefficient: no viscous friction $\gamma = 0.0$, low friction $\gamma = 0.1$, intermediate friction $\tau = 1.0$ and high friction $\gamma = 10.0$. The results of this analysis are shown in Fig. 4.21. We can see that the correlation time of the velocity t_{corr} decreases if the viscous friction increases. This is in accordance with the case of the Ornstein-Uhlenbeck process (Eq. (2.8)), where the correlation time is proportional to the inverse of the viscous friction coefficient. This observation seems to hold for any value of the correlation time of the noise τ shown in Fig. 4.21. If we increase now the correlation time τ the correlation time of the velocity increases as well. While the increase takes place around the already mentioned "critical value" of $\tau = 0.1$ for intermediate, low and no viscous friction, t_{corr} increases already for very small values of τ in the case of high viscous friction $\gamma = 10.0$. We also observe that for high values of the noise correlation time τ, the distances between the results for t_{corr} for the different values of the viscous friction become smaller compared to the white noise case: for $\tau = 0.001$, we have $t_{corr} = 4$ for $\gamma = 0.0$ and $t_{corr} = 0.18$ for $\gamma = 10.0$, whereas for $\tau = 3.0$ we obtain $t_{corr} = 7.52$ for $\gamma = 0.0$ and $t_{corr} = 2.95$ for

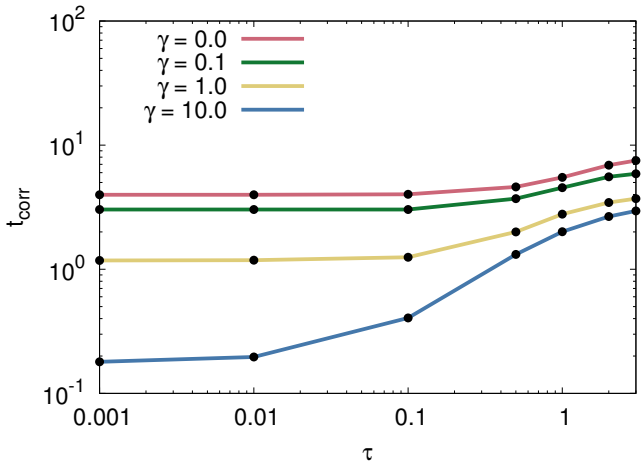

Figure 4.21: Correlation time of the velocity t_{corr} as a function of the correlation time of the noise τ for different values of the viscous friction γ. The results have been obtained from numerical simulations of the power spectral density and the estimation of the full width at half maximum by using a quartic spectral fit, see the caption of Fig. 4.20.

$\gamma = 10.0$. This is in accordance with the result of the Ornstein-Uhlenbeck process, as the full widths at half maximum coincide for high correlation times τ are more or less independent of the value of γ, see Fig. 2.3.

After discussing the impact of the viscous friction in addition to the dry friction, we now take the constant force b into account. In Fig. 4.22 results for the correlation time of the velocity t_{corr} are shown for different values of the constant force. The numerically obtained findings are shown for three different values of the viscous friction: $\gamma = 0.1$ in Fig. 4.22(a), $\gamma = 1.0$ in Fig. 4.22(b) and $\gamma = 10.0$ in Fig. 4.22(c). In the regime of small and intermediate value of the noise correlation time τ, we observe that for low viscous friction, the value of the constant force plays an important role for the correlations of the velocity. For a fixed value τ in the aforementioned regime, the correlation time t_{corr} becomes larger by increasing the constant force, see (Fig. 4.22(a)). This has already been indicated in Fig. 4.19(a), where the power spectral density for $b = -1.5$ decays strongly for intermediate frequencies, resulting in a small full width at half maximum. A similar but lesser impact of the constant force can be seen for intermediate values of the viscous friction $\gamma = 1.0$ (Fig. 4.22(b)). And for high values of γ, the constant force b hardly matters for the result of the correlation time t_{corr}, as the dynamics is strongly dominated by the viscous friction

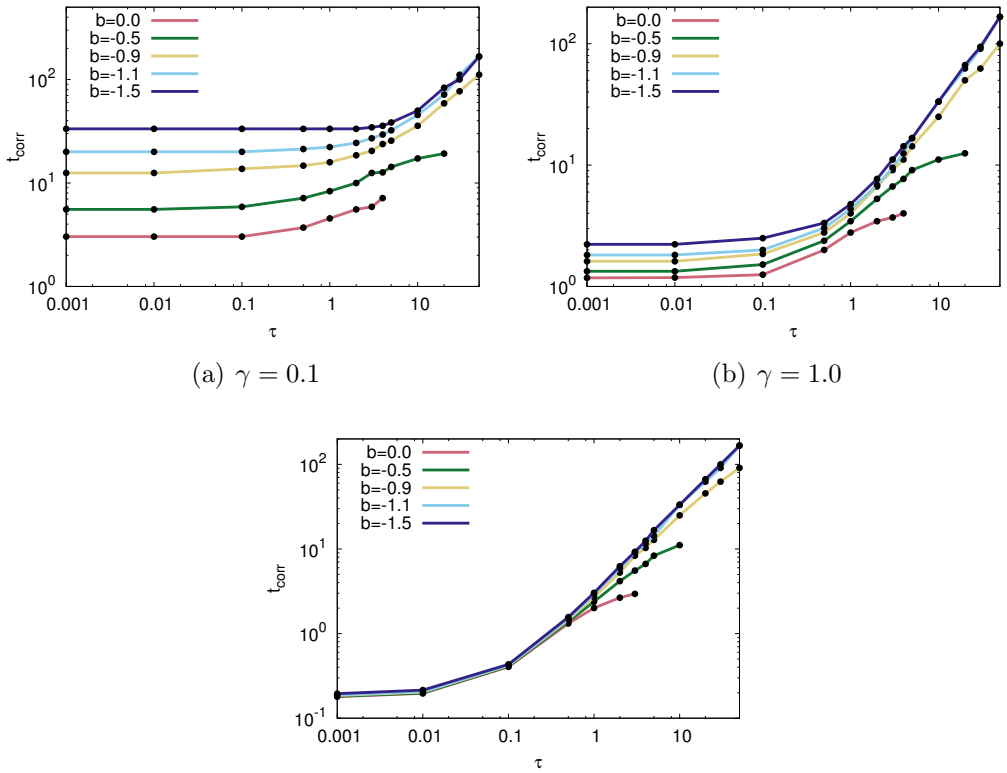

(a) $\gamma = 0.1$

(b) $\gamma = 1.0$

(c) $\gamma = 10.0$

Figure 4.22: Correlation time of the velocity t_{corr} as a function of the correlation time of the noise τ for different values of the constant force $b = 0.0$ (red), $b = -0.5$ (green), $b = -0.9$ (yellow), $b = -1.1$ (cyan), $b = -1.5$ (dark blue) (from top to bottom in each subfigure) and for different parameters of the viscous friction: $\gamma = 0.1$ (a), $\gamma = 1.0$ (b) and $\gamma = 10.0$ (c). The results have been obtained from numerical simulations of the spectral density and the estimation of the full width at half maximum by using a quartic spectral fit, see the caption of Fig. 4.20.

and we therefore have very similar dynamics like an Ornstein-Uhlenbeck process, see Fig. 4.22(c).

Furthermore, in the regime of high noise correlations, the differences between the results for the correlation times of the velocity t_{corr} for different values of the constant force b becomes smaller. This is displayed in Fig. 4.22 only for values of b close to the stick-slip transition ($|b| = 1$) or above as the results for the power spectral density and therefore the correlation time of the velocity are a dynamical feature of this model. For a value of the constant force which lies in the sticking regime,

it becomes more and more difficult to obtain reliable data for the power spectral density for high correlation times as the dynamics are dominated by sticking events in this case. Thus, from Fig. 4.22 stick-slip transitions are not clearly visible.

4.3.2 Sticking and sliding time distributions

In the last part of this chapter, the distribution of the sticking and the sliding time events are investigated. In the previous chapter, the distribution of sticking time events was estimated via the exit time problem for the Ornstein-Uhlenbeck process with two absorbing boundaries (see Sec. 3.3.2). As we considered the pure dry friction case ($\gamma = 0,\ b = 0$), the boundary conditions for this exit time problem were symmetric around $\eta(t) = 0$, i.e. the boundaries were located at $\eta = -1$ and $\eta = 1$, which describes to situation that the particle sticks if $v = 0$ and $-1 < \eta < 1$. It starts moving again if η attains values outside from the aforementioned symmetric interval $[-1, 1]$, as the stochastic force is then strong enough to overcome the dry friction coefficient, which has the value one here. As a constant force enters our equation of motion, the particle sticks now if we have $v = 0$ and $-1 < b + \eta < 1$, as already mentioned in Sec. 4.1, see Eq. (4.1) and therefore the sticking interval changes to the expression shown in Eq. (4.4). Thus, we will consider here the interval $[-1 - b, 1 - b]$ with an initial value $\eta_0 \in (-1 - b, 1 - b)$ for our exit time problem.

As done in Sec. 3.3.2 (see Fig. 3.15) we compute numerically the distribution of initial values $P(\eta_0)$, i.e. when $v(t) = 0$ and $\eta(t)$ attains a value within the interval $[-1 - b, 1 - b]$. We show results for two different values of the constant force b while we vary the correlation time of the noise τ. In Fig. 4.23(a) we have $b = -0.5$ and in Fig. 4.23(b) we use $b = -1.5$.

For small values of τ, $P(\eta_0)$ is uniformly distributed. By increasing τ, the distribution becomes bimodal and the maxima move towards the boundaries of the interval. Due to the constant force, the maxima of the distribution do not stay the same. The maximum, which moves towards the lower bound becomes much larger than the one moving towards the upper boundary. The larger the constant force b, the more pronounced is this phenomenon.

It is possible to derive an exact result for the exit time distribution in Laplace space for two absorbing boundaries α_L (lower boundary) and α_R (upper boundary) ($-\alpha_L \neq \alpha_R$) (see Eq. (D.23)). Unfortunately, the numerical inverse Laplace trans-

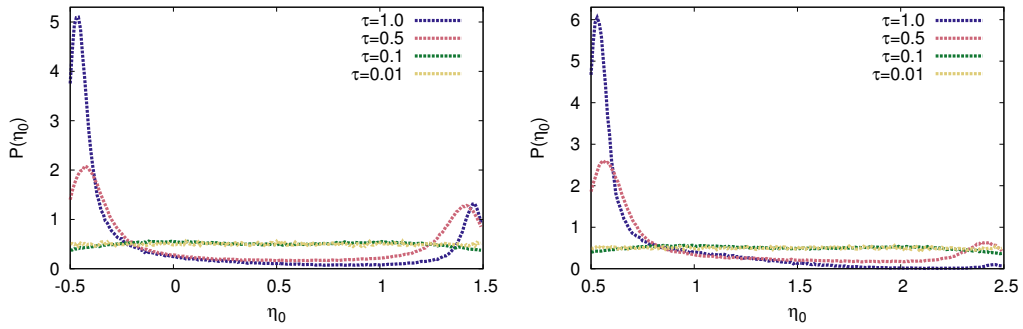

(a) $b = -0.5$ (b) $b = -1.5$

Figure 4.23: Distribution of initial values $P(\eta_0)$ obtained for different values of the correlation time of the noise τ and for the sticking regime ($b = -0.5$ (a)) and the sliding regime ($b = -1.5$ (b)). The results have been obtained numerically from Eqs. (4.1) and (4.3).

form does not give reasonable results for the case including a constant force b. For small values of b and intermediate values of τ results can be obtained but they differ only slightly from the results for the pure dry friction case. For higher parameter values oscillations appear for small sticking times T. In addition, the algorithm produces even negative values. Therefore, we restrict our discussion to the results of numerical simulations.

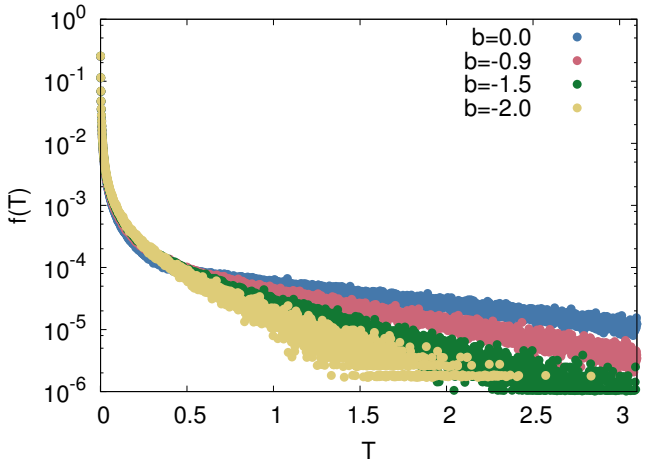

Figure 4.24: Sticking time distribution for $\tau = 1.0$ and different values of the constant force b, obtained numerically from Eqs. (4.1) and (4.3).

Figure 4.24 shows results for the sticking time distribution for a fixed value of the correlation time $\tau = 1.0$ and different values of the constant force b, above and below the stick-slip transition ($|b| = 1$). The shape of the distribution is in general the same as in the pure dry friction case (compare as well to Fig. 3.16): the distributions exhibit a peak around $T = 0$ and then they decay exponentially. For high values of the constant force b, the decay is stronger and therefore it is less likely that the particle sticks for a long time, whereas for smaller values of b, the decay is slower and the particle can stick for longer time periods.

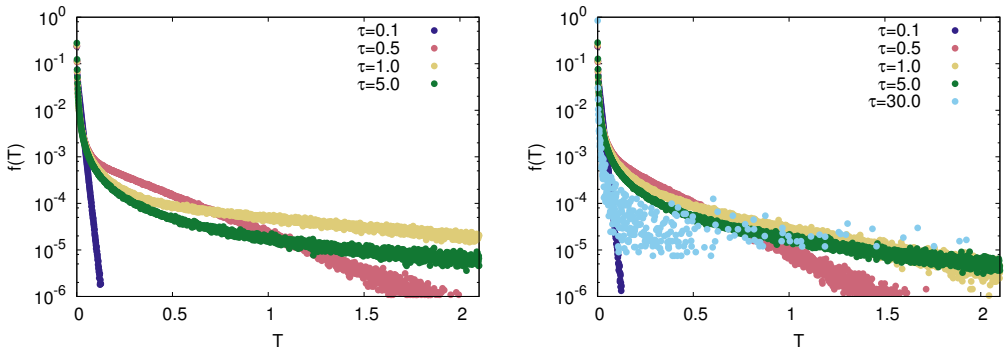

(a) $b = -0.5$ (b) $b = -1.5$

Figure 4.25: Sticking time distribution for $b = -0.5$ (a) and $b = -1.5$ (b) and different values of the correlation of the noise τ, obtained numerically from Eqs. (4.1) and (4.3).

In Fig. 4.25(a) we fix the constant force at a value below the stick-slip transition $b = -0.5$ and increase the correlation time of the noise τ. For small values of τ, the decay of the distribution is very strong; thus, it is not very likely for the particle to stick. By increasing τ further, we observe that the exponential decay for small sticking times becomes weaker. Therefore with higher correlation times τ it becomes more likely for the particle to stick for longer times. We will not show results for very high correlation times here, as the data files for the obtained distributions become very large due to the number of possible sticking time periods and very long numerical simulations are required to average out the fluctuations in the results.

For a constant force in the sliding regime $b = -1.5$, a similar behaviour as previously described can be observed first: by increasing τ, the exponential decay of the distribution becomes weaker. However, for high correlation times τ, we can see that the decay becomes stronger again and only short sticking times are likely

to happen (see the case $\tau = 30$ in Fig. 4.25(b)). This is in accordance with the results from the previous sections, where we observed the appearance and vanishing of sticking time periods (Sec. 4.1) and a non-monotonic behaviour of the probability of sticking (Sec. 4.2.1) by increasing the correlation time. Thus, we conclude that for small and intermediate correlation times τ, the differences between the results for the sticking regime ($b = -0.5$) and the sliding regime ($b = -1.5$) are hardly noticeable. A comparison for high correlation times by performing a purely numerical analysis, where differences between the sticking and sliding regime should be visible, is not an easy task and requires a lot of effort concerning the length of numerical simulations and storage capacities of the computer.

After exploring the sticking time distributions and discussing the influence of the constant force b, we analyse now the sliding time distributions. We have not been able to find analytically solvable model, which can be used to find an analytical expression for the distribution of the sliding time periods, in contrast to the exit time problem for the Ornstein-Uhlenbeck process for the sticking time periods. Therefore our entire analysis will be purely numerically. We proceed similarly to the previous chapter (see Sec. 3.3.2): from the numerically generated time traces of our model (Eqs. (4.1) and (4.3)), we compute the length of the time intervals, for which the velocity v is nonzero. From the length of these time intervals we generate then the distribution for the sliding time periods.

In Sec. 3.3.2, we have seen for the pure dry friction case that for intermediate or larger values of the correlation time of the noise τ the corresponding sliding time distributions exhibits a kind of universal behaviour, see Fig. 3.18. For small sliding times the distribution shows a power law decay (regime (I)), then there is a transition to sliding times with strong exponential decay for a short interval (regime (II), followed an exponential decay as well for intermediate until large sliding times T but the decay is weaker (regime (III). Depending on the value of τ, the transitions between these regimes of different decay behaviour are shifted, i.e. they take place at higher or smaller values of T. For small correlation times, there is only a short regime with a power law decay, whereas for higher correlation times the transition to an exponential decay takes place at higher values of T. These findings can be observed in Fig. 3.17. Here we want to investigate how an additional viscous friction term and different values of the constant force b affect the shape and the behaviour of the sliding time distribution while we increase the correlation time of the noise. In

Fig. 4.26, sliding time distributions are shown for different values of the viscous friction coefficient γ and different values of τ respectively.

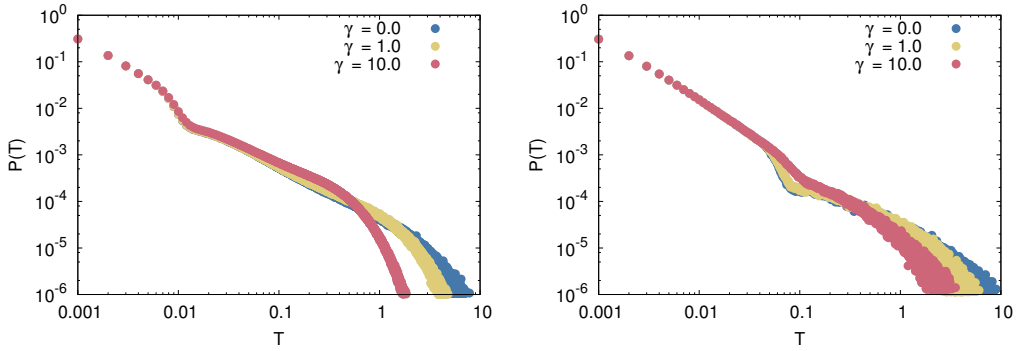

(a) $\tau = 0.1$ (b) $\tau = 2.0$

Figure 4.26: Sliding time distribution $P(T)$, numerically obtained from time traces of our model (Eqs. (4.1) and (4.3)) for different values of the viscous friction γ. Further paramter $\tau = 0.1$ (a), $\tau = 2.0$ (b) and $b = 0$ in both figures.

For small sliding times, the distributions exhibit a power law decay, which is the same for all shown distributions, independent of their value of the viscous friction γ. They show the same behaviour for the strong exponential decay at intermediate times. Only for large sliding times T, we observe a difference regarding the value of the viscous friction: the higher the viscous friction, the stronger the exponential decay of the distribution. Thus, for a small values of γ, it is more likely to observe the particle sliding for a long time. This does not come as a surprise, as for lower viscous friction the particle can attain higher values of the velocity compared to the case of a strong viscous friction. Similarly to the pure dry friction case, the transition from the power law decay to the strong exponential decay takes place already at small sliding times T for $\tau = 0.1$, whereas this transition is shifted towards larger sliding times for a higher noise correlation time. For $\tau = 2.0$ (Fig. 4.26(b)) we also observe that strong viscous damping weakens the strong exponential decay around sliding times of the value $T = 0.1$.

After analysing the impact of the viscous friction on the sliding time periods, we consider now the impact of the constant force in our model and compute the corresponding sliding time distributions. Fig. 4.27 displays results for a fixed viscous friction coefficient $\gamma = 1.0$ and different values of the constant bias: no bias $b = 0$, one below $b = -0.5$ and one above $b = -1.5$ the deterministic stick-slip transition.

For small and intermediate sliding times T, no difference can be observed for the

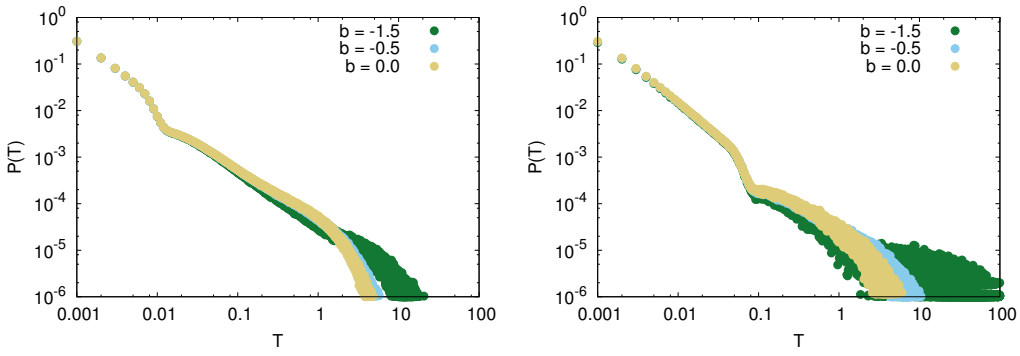

(a) $\tau = 0.1$ (b) $\tau = 2.0$

Figure 4.27: Sliding time distribution $P(T)$, numerically obtained from time traces of our model (Eqs. (4.1) and (4.3)) for different values of the constant force b. Further paramters $\tau = 0.1$ (a), $\tau = 2.0$ (b) and $\gamma = 1.0$ in both figures.

different values of the constant force. The results are only distinguishable in the regime between the weak exponential decay and the exponential cut-off for large sliding times. For a large force (sliding regime), longer sliding times are more likely to be observed compared to the case of the smaller force (sticking regime) and to the case of no bias. While the differences between the different cases are small for $\tau = 0.1$, they seem to become larger at $\tau = 2.0$. However, the results for the cases of $b = 0$ and $b = -0.5$ show more or less the same result. Note that in general only qualitative statements are possible here in this analysis, as the results for the sliding times is purely numerical. Numerical simulations for high correlation times of the noise τ and for constant forces in the sliding regime require a very long time to obtain a reasonable result, where all fluctuations are averaged out.

4.4 Summary of the chapter

In this chapter, we investigated the impact of coloured noise on a dry friction model with viscous friction and constant force. Analytical results have been available in the framework of the unified coloured noise approximation. An analytical expression for the marginal probability density of the velocity has been derived. For increasing correlation time of the noise τ, the stationary distribution shows a Dirac δ peak at

$v = 0$, representing sticking phenomena. Depending on whether the value of the constant force b lies in the sticking or sliding regime, two different types of behaviour of the system could be observed. In the sticking regime, the dynamics shows a transition from sliding dynamics to sticking dynamics for increasing values of τ. The transition to the dynamics dominated by the sticking phenomena occurs at higher correlation times τ compared to the case without the constant force. In the sliding regime, sticking events take place at intermediate values of τ, but if the correlation time of the noise is increased further, the sticking events vanish and only sliding dynamics can be observed. These observations are indicated by a non-monotonic behaviour of the probability of sticking for values of the constant force b in the sliding regime. Furthermore, we have been able to find an asymptotic expression for the joint stationary probability distribution $P(v, \eta)$, which gives a useful description of the dynamics at large velocities and large noise amplitudes. This formal solution does not obey the required matching conditions at the discontinuity at $v = 0$. Due to the lack of detailed balance, it has not been possible to find an exact result for the Fokker-Planck equation of the two-dimensional system with the required matching conditions for the probability distribution and the probability current at the discontinuity,

To study the dynamical properties of our model, i.e. the correlations of the velocity, we computed the power spectral density and compared results for different values of the viscous friction and the constant force. In general, we could again observe that the shape of the spectral densities changes when the correlation time of the noise τ was increased. In the white noise case, the power spectral density is a Lorentzian with a ω^{-2} decay for high frequencies, whereas a ω^{-4} decay is observed for intermediate correlation times of the noise τ. By increasing the viscous friction coefficient γ, the correlation time of the velocity decreases; this inverse proportionality has already been observed for the Ornstein-Uhlenbeck driven by coloured noise. On the other hand, for high values of the constant force b, the correlations of the velocity increase.

Finally, the sticking time and sliding distributions were investigated. In Sec. 3.3.2, the sticking time distribution could be estimated via the exit time problem of an Ornstein-Uhlenbeck process. Here, we could also state an exact result for the exit time distribution in Laplace space. However, as the numerical inversion of this expression does not give reasonable results, we have to rely on a purely numerical

analysis. We focussed our investigations on the sticking ($|b| < 1$) and the sliding ($|b| > 1$) regime. While longer sticking time periods become more likely in the sticking regime as we increase the correlation time of the noise τ, this is observed for the sliding time only for small and intermediate values of τ. For higher values, the sticking time periods are more likely to become shorter, which is in accordance with the previous findings for the probability of sticking. For the estimation of the sliding time distributions suitable analytical models have not been available. Thus, this analysis has also been done purely numerically. We investigated the impact of the viscous friction and the constant force and compared it to the results obtained from the pure dry friction case. The shape of the distributions did not change at small and intermediate sliding times for different values of the viscous friction and the constant force. It is only for large sliding times that differences become visible as the decay is stronger for large viscous friction. For a larger constant force, longer sliding times are possible compared with the case of a smaller constant force. However, in general, it is quite surprising that the shape of the distribution is only marginally affected by the viscous friction and the constant force.

Chapter 5

Eigenvalue problem of a dry friction model with displacement and velocity

In this chapter we consider a two-dimensional stochastic dry friction model with displacement x and velocity v. In the previous Chapters 3 and 4 we investigated the velocity of a particle in stochastic dry friction model subjected to exponentially correlated Ornstein-Uhlenbeck noise. This type of noise led from a one-dimensional non-Markov process for the velocity to a two-dimensional Markov process for velocity and noise amplitude. Instead of using a correlated noise, we add here a spatial component to our dynamical equation and use Gaussian white noise as the stochastic perturbation. This system is another simple version of a two-dimensional piecewise-smooth stochastic system which does not obey detailed balance.

While one-dimensional piecewise-smooth stochastic systems, which consider the velocity component of a particle, have been studied intensely in the past decade, investigations on the displacement of such systems are only in their infancy. Some experiments and numerical studies have been performed to investigate the impact of dry friction on the displacement of water droplets and small solid objects on vibrating substrates [42, 43, 73]. In [72], the Fokker-Planck equation of a dry friction model has been analysed by a direct numerical integration and by demonstrating a formal connection to the Schrödinger equation for the quantum harmonic oscillator, which allowed a semi-analytical treatment of the spatial displacement statistics.

Furthermore, displacement distributions have been calculated in the framework of large deviation properties of functionals with dry friction [20].

Our investigations here will focus on the underlying eigenvalue problem of the dry friction model with displacement and velocity; thus, we will proceed similarly as in [94] for the problem with the velocity only. The main goal of these investigations is to find out how the dry friction affects the dynamics of the displacement. By studying the eigenvalue spectrum of the Fokker-Planck operator we will be able to draw conclusions about quantities like correlation function or other observables like moments or the diffusion constant. The latter can be computed via the autocorrelation function (Green-Kubo relations [46, 61]). These quantities can be related to the eigenvalues of the Fokker-Planck operator, since the time-dependent solution of the Fokker-Planck equation is used for their computation.

The outline of this chapter is the following: we briefly present our stochastic model in Sec. 5.1, before we will derive an eigenvalue equation for our problem in Sec. 5.2, making use of periodic boundary conditions for the position x. In Section 5.3, we focus on the eigenvalue analysis of the system without constant force, before we discuss the eigenvalue problem including a constant force in Sec 5.4. A summary of the chapter is given in Sec. 5.5.

5.1 Two-dimensional piecewise-smooth stochastic system with Gaussian white noise

We add a spatial component to the one-dimensional piecewise-smooth stochastic system for the velocity of a particle (Eq. (1.2)) and after rescaling our variables, our equations of motion for the position x and velocity v are

$$\dot{x}(t) = v(t), \tag{5.1a}$$

$$\dot{v}(t) = -v(t) - \mu\sigma(v(t)) + b + \xi(t). \tag{5.1b}$$

Here, μ denotes the rescaled dry friction coefficient, b is the constant force in non-dimensional units (see App. B.8 for details of the rescaling), and $\xi(t)$ is delta-correlated Gaussian white noise (see Eq. (1.3)). As already mentioned in the introduction (see Sec. 1.1), we have set the mass of the particle to one. Note that

we have used the same rescaling of the variables as for the one-dimensional problem for the velocity only, which facilitates to draw connections between that known problem and the investigated two-dimensional system here. From Eqs. (5.1a) and (5.1b) we observe that the velocity attains only finite values due to the viscous friction, whereas the dynamics in x is unbounded due to the absence of a potential depending on x, thus, the particle can move freely. Therefore, we will impose specific boundaries for the displacement in such a way that the Eqs. (5.1a) and (5.1b) have a well defined joint stationary distribution and the problem becomes treatable by analytical means.

The corresponding Fokker-Planck equation for the joint probability distribution $P(x, v, t|x_0, v_0, 0)$ reads

$$\frac{\partial}{\partial t}P(x, v, t|x_0, v_0, 0) = \left[-\frac{\partial}{\partial x}v + \frac{\partial}{\partial v}\left(v + \mu\sigma(v) - b\right) + \frac{\partial^2}{\partial v^2}\right] P(x, v, t|x_0, v_0, 0) \tag{5.2}$$

with the initial condition

$$P(x, v, 0|x_0, v_0, 0) = \delta(x - x_0)\delta(v - v_0). \tag{5.3}$$

Since the potential conditions are not fulfilled

$$\frac{\partial A_x}{\partial v} \neq \frac{\partial A_v}{\partial x} \tag{5.4}$$

($A_x = v$ and $A_v = -v - \mu\sigma(v) + b$ denote the components of the drift in Eq. (5.2)), the probability current does not vanish everywhere and the computation of the joint stationary probability distribution cannot be done straightforwardly [82]. We impose natural boundary conditions in v and periodic boundary conditions in x, which means the dynamics of x takes place in an interval $x \in [0, L]$ and we have $x = x + L$. These boundaries give rise to a joint stationary probability distribution $P(x, v)$ and enable us to perform analytical calculations.

5.2 Derivation of the eigenvalue equation for periodic boundaries

To find an analytical expression for the propagator in Eq. (5.2), we have to investigate the corresponding eigenvalue problem. Similarly to Sec. 2.3, we use the following ansatz

$$P(x,v,t) = \exp(-\Lambda t) u_\Lambda(x,v), \tag{5.5}$$

where Λ denotes the eigenvalue and $u_\Lambda(x,v)$ the corresponding eigenfunction of the Fokker-Planck operator L_{FP}. The eigenvalue problem reads then

$$\begin{aligned} -\Lambda u_\Lambda(x,v) &= L_{FP} u_\Lambda(x,v) \\ &= \left[-\frac{\partial}{\partial x} v + \frac{\partial}{\partial v}(v + \mu\sigma(v) - b) + \frac{\partial^2}{\partial v^2} \right] u_\Lambda(x,v). \end{aligned} \tag{5.6}$$

As the Fokker-Planck operator in Eq. (5.6) is not Hermitian, we need to consider the adjoint problem as well

$$\begin{aligned} -\Lambda w_\Lambda(x,v) &= L_{FP}^\dagger w_\Lambda(x,v) \\ &= \left[v\frac{\partial}{\partial x} - (v + \mu\sigma(v) - b)\frac{\partial}{\partial v} + \frac{\partial^2}{\partial v^2} \right] w_\Lambda(x,v). \end{aligned} \tag{5.7}$$

A relation like Eq. (2.52) between the two eigenfunctions $u_\Lambda(x,v)$ and $w_\Lambda(x,v)$ can only be formulated if detailed balance holds [38]. The full expression for the propagator reads (similarly to Eq. (2.56) and assuming a discrete eigenvalue spectrum, see Sec. 2.3)

$$P(x,v,t|x_0,v_0,0) = \sum_\Lambda \exp(-\Lambda t) \frac{u_\Lambda(x,v) w_\Lambda(x_0,v_0)}{M_\Lambda}, \tag{5.8}$$

where M_Λ is the normalisation constant

$$M_\Lambda = \int_0^L \int_{-\infty}^{\infty} u_\Lambda(x,v) w_\Lambda(x,v) dv dx. \tag{5.9}$$

As previously indicated, both eigenfunctions satisfy periodic boundary conditions in x, e.g. $u_\Lambda(x+L,v) = u_\Lambda(x,v)$, and for the velocity we have, similarly to Eq. (2.55)

$$u_\Lambda(x,v)w_\Lambda(x,v) \xrightarrow{|v|\to\infty} 0, \tag{5.10}$$

which follows from the duality of the operators L_{FP} and $L_{FP}^\dagger$ (Eqs. (5.6) and (5.7)).

Here, we proceed with the analysis of the eigenvalues by focussing only on the eigenfunctions $u_\Lambda(x,v)$ and in the following parts we will drop the index Λ. The solutions of the eigenvalue equations need to satisfy the matching conditions at the discontinuity (compare Eqs. (2.58a) and (2.58b)), i.e. the eigenfunctions $u(x,v)$ and the v-component of the probability current have to be continuous at $v = 0$; thus, we have

$$u(x,0-) = u(x,0+), \tag{5.11a}$$

$$-(\mu+b)\,u(x,0-) + \frac{\partial}{\partial v}u(x,v)\bigg|_{v=0-} = (\mu-b)\,u(x,0+) + \frac{\partial}{\partial v}u(x,v)\bigg|_{v=0+}. \tag{5.11b}$$

Due to the periodic boundaries in x, we can expand $u(x,v)$ in a Fourier series in x by using the following separation ansatz

$$u(x,v) = e^{i\beta x}\phi(v). \tag{5.12}$$

An expression for β can be found via

$$e^{i\beta x} = e^{i\beta(x+L)} \quad \to e^{i\beta L} = 1, \tag{5.13}$$

and therefore we have

$$\beta_m = \frac{2\pi m}{L}, \tag{5.14}$$

with $m \in \mathbb{Z}$. Thus, we can express the eigenfunction $u(x,v)$ by the sum of all Fourier modes

$$u(x,v) = \sum_{m\in\mathbb{Z}} e^{i\beta_m x}\phi_m(v). \tag{5.15}$$

Inserting this ansatz in Eq. (5.6) gives us an eigenvalue equation for $\phi_m(v)$

$$-\Lambda_m\phi_m(v) = -\left[i\beta_m v + \frac{\partial}{\partial v}\left(v + \mu\sigma(v) - b\right) + \frac{\partial^2}{\partial v^2}\right]\phi_m(v). \tag{5.16}$$

Next, we apply the transformation

$$\phi_m(v) = e^{i\beta_m v}\psi_m(v). \tag{5.17}$$

Thus, the terms with the derivatives with respect to v change

$$\frac{\partial^2}{\partial v^2}\phi_m(v) = e^{i\beta_m v}\left[(i\beta_m)^2\psi_m(v) + 2i\beta_m\frac{\partial}{\partial v}\psi_m(v) + \frac{\partial^2}{\partial v^2}\psi_m(v)\right] \tag{5.18}$$

and

$$\begin{aligned}\frac{\partial}{\partial v}\left(v+\mu\sigma(v)-b\right)\phi_m(v) &= e^{i\beta_m v}\Big[i\beta_m\left(v+\mu\sigma(v)-b\right)\psi_m(v) \\ &+ \frac{\partial}{\partial v}\left(v+\mu\sigma(v)-b\right)\psi_m(v)\Big].\end{aligned} \tag{5.19}$$

Therefore, we end up with the following equation for $\psi_m(v)$

$$-\left(\Lambda_m + i\beta_m(\mu\sigma(v)-b) - \beta_m^2\right)\psi_m(v) = \left[\frac{\partial}{\partial v}\left(v+\mu\sigma(v)-b+2i\beta_m\right) + \frac{\partial^2}{\partial v^2}\right]\psi_m(v). \tag{5.20}$$

Equation (5.20) has the same structure as the one for the one-dimensional problem with the velocity (see Sec. 2.3 in particular Eqs. (2.62) and (2.73)). It differs only in the additional terms with β_m. Thus, by using the Fourier expansion in x (Eq. (5.15)), we have transformed the original problem (Eq. (5.6)) to a modified version of a known problem, which has been analysed thoroughly. The solution for $\psi_m(v)$ and therefore $\phi_m(v)$ (Eq. (5.17)) have to obey natural boundary conditions at infinity ($v \to \pm\infty$) and the matching conditions at the origin ($v = 0$) (Eqs. (5.11a) and (5.11b))

$$\phi_m(0-) = \phi_m(0+), \tag{5.21a}$$

$$-(\mu+b)\phi_m(0-) + \frac{\partial}{\partial v}\phi_m(v)\bigg|_{v=0-} = (\mu-b)\phi_m(0+) + \frac{\partial}{\partial v}\phi_m(v)\bigg|_{v=0+}. \tag{5.21b}$$

As already mentioned above, the product of the eigenfunctions has to obey natural boundary conditions (Eq. (5.10)). Thus, we actually have

$$\phi_m(v)\hat{\phi}_m(v) \xrightarrow{|v|\to\infty} 0, \tag{5.22}$$

where $\hat{\phi}_m(v)$ is connected to the eigenfunction of the adjoint problem $w(x,v)$ (Eq. (5.7)) as $\phi_m(v)$ is to $u(x,v)$, see Eq. (5.12). In the following eigenvalue analysis, we will separately consider the cases without constant force and with additional constant force.

5.3 Eigenvalue analysis without constant bias

In the case of the one-dimensional problem for the velocity, the eigenvalue analysis for the case without constant force has been performed from the perspective of even and odd eigenfunctions (see Sec. 2.3). Even and odd eigenfunctions follow symmetry relations

$$u^{(e)}(x,v) = u^{(e)}(-x,-v), \quad u^{(o)}(x,v) = -u^{(o)}(-x,-v). \tag{5.23}$$

$u^{(e)}(x,v)$ denotes the even eigenfunction and $u^{(o)}(x,v)$ is the odd eigenfunction. Our eigenvalue equation reads without the constant force

$$-(\Lambda_m + i\beta_m\mu\sigma(v) - \beta_m^2)\psi_m(v) = \left(\frac{\partial}{\partial v}(v + \mu\sigma(v) + 2i\beta_m) + \frac{\partial^2}{\partial v^2}\right)\psi_m(v) \tag{5.24}$$

Note that for $m = 0$ we receive the known problem for the velocity only, where the eigenfunction is even or odd. Here for $m \neq 0$ the function $\phi_m(v)$ does not have a designated symmetry. Therefore we need to proceed differently to facilitate the derivation of the characteristic equation by using symmetry relations of the eigenfunctions.

If we rewrite Eq. (5.24) by using $v \to -v$ (and making use of the antisymmetric relation $\sigma(v) = -\sigma(-v)$), we find

$$-(\Lambda_m - i\beta_m\mu\sigma(v) - \beta_m^2)\psi_m(-v) = \left[\frac{\partial}{\partial v}(v + \mu\sigma(v) - 2i\beta_m) + \frac{\partial^2}{\partial v^2}\right]\psi_m(-v). \tag{5.25}$$

We note that Eq. (5.25) is the eigenvalue equation for $-m$. This gives us the relations

$$\Lambda_m = \Lambda_{-m}, \quad \psi_{-m}(v) = \psi_m(-v), \tag{5.26}$$

which means that eigenvalues are degenerated for $m \neq 0$. Thus, the eigenvalue spectrum consists of simple eigenvalues with $m = 0$ and the corresponding eigen-

function $\phi_0(v)$ is even or odd. For $m \neq 0$, to each of the aforementioned eigenvalues there are double degenerated eigenvalues $\Lambda_m = \Lambda_{-m}$ and the corresponding eigenfunctions are the Fourier modes $\exp(i\beta_m x)\,\phi_m(v)$ and their complex conjugates, respectively, which is equal to the Fourier mode with the corresponding negative index $-m$ ($\exp(i\beta_{-m}x)\,\phi_{-m}(v)$). By using a suitable linear combination of these eigenfunctions, we can construct even and odd eigenfunctions via

$$u^{(e)}(x,v) = \frac{1}{2}\left[\exp(i\beta_m(x+v))\,\psi_m(v) + \exp(-i\beta_m(x+v))\,\psi_m(-v)\right] \quad (5.27)$$

$$u^{(o)}(x,v) = \frac{1}{2}\left[\exp(i\beta_m(x+v))\,\psi_m(v) - \exp(-i\beta_m(x+v))\,\psi_m(-v)\right] \quad (5.28)$$

which satisfy the symmetry relations above (Eqs. (5.23)).

Furthermore, we can show that all eigenvalues Λ_m are real. Taking the complex conjugate of Eq. (5.24) gives

$$-(\bar{\Lambda}_m - i\beta_m\mu\sigma(v) - \beta_m^2)\bar{\psi}_m(v) = \left(\frac{\partial}{\partial v}(v + \mu\sigma(v) - 2i\beta_m) + \frac{\partial^2}{\partial v^2}\right)\bar{\psi}_m(v). \quad (5.29)$$

This result coincides with Eq. (5.25), which is the eigenvalue equation for $-m$. Thus, we have the relations

$$\bar{\Lambda}_m = \Lambda_m = \Lambda_{-m}, \quad \bar{\psi}_m(v) = \psi_{-m}(v) = \psi_m(-v). \quad (5.30)$$

Although we used $\psi_m(v)$ in these calculations, these relations hold as well for $\phi_m(v)$ (Eq. (5.17)).

As for the one-dimensional problem for the velocity (see Sec. 2.3), it is sufficient to solve the problem for the positive half space with appropriate boundary conditions at the origin, which are given by Eqs. (5.21a) and (5.21b). Using the relations from Eq. (5.30) the boundary conditions at the origin change to

$$\bar{\phi}_m(0+) = \phi_m(0+), \quad (5.31a)$$

$$-\mu\bar{\phi}_m(0+) - \frac{\partial}{\partial v}\bar{\phi}_m(v)\bigg|_{v=0+} = \mu\phi_m(0+) + \frac{\partial}{\partial v}\phi_m(v)\bigg|_{v=0+}. \quad (5.31b)$$

Therefore, we investigate Eq. (5.20) for $v > 0$

$$-\left(\Lambda_m + i\beta_m\mu - \beta_m^2\right)\psi_m(v) = \frac{\partial}{\partial v}\left(v + \mu + 2i\beta_m\right)\psi_m(v) + \frac{\partial^2}{\partial v^2}\psi_m(v). \tag{5.32}$$

Similarly to Eq. (2.66), Eq. (5.32) can be solved by

$$\psi_m(v) = C\exp(-(v+\mu+2i\beta_m)^2/4)D_{\zeta_m}(v+\mu+2i\beta_m) \tag{5.33}$$

with the parabolic cylinder function $D_{\zeta_m}(v+\mu+2i\beta_m)$ and we have used the abbreviation for the index

$$\zeta_m = \Lambda_m + i\beta_m\mu - \beta_m^2. \tag{5.34}$$

C denotes a complex coefficient of the solution. Equation (5.33) satisfies the boundary condition at infinity due to the asymptotic behaviour of the parabolic cylinder function (see App. C.1). Next, we want to find the characteristic equation for the underlying problem. Therefore, we use the result from Eq. (5.33) and insert the expression for $\phi_m(v)$ (Eq. (5.17)) into Eqs. (5.31a) and (5.31b). From Eq. (5.31a) we obtain

$$\bar{C}\exp(-(\mu-2i\beta_m)^2/4)D_{\bar{\zeta}_m}(\mu-2i\beta_m) = C\exp(-(\mu+2i\beta_m)^2/4)D_{\zeta_m}(\mu+2i\beta_m). \tag{5.35}$$

The contributions on the left-hand side of Eq. (5.31b) give

$$-\mu\bar{\phi}_m(0+) = -\mu\bar{C}\exp(-(\mu-2i\beta_m)^2/4)D_{\bar{\zeta}_m}(\mu-2i\beta_m), \tag{5.36}$$

$$\begin{aligned} -\frac{\partial}{\partial v}\bar{\phi}_m(v)\bigg|_{v=0+} &= i\beta_m\bar{C}\exp(-(\mu-2i\beta_m)^2/4)D_{\bar{\zeta}_m}(\mu-2i\beta_m) \\ &\quad - \frac{\partial}{\partial v}\bar{C}\exp(-(v+\mu-2i\beta_m)^2/4)D_{\bar{\zeta}_m}(v+\mu-2i\beta_m)\bigg|_{v=0+} \\ &= i\beta_m\bar{C}\exp(-(\mu-2i\beta_m)^2/4)D_{\bar{\zeta}_m}(\mu-2i\beta_m) \\ &\quad + \bar{C}\exp(-(\mu-2i\beta_m)^2/4)D_{\bar{\zeta}_m+1}(\mu-2i\beta_m). \end{aligned} \tag{5.37}$$

In the last step of Eq. (5.37), we have used an identity for the parabolic cylinder

functions (Eq. (C.5a)) The contributions on the right-hand side of Eq. (5.31b) yields

$$\begin{aligned}
\mu\phi_m(0+) &= \mu C\exp(-(\mu+2i\beta_m)^2/4)D_{\zeta_m}(\mu+2i\beta_m), && (5.38)\\
\frac{\partial}{\partial v}\phi_m(v)\bigg|_{v=0+} &= i\beta_m C\exp(-(\mu+2i\beta_m)^2/4)D_{\zeta_m}(\mu+2i\beta_m)\\
&\quad + \frac{\partial}{\partial v}C\exp(-(v+\mu+2i\beta_m)^2/4)D_{\zeta_m}(v+\mu+2i\beta_m)\bigg|_{v=0+}\\
&= i\beta_m C\exp(-(\mu+2i\beta_m)^2/4)D_{\zeta_m}(\mu+2i\beta_m)\\
&\quad - C\exp(-(\mu+2i\beta_m)^2/4)D_{\zeta_m+1}(\mu+2i\beta_m). && (5.39)
\end{aligned}$$

Finally, we combine these expression (Eqs. (5.36) - (5.39)) and obtain

$$\begin{aligned}
&\bar{C}\exp(-(\mu-2i\beta_m)^2/4)\left[-(\mu-i\beta_m)D_{\bar{\zeta}_m}(\mu-2i\beta_m)+D_{\bar{\zeta}_m+1}(\mu-2i\beta_m)\right]\\
=\;& C\exp(-(\mu+2i\beta_m)^2/4)\left[(\mu+i\beta_m)D_{\zeta_m}(\mu+2i\beta_m)-D_{\zeta_m+1}(\mu+2i\beta_m)\right]. \qquad (5.40)
\end{aligned}$$

We observe that the factor $C\exp(-(\mu+2i\beta_m)^2/4)$ and its complex conjugate counterpart occur in both equations (Eqs. (5.35) and (5.40)). Therefore, we can combine these equations to obtain

$$\begin{aligned}
&D_{\zeta_m}(\mu+2i\beta_m)\left[-(\mu-i\beta_m)D_{\bar{\zeta}_m}(\mu-2i\beta_m)+D_{\bar{\zeta}_m+1}(\mu-2i\beta_m)\right]\\
&-D_{\bar{\zeta}_m}(\mu-2i\beta_m)\left[(\mu+i\beta_m)D_{\zeta_m}(\mu+2i\beta_m)-D_{\zeta_m+1}(\mu+2i\beta_m)\right]=0 \qquad (5.41)
\end{aligned}$$

and after using an identity for the parabolic cylinder functions (Eq. (C.3)), we arrive at the characteristic equation

$$\begin{aligned}
&D_{\Lambda_{n,m}+i\beta_m\mu-\beta_m^2}(\mu+2i\beta_m)[\Lambda_{n,m}-i\beta_m\mu-\beta_m^2]D_{\Lambda_{n,m}-i\beta_m\mu-\beta_m^2-1}(\mu-2i\beta_m)\\
&+D_{\Lambda_{n,m}-i\beta_m\mu-\beta_m^2}(\mu-2i\beta_m)[\Lambda_{n,m}+i\beta_m\mu-\beta_m^2]D_{\Lambda_{n,m}+i\beta_m\mu-\beta_m^2-1}(\mu+2i\beta_m)=0. \qquad (5.42)
\end{aligned}$$

Here, $\Lambda_{n,m}$ denotes the respective eigenvalue, which has, compared to the one-dimensional problem, an additional second label m due to the contribution of the periodic boundaries in the displacement.

To check the consistency of our result in Eq. (5.42), we consider several special

cases. For $\beta_m = 0$, we arrive at the characteristic equation for the one-dimensional Fokker-Planck equation (compare Eqs. (2.67a) and (2.67b))

$$D_{\Lambda_{n,0}}(\mu)\Lambda_{n,0}D_{\Lambda_{n,0}-1}(\mu) = 0. \tag{5.43}$$

If we set $\mu = 0$ in Eq. (5.42), we obtain

$$\begin{aligned} &D_{\Lambda_{n,m}-\beta_m^2}(2i\beta_m)(\Lambda_{n,m} - \beta_m^2)D_{\Lambda_{n,m}-\beta_m^2-1}(-2i\beta_m) \\ &+D_{\Lambda_{n,m}-\beta_m^2}(-2i\beta_m)(\Lambda_{n,m} - \beta_m^2)D_{\Lambda_{n,m}-\beta_m^2-1}(2i\beta_m) = 0 \end{aligned} \tag{5.44}$$

and by applying the product identity for parabolic cylinder functions (Eqs. (C.6)), we arrive at

$$\frac{\sqrt{2\pi}(\Lambda_{n,m} - \beta_m^2)}{\Gamma(-\Lambda_{n,m} + \beta_m^2 - 1)} = 0. \tag{5.45}$$

From the properties of the gamma function, we therefore obtain the eigenvalues

$$\Lambda_{n,m} = n + \beta_m^2, \tag{5.46}$$

which denotes the spectrum of the Ornstein-Uhlenbeck process with an additional term due to the periodic boundaries of the displacement [82].

Next, we investigate how the dry friction affects the eigenvalues $\Lambda_{n,m}$ by numerically evaluating Eq. (5.42). In the following analysis, we will always refer to positive integers m as indices of the eigenvalues. However, due to the degeneracy of the eigenvalues, results which are valid for an eigenvalue $\Lambda_{n,m}$ apply as well for the eigenvalue $\Lambda_{n,-m}$.

Fig. 5.1 shows the results for the eigenvalues $\Lambda_{1,m}$ with $m = 0, 1, \ldots, 4$. As already known from the one-dimensional problem for the velocity, the eigenvalue $\Lambda_{1,0}$ becomes larger if we increase the dry friction (see Fig. 2.4 as well). The same behaviour can be observed for the other eigenvalues $\Lambda_{1,m}$ with $m \neq 0$. For $\mu = 0$ the eigenvalues can be found from Eq. (5.46). Furthermore, we observe that the eigenvalue $\Lambda_{1,4}$ increases stronger for larger dry friction compared to the other eigenvalues, i.e. the distance to the eigenvalue $\Lambda_{1,3}$ seems to increase. For each value of μ, the eigenvalue $\Lambda_{1,0}$ is the smallest eigenvalue compared to the others with different index m. Due to difficulties with the numerical evaluation of Eq. (5.42) to obtain eigenvalues with large indices m, we only study eigenvalues for the indices

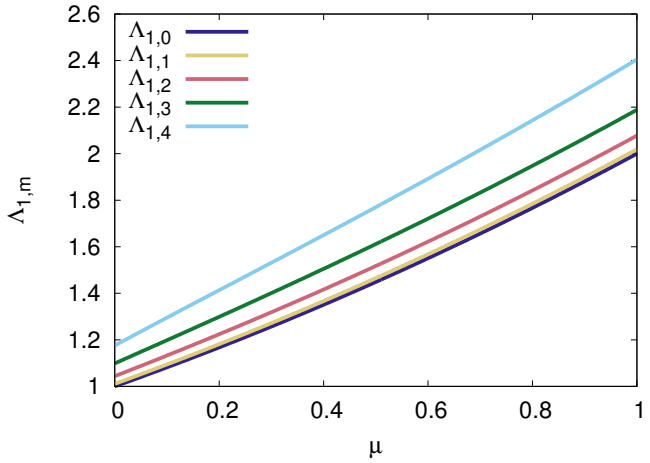

Figure 5.1: Eigenvalues $\Lambda_{1,m}$ with $m = 0, 1, \ldots, 4$ as function of the dry friction. The results have been obtained numerically from Eq. (5.42) with the step size $\Delta\mu = 0.005$. Further parameter: $L = 60$.

$m \leq 4$.

In Fig. 5.2, we can observe that an analysis for the eigenvalues $\Lambda_{2,m}$ with $m = 0, 1, \ldots, 4$ gives similar results as seen in Fig. 5.1. By increasing the dry friction, all eigenvalues increase as well. However, here a additional phenomenon occurs. While we have observed in Fig. 5.1 that eigenvalues with a larger m are larger than those with the smaller value for m, this is only the case for small dry friction in Fig. 5.2. At specific values of the dry friction coefficient μ, the eigenvalues with the larger index m cross the eigenvalues with smaller indices m and by increasing μ further, we see that those eigenvalues with the larger index m are smaller than the ones with a smaller index m. For example for large dry friction, the eigenvalue $\Lambda_{2,m}$ is the largest compared to the other eigenvalues with larger index m. Thus, for large values of the dry friction we observe exactly the opposite order of the eigenvalues $\Lambda_{2,m}$ compared to the eigenvalues $\Lambda_{1,m}$.

As we compute the eigenvalues $\Lambda_{3,m}$ and $\Lambda_{4,m}$ with $m = 0, 1, 2, 3$ (see Fig. 5.3), we find similar results compared to Figs. 5.1 and 5.2. For increasing dry friction, the eigenvalues become larger as well. For the eigenvalues $\Lambda_{3,m}$ we find the same relation as we found for $\Lambda_{1,m}$: eigenvalues with a larger index m are larger than eigenvalues with a smaller index m, i.e. the eigenvalue $\Lambda_{3,0}$ is the smallest. However, for the eigenvalues $\Lambda_{4,m}$ the same behaviour is found as for the eigenvalues $\Lambda_{2,m}$. Only for

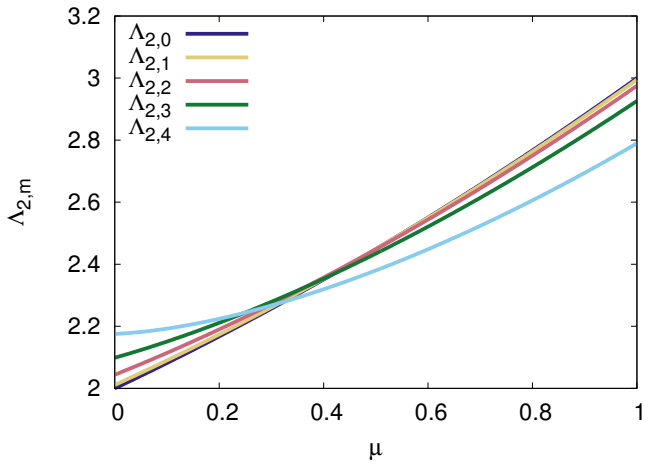

Figure 5.2: Eigenvalues $\Lambda_{2,m}$ with $m = 0, 1, \ldots, 4$ as function of the dry friction. The results have been obtained numerically from Eq. (5.42) with the step size $\Delta\mu = 0.005$. Further parameter: $L = 60$.

small values of the dry friction, $\Lambda_{4,0}$ is the smallest compared to eigenvalues with a larger index m, whereas for large values of μ the eigenvalue $\Lambda_{4,0}$ becomes the largest eigenvalue of the eigenvalues with $n = 4$.

Based on our findings in Figs. 5.1 - 5.3, we assume a general rule of the order among the eigenvalues $\Lambda_{n,m}$ concerning the index m for the same n. For odd integers n, we have always

$$\Lambda_{n,m+1} > \Lambda_{n,m}, \quad \Lambda_{n,-m-1} > \Lambda_{n,-m}. \tag{5.47}$$

For even integers n, the eigenvalues follow a relation as in Eq. (5.47) with the difference being that here, we are looking at small dry friction. For large dry friction we get

$$\Lambda_{n,m+1} < \Lambda_{n,m}, \quad \Lambda_{n,-m-1} < \Lambda_{n,-m}. \tag{5.48}$$

Eq. (5.48) implies that the range of m values is bounded, otherwise $\Lambda_{n,m}$ can become negative. This would lead to the scenario that the propagator (Eq. 5.5) becomes unstable in the stationary limit $t \to \infty$.

Next, we investigate the eigenvalues $\Lambda_{0,m}$. From the one-dimensional problem for the velocity, we know that $\Lambda_{0,0} = 0$ for all μ. Eq. (5.46) gives us the starting point for our analysis as we obtain the eigenvalues $\Lambda_{0,m}$ for $\mu = 0$. Varying the dry friction coefficient in Eq. (5.42), we observe a quite surprising result, which is shown in Fig. 5.4. The eigenvalues $\Lambda_{0,m}$ with $m \neq 0$ decrease towards zero as

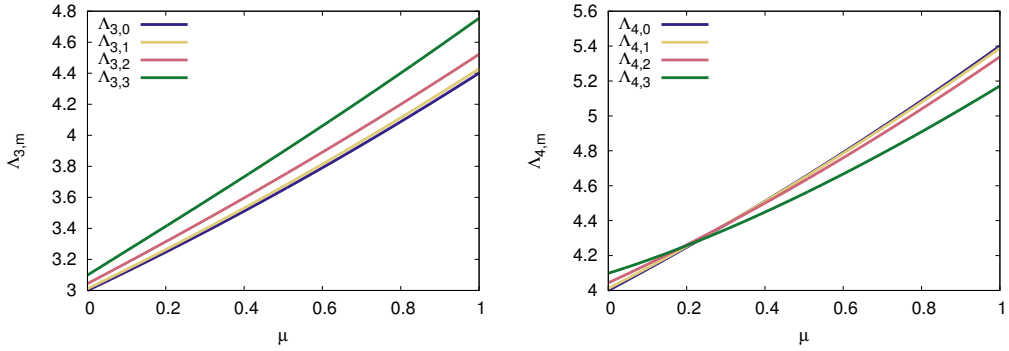

(a) $\Lambda_{3,m}$ (b) $\Lambda_{4,m}$

Figure 5.3: Eigenvalues $\Lambda_{3,m}$ (a) and $\Lambda_{4,m}$ (b) with $m = 0, 1, 2, 3$ as function of the dry friction. The results have been obtained numerically from Eq. (5.42) with the step size $\Delta\mu = 0.005$. Further parameter: $L = 60$.

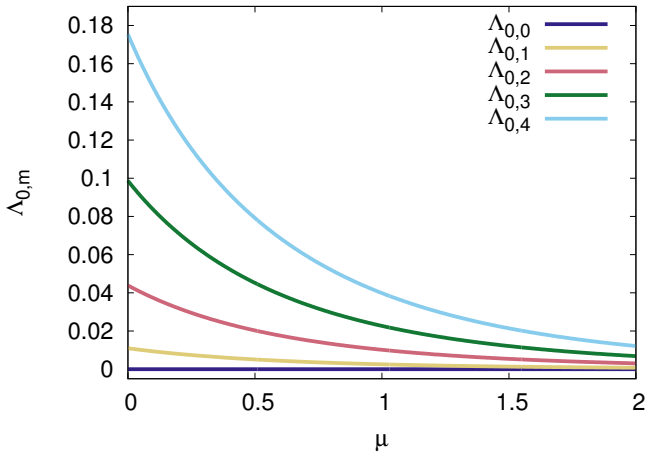

Figure 5.4: Eigenvalues $\Lambda_{0,m}$ with $m = 0, 1, \ldots, 4$ as function of the dry friction. The results have been obtained numerically from Eq. (5.42) with the step size $\Delta\mu = 0.005$. Further parameter: $L = 60$.

we increase the dry friction. This result is exactly the opposite behaviour to the previously observed results for the eigenvalues with $n \geq 1$ (see Figs. 5.1 - 5.3). Here we performed the analysis only for eigenvalues with the index $m \leq 4$ and the dry friction coefficient does not exceed $\mu = 2$.

This astonishing result leads to the question of how exactly this affects the stationary behaviour of the system, as the eigenvalues $\Lambda_{0,m}$ are the smallest in the entire eigenvalue spectrum and determine therefore the long time behaviour of the

system.

5.4 Eigenvalue analysis with constant bias

In this section, we study the eigenvalue problem with an additional constant force b. As in the case for the velocity only, we cannot classify the eigenfunctions into odd and even functions with an additional constant force in the equation of motion, see Sec. 2.3. Therefore we need to proceed with the full equation (Eq. (5.20)) to find an expression for $\psi_m(v)$ (and $\phi_m(v)$), which satisfies natural boundaries conditions at $v \to \pm\infty$. Thus, we have for the two half spaces of the velocity

$$-\left(\Lambda_m + i\beta_m(\pm\mu - b) - \beta_m^2\right)\psi_m(v) = \left[\frac{\partial}{\partial v}\left(v \pm \mu - b - 2i\beta_m\right) + \frac{\partial^2}{\partial v^2}\right]\psi_m(v), \quad v \gtrless 0. \tag{5.49}$$

Considering the complex conjugate equation of Eq. (5.49), we get

$$-\left(\bar{\Lambda}_m - i\beta_m(\pm\mu - b) - \beta_m^2\right)\bar{\psi}_m(v) = \left[\frac{\partial}{\partial v}\left(v \pm \mu - b + 2i\beta_m\right) + \frac{\partial^2}{\partial v^2}\right]\bar{\psi}_m(v), \quad v \gtrless 0. \tag{5.50}$$

We observe that Eq. (5.50) is the eigenvalue equation for negative indices m (see Eq. (5.14) for β_m). Therefore, we obtain here the relations

$$\bar{\Lambda}_m = \Lambda_{-m}, \quad \bar{\psi}_m(v) = \psi_{-m}(v). \tag{5.51}$$

However, if we compare the positive and the negative half space for the velocity in Eq. (5.49), we have $\Lambda_m \neq \Lambda_{-m}$ in contrast to Sec. 5.3 (see Eq. (5.26)). Thus, the additional constant force removes the degeneracy of the eigenvalues (see Eq. (5.26)) and the eigenvalues Λ_m with $m \neq 0$ come as complex conjugate pairs, see Eq. (5.51).

Equation (5.49) can be solved by

$$\psi_m(v) = C_+ \exp(-(v + \mu - b + 2i\beta_m)^2/4) D_{\zeta_m}(v + \mu - b + 2i\beta_m) \tag{5.52}$$

for the positive half space $v > 0$ and by

$$\psi_m(v) = C_- \exp(-(v - \mu - b + 2i\beta_m)^2/4) D_{\theta_m}(-(v - \mu - b + 2i\beta_m)) \tag{5.53}$$

for the negative half space $v < 0$. Here we used the expressions

$$\zeta_m = \Lambda_m + i\beta_m(\mu - b) - \beta_m^2, \tag{5.54a}$$
$$\theta_m = \Lambda_m - i\beta_m(\mu + b) - \beta_m^2, \tag{5.54b}$$

and $C_\pm$ are amplitudes for the solution in the respective half space. The two solutions (Eqs. (5.52) and (5.53)) satisfy the boundary condition at infinity for each half space respectively (see Eq. (2.74) and App. C.1 for details). In addition, we need to check the matching conditions for $\phi_m(v)$ at the origin (Eqs. (5.21a) and (5.21b)). The continuity of the eigenfunction results in

$$\begin{aligned} & C_- \exp(-(\mu + b - 2i\beta_m)^2/4) D_{\theta_m}(\mu + b - 2i\beta_m) \\ = \quad & C_+ \exp(-(\mu - b + 2i\beta_m)^2/4) D_{\zeta_m}(\mu - b + 2i\beta_m). \end{aligned} \tag{5.55}$$

In order to check the continuity of the probability current, the contributions for the positive half-space read

$$(\mu - b)\phi_m(0+) = (\mu - b) C_+ \exp(-(\mu - b + 2i\beta_m)^2/4) D_{\zeta_m}(\mu - b + 2i\beta_m)), \tag{5.56a}$$

$$\begin{aligned} \frac{\partial}{\partial v}\phi_m(v)\bigg|_{v=0+} &= C_+ i\beta_m \exp(-(\mu - b + 2i\beta_m)^2/4) D_{\zeta_m}(\mu - b + 2i\beta_m) \\ &\quad - C_+ \exp(-(v + \mu - b + 2i\beta_m)^2/4) D_{\zeta_m+1}(v + \mu - b + 2i\beta_m), \end{aligned} \tag{5.56b}$$

and we have for the negative half-space

$$-(\mu + b)\phi_m(0-) = -(\mu + b) C_- \exp(-(\mu + b - 2i\beta_m)^2/4) D_{\theta_m}(\mu + b - 2i\beta_m)), \tag{5.57a}$$

$$\begin{aligned} \frac{\partial}{\partial v}\phi_m(v)\bigg|_{v=0-} &= C_- i\beta_m \exp(-(\mu + b - 2i\beta_m)^2/4) D_{\theta_m}(\mu + b - 2i\beta_m) \\ &\quad + C_- \exp(-(v - \mu - b + 2i\beta_m)^2/4) D_{\theta_m+1}(\mu + b - 2i\beta_m). \end{aligned} \tag{5.57b}$$

Here, we have used an identity for the parabolic cylinder functions (Eq. (C.5a)).

Thus, the continuity of the probability current results in

$$\begin{aligned} & - C_- \exp(-(\mu+b-2i\beta_m)^2/4)(\mu+b-i\beta_m)D_{\theta_m}(\mu+b-2i\beta_m) \\ & + C_- \exp(-(\mu+b-2i\beta_m)^2/4)D_{\theta_m+1}(\mu+b-2i\beta_m)] \\ = \; & C_+ \exp(-(\mu-b+2i\beta_m)^2/4)(\mu-b+i\beta_m)D_{\zeta_m}(\mu-b+i\beta_m) \\ & - C_+ \exp(-(\mu-b+2i\beta_m)^2/4)D_{\zeta_m+1}(\mu-b+i\beta_m). \end{aligned} \tag{5.58}$$

Rearranging Eqs. (5.55) and (5.58) yields

$$C_- = C_+ \left[\frac{\exp(-(\mu-b+2i\beta_m)^2/4)}{\exp(-(\mu+b-2i\beta_m)^2/4)}\right] \frac{D_{\zeta_m}(\mu-b+2i\beta_m)}{D_{\theta_m}(\mu+b-2i\beta_m)}, \tag{5.59a}$$

$$\begin{aligned} C_- = C_+ & \left[\frac{\exp(-(\mu-b+2i\beta_m)^2/4)}{\exp(-(\mu+b-2i\beta_m)^2/4)}\right] \\ & \times \frac{(\mu-b+i\beta_m)D_{\zeta_m}(\mu-b+2i\beta_m) - D_{\zeta_m+1}(\mu-b+2i\beta_m)}{-(\mu+b-i\beta_m)D_{\theta_m}(\mu+b-2i\beta_m) + D_{\theta_m+1}(\mu+b-2i\beta_m)}. \end{aligned} \tag{5.59b}$$

Thus, the following condition must hold to have non-trivial solutions for C_-, C_+

$$\frac{D_{\zeta_m}(\mu-b+2i\beta_m)}{D_{\theta_m}(\mu+b-2i\beta_m)} = \frac{(\mu-b+i\beta_m)D_{\zeta_m}(\mu-b+2i\beta_m) - D_{\zeta_m+1}(\mu-b+2i\beta_m)}{-(\mu+b-i\beta_m)D_{\theta_m}(\mu+b-2i\beta_m) + D_{\theta_m+1}(\mu+b-2i\beta_m)}. \tag{5.60}$$

Rewriting Eq. (5.60) gives us the characteristic equation

$$\begin{aligned} & D_{\zeta_m}(\mu-b+2i\beta_m)\left[-(\mu+b-i\beta_m)D_{\theta_m}(\mu+b-2i\beta_m) + D_{\theta_m+1}(\mu+b-2i\beta_m)\right] \\ & -D_{\theta_m}(\mu+b-2i\beta_m)\left[(\mu-b+i\beta_m)D_{\zeta_m}(\mu-b+2i\beta_m) - D_{\zeta_m+1}(\mu-b+2i\beta_m)\right] \\ & = 0. \end{aligned} \tag{5.61}$$

By using an identity for parabolic cylinder functions (Eq. (C.3)), we can rewrite Eq. (5.61) in a similar form compared to Eq. (5.42), which facilitates cross checking

with other results

$$
\begin{aligned}
&D_{\Lambda_{n,m}+i\beta_m(\mu-b)-\beta_m^2}(\mu-b+2i\beta_m)[\Lambda_{n,m}-i\beta_m(\mu+b)-\beta_m^2] \\
&\times D_{\Lambda_{n,m}-i\beta_m(\mu+b)-\beta_m^2-1}(\mu+b-2i\beta_m) \\
&-D_{\Lambda_{n,m}-i\beta_m(\mu+b)-\beta_m^2}(\mu+b-2i\beta_m)[\Lambda_{n,m}+i\beta_m(\mu-b)-\beta_m^2] \\
&\times D_{\Lambda_{n,m}+i\beta_m(\mu-b)-\beta_m^2-1}(\mu-b+2i\beta_m) \\
&=0.
\end{aligned} \tag{5.62}
$$

To check the consistency of our result in Eq. (5.62) with the findings in Eq. (2.77), we set $\beta_m = 0$ ($\Lambda_{n,0} \to \Lambda_n$) and Eq. (5.62) changes to

$$
\Lambda_n \left[D_{\Lambda_n}(\mu-b) D_{\Lambda_n-1}(\mu+b) + D_{\Lambda_n}(\mu+b) D_{\Lambda_n-1}(\mu-b) \right] = 0. \tag{5.63}
$$

Eq. (5.63) represents the characteristic equation for the one-dimensional problem for the velocity [94] (see Eq. (2.77)). Fig. 5.5 shows the first two non-vanishing eigenvalues in terms of the constant force b for $\mu = 1.0$, (see Fig. 2.5 as well). By increasing b, the eigenvalues decrease towards the integers of the Ornstein-Uhlenbeck spectrum ($\Lambda_1 \to 1,\ \Lambda_2 \to 2$) (see Sec. 2.3).

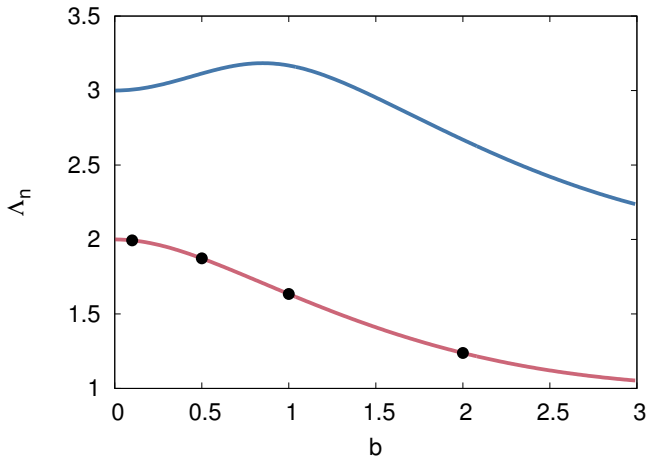

Figure 5.5: First two non-vanishing eigenvalues Λ_1 (red), Λ_2 (blue) as function of the constant force b, numerically obtained from Eq. (5.63) for $\mu = 1.0$. The black dots denote the values of the constant force b, which are used later in Fig. 5.8

If we consider the case without dry friction $\mu = 0$, the characteristic equation

(Eq. (5.62)) becomes

$$\begin{aligned} & D_{\Lambda_{n,m}-i\beta_m b-\beta_m^2}(-b+2i\beta_m)(\Lambda_{n,m}-i\beta_m b-\beta_m^2)D_{\Lambda_{n,m}-i\beta_m b-\beta_m^2-1}(b-2i\beta_m) \\ & -D_{\Lambda_{n,m}-i\beta_m b-\beta_m^2}(b-2i\beta_m)(\Lambda_{n,m}-i\beta_m b-\beta_m^2)D_{\Lambda_{n,m}-i\beta_m b-\beta_m^2-1}(-b+2i\beta_m) \\ = \; & 0. \end{aligned} \tag{5.64}$$

Using the product identity for parabolic cylinder functions (Eq. (C.6)), we obtain

$$\frac{\sqrt{2\pi}(\Lambda_{n,m}-i\beta_m b-\beta_m^2)}{\Gamma(-\Lambda_{n,m}+i\beta_m b+\beta_m^2-1)}=0. \tag{5.65}$$

From this equation we find the following result for the eigenvalues

$$\Lambda_{n,m}=n+\beta_m^2+ib\beta_m, \quad n\geq 0. \tag{5.66}$$

Eq. (5.66) is similar to Eq. (5.46) with the only difference being an additional contribution due to the constant force such that the degeneracy vanishes. Instead, the eigenvalues have an imaginary part now and we find again (see Eq. (5.51)) from Eq. (5.66) that $\bar{\Lambda}_{n,m}=\Lambda_{n,-m}$, i.e. the complex conjugate of an eigenvalue $\Lambda_{n,m}$ is the eigenvalue with the corresponding negative index m [82].

In comparison to the case $\beta_m = 0$, which is the eigenvalue problem of the Ornstein-Uhlenbeck process, the constant force has now an impact on the position of the eigenvalues in the complex plane for $m \neq 0$. To visualise the result from Eq. (5.66), we compute the eigenvalues $\Lambda_{1,m}$ with $m=-5,-4,\ldots,5$ for $b=2.0$, see Fig. 5.6.

We observe that $\Lambda_{1,0}=1$, which is the expected value coinciding with the spectrum of the Ornstein-Uhlenbeck process. The other eigenvalues $\Lambda_{1,m}$ with $m\neq 0$ have a larger real part due to the contribution of β^2 and an imaginary part, which becomes larger in terms of its absolute value the larger the index m is (or the smaller m is for negative integers). Furthermore, Fig. 5.6 illustrates nicely the relation $\bar{\Lambda}_{n,m}=\Lambda_{n,-m}$. To demonstrate the influence of b further, we compute the same eigenvalues $\Lambda_{1,m}$ as in Fig. 5.6 but now for different values of the constant force. The results are shown in Fig. 5.7.

We observe again that for $m=0$, the value of b does not matter and the eigenvalues lie on the real axis at $\Lambda_{1,0}=1$ for all chosen values of the constant force.

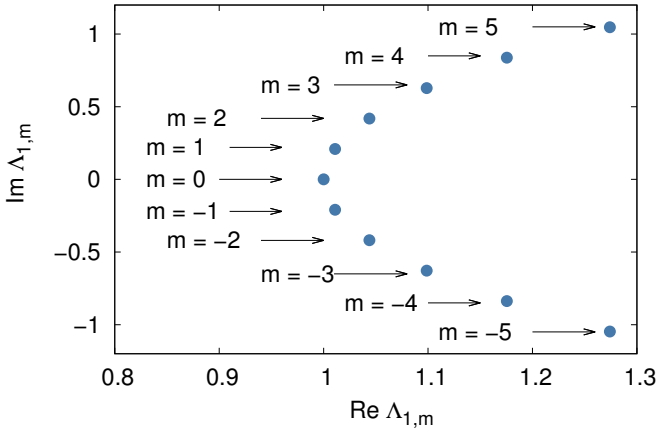

Figure 5.6: Eigenvalues $\Lambda_{1,m}$ with $m = -5, -4, \ldots, 5$ for $b = 2.0$ and $\mu = 0$. The results have been obtained from Eq. (5.66). Further parameter $L = 60$.

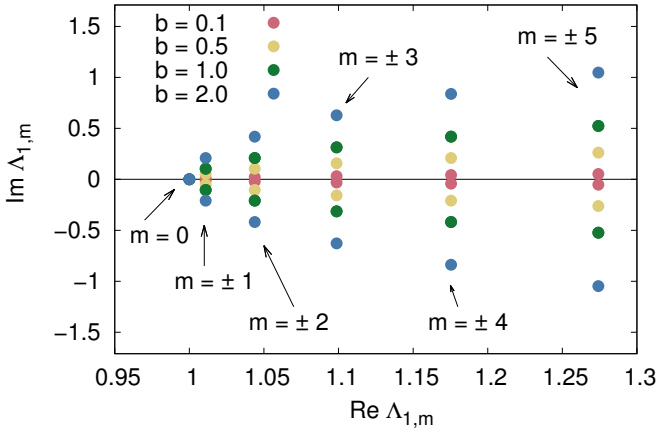

Figure 5.7: Eigenvalues $\Lambda_{1,m}$ with $m = -5, -4, \ldots, 5$ for different values of the constant force b and $\mu = 0$. The results have been obtained from Eq. (5.66). Further parameter $L = 60$.

For $m \neq 0$, the eigenvalues have an imaginary part (Eq. (5.66)) and now the value of b matters as for larger constant forces the absolute value of the imaginary part becomes larger, either with a positive or a negative sign. This depends on the sign of the index m and the sign of b, see Eq. (5.66). For $m = \pm 1$ only small differences for the eigenvalues can be observed but for $m = \pm 5$ it is clearly visible. As already seen in Fig. 5.6, the eigenvalues with a positive index m have a positive imaginary

part. Furthermore, as already observed in the previous section, the eigenvalues with the positive index m are the complex conjugate of the one with negative index.

Fig. 5.7 exhibits results for the problem without dry friction $\mu = 0$. Next, we will compute the eigenvalues $\Lambda_{1,m}$ (with $m = -5, -4, \ldots, 5$) by taking the dry friction into account. We use the same parameters as for Fig. 5.7, with the exception of μ, which we change from $\mu = 0$ to $\mu = 1$. In Fig. 5.8 we observe that the real part of

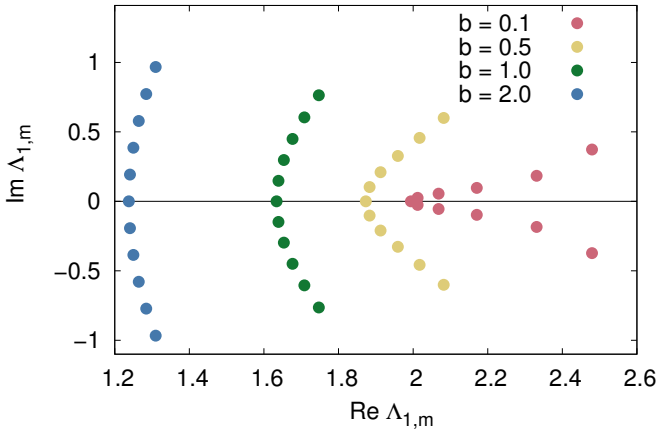

Figure 5.8: Eigenvalues $\Lambda_{1,m}$ with $m = -5, -4, \ldots, 5$ in the complex plane for different values of the constant force b ($\Lambda_{1,-5}$ represents the dot with the largest negative imaginary part, followed by $\Lambda_{1,-4}$ (see as well Fig. 5.6)). The eigenvalue $\Lambda_{1,0}$ coincides with the black dots in Fig. 5.5 for the respective value b. The results have been obtained numerically from Eq. (5.62). Further parameters: $\mu = 1.0$ and $L = 60$.

the eigenvalues decreases as we increase the constant force. This is in accordance with Fig. 5.5, where we could already observe such a decrease of the eigenvalues as a function of the constant force for $\mu \neq 0$. As an example for this result we can follow the eigenvalue $\Lambda_{1,0}$, which lies on the real axis in Fig. 5.8 and decreases for larger values of b. (the chosen value for b in Fig. 5.8 are represented by the black dots in Fig. 5.5). Nevertheless, the imaginary part of the eigenvalues increases, as we have already seen in Fig. 5.7 and in Eq. (5.66).

Next, we compute the eigenvalues for a fixed value of the constant force and vary the dry friction μ. Results for the eigenvalues $\Lambda_{1,m}$ with $m = -5, -4, \ldots, 5$ are shown for two different values of the constant force, $b = 0.5$ in Fig. 5.9 and $b = 1.5$ in Fig. 5.10. Fig. 5.9 shows that the eigenvalue $\Lambda_{1,0}$, which lies on the

real axis, becomes larger for increasing dry friction and so do the real parts of the other eigenvalues $\Lambda_{1,m}$ ($m \neq 0$). The absolute value of imaginary parts of the latter become larger as well for increasing μ. The largest difference can be observed for $\mu = 0$ and $\mu = 0.5$. Then, a change in the value of the imaginary part can only be noticed by looking at the values from the computations. However, in Fig. 5.9, this can hardly be seen. In Fig. 5.10, we can see a similar scenario for the larger value of the constant force b. In comparison to the previous figure, we note that the increase of $\Lambda_{1,0}$ and the real parts of the other eigenvalues is not as large as observed for a smaller constant force (Fig. 5.9). Furthermore, as it can be seen from Eq. (5.66), the absolute value of the imaginary parts of the eigenvalues $\Lambda_{1,m}$ ($m \neq 0$) is larger for a higher constant force.

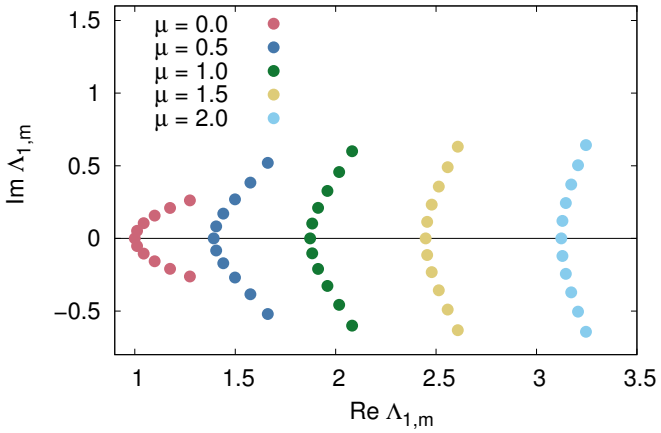

Figure 5.9: Eigenvalues $\Lambda_{1,m}$ with $m = -5, -4, \ldots, 5$ in the complex plane for different values of the dry friction μ and fixed constant force $b = -0.5$ ($\Lambda_{1,-5}$ represents the dot with the largest negative imaginary part, followed by $\Lambda_{1,-4}$ (see as well Fig. 5.6)). The results have been obtained numerically from Eq. (5.62). Further parameter: $L = 60$.

To underline our previous findings, we compute the eigenvalue $\Lambda_{1,3}$ as a function of the dry friction μ for different values of the constant force. As already indicated before in Figs. 5.9 and 5.10, we see in Fig. 5.11 that the real part becomes larger for an increase of the dry friction. The imaginary part increases as well, but depending on the value of the constant force, this increase is differently pronounced. For small b, the increase of the imaginary part is small, whereas for a larger value of b (e.g. $b = 1.0$ (blue curve in Fig. 5.11), we can observe a stronger increase below a certain

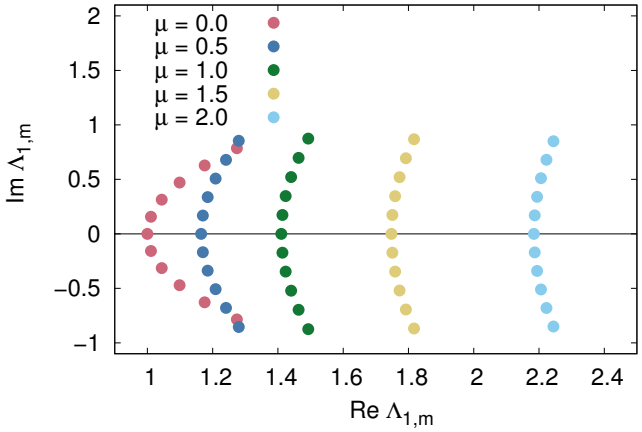

Figure 5.10: Eigenvalues $\Lambda_{1,m}$ with $m = -5, -4, \ldots, 5$ in the complex plane for different values of the dry friction μ and fixed constant force $b = -1.5$ ($\Lambda_{1,-5}$ represents the dot with the largest negative imaginary part, followed by $\Lambda_{1,-4}$ (see as well Fig. 5.6)). The results have been obtained numerically from Eq. (5.62). Further parameter: $L = 60$.

value of μ (here $\mu = 1.0$), then the imaginary part does not significantly change by varying the dry friction μ. Note again that the real part of the eigenvalue stays the same for $\mu = 0$, independent from b, as predicted from Eq. (5.66). For $\mu \neq 0$ this changes, as the real part is the largest for the lowest value of the constant force b, see the case for $\mu = 2.0$ in Fig. 5.10.

Thus, we find in general that increasing the dry friction increases the real part of the eigenvalues, whereas an influence towards the imaginary part is hardly visible. If we vary the constant force b, the real parts of the eigenvalues $\Lambda_{n,m}$ are not affected for $\mu = 0$, but for $\mu \neq 0$ the real parts decrease towards the value $n+\beta^2$, see Fig. 5.8. This could already be observed in the analysis of the problem for the velocity (there with $\beta = 0$), see Fig. 5.5.

If we consider the same analysis for one of the eigenvalues $\Lambda_{0,m}$ with $m \neq 0$ (as we have $\Lambda_{0,0} = 0$), we can see a different behaviour of the eigenvalues by varying the dry friction μ. In Fig. 5.12, the real part of the eigenvalue decreases if we increase the dry friction μ. Furthermore, the imaginary part decreases as well, such that for large values of the dry friction the differences between the eigenvalues for different values of the constant force b becomes smaller (see the results for $\mu = 2.0$ in Fig. 5.12). This very surprising result seems to be a special feature of the eigenvalues with $\Lambda_{0,m}$

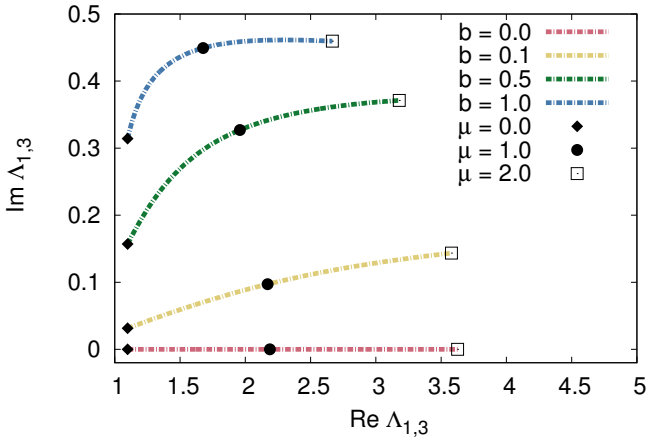

Figure 5.11: Eigenvalue $\Lambda_{1,3}$ in the complex plane as a function of the dry friction μ for different values of the constant force b. Three points have been marked as they represent specific values of the dry friction ($\mu = 0$ (black diamond), $\mu = 1.0$ (black dot) and $\mu = 2.0$ (black open square)). The results have been obtained numerically from Eq. (5.62) for 401 values of μ at an interval of $\Delta\mu = 0.005$. Note that exact results are available for $\mu = 0$ from Eq. (5.66). Further parameter $L = 60$.

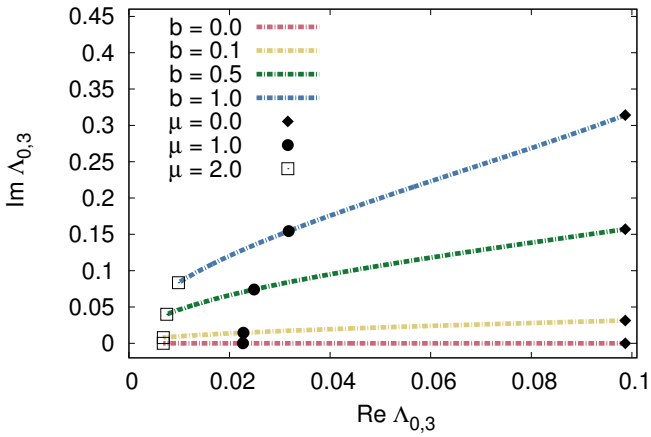

Figure 5.12: Eigenvalue $\Lambda_{0,3}$ in the complex plane as a function of the dry friction μ for different values of the constant force b. Three points have been marked as they represent specific values of the dry friction ($\mu = 0$ (black diamond), $\mu = 1.0$ (black dot) and $\mu = 2.0$ (black open square)). The results have been obtained numerically from Eq. (5.62) for 401 values of μ at an interval of $\Delta\mu = 0.005$. Note that exact results are available for $\mu = 0$ from Eq. (5.66). Further parameter $L = 60$.

and $m \neq 0$ as we could already observe such a behaviour in the previous section (see Fig. 5.4).

5.5 Summary of the chapter

In this chapter, we investigated a two-dimensional piecewise-smooth stochastic system with displacement x and velocity v, which does not obey detailed balance. More precisely, we studied the eigenvalues of the underlying Fokker-Planck operator with natural boundary conditions for the velocity and periodic boundary conditions for the displacement. This analysis has been done by following a similar approach as for the one-dimensional case of considering the velocity only [94]. We used a Fourier ansatz in x for the eigenfunctions, making use of the periodic boundary conditions. This enabled us to derive an equation for the eigenfunctions, which is of similar form as for the known problem of the one-dimensional problem of the velocity. The eigenfunctions can be represented by parabolic cylinder functions and we obtained the characteristic equation for the eigenvalues. The eigenvalues are labelled by two indices n and m as the second index arises from the Fourier ansatz for the eigenfunctions. Thus, for each eigenvalue with index n, branches of eigenvalues with the indices m and $-m$ arise. Our analysis has been performed only for eigenvalues with small indices n and m. This analysis has been done for the case without constant force and with constant force.

Without the constant force, we found that all eigenvalues are real and for $m \neq 0$ we have doubly degenerated eigenvalues as the eigenvalue with a positive integer m is the same as the corresponding eigenvalue with a negative integer. For $n \geq 1$ the eigenvalues become larger if we increase the dry friction μ. If we fix a value for μ we found that for odd integers m, the eigenvalue with a larger index is always larger than the eigenvalue with a smaller index (for positive m). This holds for even integers for small dry friction only, but for large dry friction, the eigenvalues change the order and for a fixed μ the eigenvalue $\Lambda_{n,0}$ is the largest compared to eigenvalues with the same n but different m. The eigenvalues with the smallest index $n = 0$ show a different behaviour compared to the eigenvalues with index $n \geq 1$ as they decrease if we increase the dry friction. This result implies that for large dry friction, the correlations of the displacement decay slower than for small dry friction.

Including a constant force in our model makes the degeneracy of the eigenvalues disappear and gives rise to an imaginary part. Now, the complex conjugate of an eigenvalue is the one with the corresponding negative index m. For the case without dry friction, an exact result can be found for the eigenvalues. By analysing an eigenvalue with index $n = 0$ but $m \neq 0$, the surprising result in terms of the dry friction μ appears as both real part and imaginary part decrease. This has been observed already in the case without the constant force.

As we varied the dry friction coefficient μ, we observed unexpected behaviour of the eigenvalues $\Lambda_{0,m}$. This behaviour is likely to play an important role for the stationary behaviour of the system. A more detailed analysis is needed to investigate the decrease of the eigenvalues more thoroughly as we just gave some qualitative results from a numerical analysis here.

Chapter 6

Conclusion and outlook

In this thesis, simple piecewise-smooth stochastic systems without detailed balance were investigated. We studied a dry friction model for the velocity of a particle subjected to exponentially correlated Ornstein-Uhlenbeck noise. In particular, we started with a pure dry friction model and afterwards we added viscous friction and a constant force to our dynamical equations. Furthermore, we considered the eigenvalue problem of a dry friction model with displacement and velocity. In the following, we will summarise the most important results.

Chapter 3 deals with the investigations of a pure dry friction model subjected to exponentially correlated Ornstein-Uhlenbeck noise. As analytical calculations are hampered due to the absence of detailed balance, the unified-coloured noise approximation has been applied. This approach returns quite good results for the stationary probability density of the velocity of a particle in comparison to numerical simulations. The distribution shows a Dirac δ peak at velocity zero, which reflects the phenomenon of sticking. For increasing correlation time, the sliding dynamics becomes less likely to take place as the noise amplitude decreases. By investigating the two-dimensional system (v, η) it was possible to find an analytical expression for the joint stationary probability distribution. This result does not obey the matching conditions at the discontinuity, but seems to be a useful description for large velocities and large noise amplitudes. To explore the dynamical characteristics of the model, i.e. correlations of the velocity, the correlation time of the velocity has been estimated via the power spectral density. For small noise correlation times, the result for the white noise has been recovered, but when the noise correlation time exceeds

a critical value, the correlations of the velocity increases. In addition, the power spectral density changes for increasing correlation times from a Lorentzian shape to a spectrum with quartic decay at high frequencies. Furthermore, sticking and sliding time distributions were explored. The former can be estimated via the exit time problem for the Ornstein-Uhlenbeck process with two absorbing boundaries. The investigation of the sliding time distributions exhibits a surprising universal behaviour for large correlation times. We observe a power law decay for small sliding times, a strong exponential decay for a small range of intermediate sliding times and an exponential cut-off for large sliding times.

In Chapter 4, the previously studied model has been extended by adding viscous friction and a constant force. The additional constant force changes the sticking condition, whereas the viscous friction only limits the velocity in attaining large values. We again used the unified-coloured noise approximation to estimate the marginal stationary probability distribution of the velocity. The probability of sticking exhibits a non-monotonic behaviour as a function of the correlation time in the sliding regime, i.e. above the deterministic stick-slip transition. Such a feature has already been indicated by investigating the time traces of the velocity. The correlations of the velocity were evaluated by computing the power spectral density. For large correlation times of the noise, the correlation time of the velocity increases as already observed for the pure dry friction case. If we increase the viscous friction while being in the small noise correlation regime, the correlations for the velocity decrease, which is in accordance with the results of the known Ornstein-Uhlenbeck process. For high correlations of the noise, results for different values of the viscous friction are nearly indistinguishable. Adding a constant force, its impact is only visible for small noise correlations and small values of the viscous friction. However, for high viscous friction the constant force only plays a marginal role. By investigating the sticking time distributions, no significant differences can be observed among a value of the constant force in the sliding regime and a value in the sticking regime for small correlations of the noise. Only for very large noise correlations, we see that only short sticking time periods occur in the sliding regime, whereas in the sticking regime larger sticking periods are observed. Finally, we obtained the surprising result that the sliding time distribution does not significantly change through the impact of additional viscous friction and constant bias.

Furthermore, we explored the eigenvalue problem of a dry friction model with

displacement and velocity subjected to Gaussian white noise in Chapter 5. While we imposed natural boundaries for the velocity, the dynamics of the displacement has been limited by periodic boundary conditions. The latter enabled us to expand the eigenfunctions in a Fourier series for the displacement. In the end, we obtained an eigenvalue equation for the Fokker-Planck operator, which can be solved in a similar way to the one-dimensional case for the velocity only. Considering the system without the constant force, the characteristic equation can be found by making use of appropriate symmetry relations for the velocity at the discontinuity. All eigenvalues are real and for each eigenvalue with index n additional branches with double degenerated eigenvalues denoted by the index m arise due to the periodic boundaries. Without the dry friction, it is possible to find exact results for the eigenvalues. With increasing dry friction the eigenvalues with index $n \geq 1$ increase, whereas the eigenvalues $n = 0$ surprisingly decrease. Adding a constant force gives rise to imaginary parts of the eigenvalues. The degeneracy is removed and now each eigenvalue $\Lambda_{n,m}$ with $m \neq 0$ has a corresponding complex conjugate eigenvalue $\Lambda_{n,-m}$. For a non zero dry friction, the real parts of the eigenvalues decrease, which is in accordance with the one-dimensional problem for the velocity only. However, the imaginary parts increase for higher values of the constant force. The same surprising result as in the previous section was discovered for the eigenvalues $\Lambda_{0,m}$ as they decrease towards zero for increasing dry friction, regardless of whether the constant force is zero or not.

Open problems

Here we would like to draw attention to some open problems that are closely related to the investigations in this thesis. Furthermore, we believe that they could be useful links to studies related to two-dimensional piecewise-smooth stochastic systems.

Dry friction model with displacement and velocity

As we only analysed a part of the eigenvalue spectrum of the Fokker-Planck operator for the dry friction model including position and velocity (Chapter 5), further details can be elaborated on this model. In [94], the authors found asymptotic expression for eigenvalues with large index n and for large parameter values of the dry

friction. A similar analysis might be useful to gain a deeper insight into the spectral representation of the underlying propagator.

Another interesting aspect is the question of whether it is possible to compute the marginal propagator for the displacement analytically from the joint propagator. Such a result would allow us to investigate the impact of dry friction to the displacement analytically to a large extent. As in the stationary limit the smallest eigenvalues of the system contribute the most, it would also be interesting to check whether it is possible to perform a Taylor expansion for small eigenvalues from the obtained results in Chapter 5. This would mean that a Taylor expansion needs to be done for the index of the parabolic cylinder functions, which is clearly a very challenging task. Nevertheless, findings from such an analysis might provide a very useful insight into the impact of dry friction on the displacement.

Furthermore, it might be of interest to investigate whether exit time problems for the displacement can be solved analytically and semi-analytically by using the theoretical framework shown in Chapter 5. Different boundary conditions have to be chosen then, as they need to absorbing boundaries. Such results will be interesting not only from a theoretical point of view but for experimental setups as well.

Brownian motion with dry friction in a harmonic potential

Another related piecewise-smooth stochastic model considering displacement and velocity is the problem of Brownian motion in a harmonic potential including dry friction. The deterministic counterpart has attracted a lot of attention over the past decades [24,51,103]. In the case of the piecewise-smooth stochastic system, the underlying Fokker Planck equation reads

$$\begin{aligned}\frac{\partial}{\partial t}P(x,v,t|x_0,v_0,0) &= \left[-v\frac{\partial}{\partial x}+\frac{\partial}{\partial v}\left(\gamma v+kx+\nu\sigma(v)-F\right)\right]P(x,v,t|x_0,v_0,0)\\ &\quad+\frac{1}{2}\frac{\partial^2}{\partial v^2}P(x,v,t|x_0,v_0,0).\end{aligned}\tag{6.1}$$

Here k denotes the spring constant. Due to the lack of detailed balance, it is very difficult to find a solution for the joint stationary distribution $P(x,v)$, which satisfies all the necessary boundary and matching conditions. In the absence of the dry friction and the constant force, we obtain the classic textbook example [17], where analytical solutions for the propagator and the stationary joint distribution are

available. Therefore, an approach in terms of a perturbation theory could help here to find analytical estimates to the problem. The idea is to treat the part responsible for the stick-slip dynamics $\nu\sigma(v) + F$ as a perturbation. Therefore, we introduce the perturbation parameter ε

$$\left[-v\frac{\partial}{\partial x} + \frac{\partial}{\partial v}(\gamma v + kx) + \frac{1}{2}\frac{\partial^2}{\partial v^2}\right] P(x,v) + \varepsilon\frac{\partial}{\partial v}(\nu\sigma(v) - F)P(x,v) = 0. \tag{6.2}$$

We expand the stationary distribution in terms of the perturbation parameter ε

$$P(x,v) = P_0(x,v) + \varepsilon P_1(x,v) + \varepsilon^2 P_2(x,v)\ldots \tag{6.3}$$

In the lowest order ($\varepsilon = 0$), we arrive at the known problem

$$\left[-v\frac{\partial}{\partial x} + \frac{\partial}{\partial v}(\gamma v + kx) + \frac{1}{2}\frac{\partial^2}{\partial v^2}\right] P(x,v) = 0, \tag{6.4}$$

and the solution is

$$P_0(x,v) = \frac{\gamma\sqrt{k}}{\pi}\exp\left(-k\gamma x^2 - \gamma v^2\right). \tag{6.5}$$

For the next order in ε, we have to solve the following equation

$$\left[-v\frac{\partial}{\partial x} + \frac{\partial}{\partial v}(\gamma v + kx) + \frac{1}{2}\frac{\partial^2}{\partial v^2}\right] P_1(x,v) + \frac{\partial}{\partial v}(\nu\sigma(v) - F)P_0(x,v) = 0. \tag{6.6}$$

A solution for $P_1(x,v)$ could be found via a double Fourier transform and solving the equation in Fourier space or by using an expansion into Hermite polynomials, i.e. the eigenfunctions of the unperturbed problem (Eq. (6.4)). As such a result would probably only be valid for small values of the dry friction and the constant force, the question is whether, for example, stick-slip transitions can be observed or whether the impact of the dry friction is too small.

Nonlinear friction models

In this thesis we have set the static friction μ_S and the kinetic friction μ_C equal. To describe the situation that the static friction is larger than the kinetic friction $\mu_S > \mu_C$, which is more likely to happen in real world, the dynamical equation for

the velocity has to change towards

$$\dot{v}(t) = \begin{cases} 0 & \text{if } |F + F_{Rand}(t)| < \mu_S \text{ and } v = 0, \\ -\gamma v(t) - \mu_C \sigma_0(v(t)) + F + F_{Rand}(t) & \text{otherwise.} \end{cases} \tag{6.7}$$

F_{Rand} denotes a stochastic force, which could be for example a Gaussian white noise or an Ornstein-Uhlenbeck noise. The force $F + F_{Rand}(t)$ applied to our system still has to overcome the static friction μ_S, but, for $v \neq 0$ a smaller contribution $\mu_C \sigma_0(v(t))$ now enters the dynamical equation. Such a system can exhibit friction characteristics like hysteresis. Another aspect to consider is that in a scenario described above, the dry friction is modelled by

$$F_{fri}(v) = \mu_C \sigma_0(v(t)) \tag{6.8}$$

which means we have a jump in the dry friction contribution if we go from $v = 0$ to $v \neq 0$. To ensure a smooth transition, this could be modelled by, for example,

$$F_{fri}(v) = \mu_C \left(1 + \frac{\mu_S - \mu_C}{\mu_C} g(v)\right) \sigma_0(v) \tag{6.9}$$

where $g(v)$ is nonlinear function describing the transition from the static friction at $v = 0$ and the kinetic friction at $v \neq 0$. A candidate for such a nonlinear function could be an exponential function, for example. More details on such an approach to model the dry friction can be found in [100].

Coupled stochastic systems with dry friction

While this thesis and large parts of existing research have considered only a single particle subjected to dry friction and stochastic perturbations, it might be very interesting to investigate coupled piecewise-smooth stochastic systems. Recently, coupled deterministic models have been studied, e.g. the dynamics of two coupled dry friction oscillators [77, 78] or a network of dry friction oscillators towards synchronisation properties using the master stability function concept [70]. In addition, chains of solid blocks connectd via springs and subjected to dry friction have been used in investigations and modelling of earthquakes [13, 14]. Thus, it could be interesting to investigate the robustness of phenomena discovered for determin-

istic systems against noisy perturbations or the additional noise could lead to new phenomena, which are not visible for deterministic systems.

Experiments

Finally, it would be desirable to compare the theoretically obtained results for the system subjected to coloured noise with experimental data. For example, different probability distributions for different noise correlation times could be measured to compare whether or not a similar transition from sliding to sticking appears. In addition, experiments could answer the question on whether the idealisation of equal static and kinetic friction is appropriate or whether more complex friction models are needed to describe the underlying dynamics. Appropriate experimental setups could be the ones used for the water droplets on the vibrating substrate, e.g. [42,43]. The coloured noise could be realised by a noise generator to change the vibrations of the solid plate, on which the solid object is placed.

Appendix A

Euler-Maruyama scheme

Here we want to show the derivation of an numerical algorithm for stochastic differential equations [60], which is used in this thesis. We consider the following stochastic differential equation

$$\dot{v}(t) = -a(v(t)) + \sqrt{D}\xi(t) \tag{A.1}$$

on a time interval $[0, T]$. $a(v(t))$ represents a drift function and we only consider additive noise here. Integration of Eq. (A.1) yields

$$v(T) = v(0) - \int_0^T a(v(t))dt + \int_0^T \sqrt{D}\xi(t)dt. \tag{A.2}$$

To construct the numerical integration scheme, we divide the time interval into N subintervals of size $\Delta t = T/N$ and we evaluate $v(t)$ at each point $t_n = n\Delta t$. In such a subinterval, we have

$$v(t_{n+1}) = v(t_n) - \int_{t_n}^{t_{n+1}} a(v(t))dt + \int_{t_n}^{t_{n+1}} \sqrt{D}\xi(t)dt. \tag{A.3}$$

As $\xi(t)$ is Gaussian (Eq. (1.3)), $\int_{t_n}^{t_{n+1}} \xi(t)dt$ is also Gaussian, as we have

$$\left\langle \int_{t_n}^{t_{n+1}} \xi(t)dt \right\rangle = \int_{t_n}^{t_{n+1}} \langle \xi(t) \rangle dt = 0 \tag{A.4}$$

and

$$\begin{aligned}\left\langle \left(\int_{t_n}^{t_{n+1}} \xi(t)dt \right)^2 \right\rangle &= \int_{t_n}^{t_{n+1}} \int_{t_n}^{t_{n+1}} \langle \xi(t)\xi(t') \rangle dtdt' \\ &= \int_{t_n}^{t_{n+1}} \int_{t_n}^{t_{n+1}} \delta(t-t')dtdt' \\ &= t_{n+1} - t_n \\ &= \Delta t. \end{aligned} \tag{A.5}$$

If Δt is small enough, for a subinterval $[t_n, t_{n+1}]$ we have

$$\int_{t_n}^{t_{n+1}} a(v(t))dt \approx a(v(t_n))\Delta t \tag{A.6}$$

and

$$\int_{t_n}^{t_{n+1}} \sqrt{D}\xi(t)dt = \sqrt{D}dW_n \tag{A.7}$$

where dW_n denotes the increment of the Wiener process

$$dW_n = W_{t_{n+1}} - W_{t_n} \sim \mathcal{N}(0, t_{n+1} - t_n). \tag{A.8}$$

$\mathcal{N}(0, t_{n+1}-t_n)$ represents the normal distribution with mean 0 and variance $t_{n+1}-t_n$. Thus, dW_n can be generated from a standard normal distribution

$$dW_n \sim \sqrt{\Delta t}\mathcal{N}(0,1) \tag{A.9}$$

with $\Delta t = t_{n+1} - t_n$. Note that we have used the relation $\frac{dW}{dt} = \xi(t)$ in Eq. (A.7), which only applies in a distributional sense as the Wiener process is nowhere differentiable.

Finally, denoting $n+1 = t_{n+1}$, we have the numerical algorithm to solve Eq. (A.1)

$$v_{n+1} = v_n - a(v_n)\Delta t + \sqrt{D\Delta t}\mathcal{N}(0,1). \tag{A.10}$$

Appendix B

Rescaling of variables

Here we demonstrate how the variables in the Langevin equation and the Fokker-Planck equation are rescaled to consider the problem in non-dimensional units, or in other words, how the number of contributing system parameters can be reduced. In this section, we perform the rescaling for the Fokker-Planck equation; it can be done in the same way for the Langevin equation.

Considering a one-dimensional problem in x, we have the Fokker-Planck equation for the propagator $p(x,t|x_0,0)$

$$\frac{\partial}{\partial t}p(x,t|x_0,0) = -\frac{\partial}{\partial x}h(x)p(x,t|x_0,0) + \frac{\chi}{2}\frac{\partial^2}{\partial x^2}p(x,t|x_0,0) \tag{B.1}$$

with the function $h(x)$, which represents the drift, and the diffusion (which does not depend on x) is represented by χ. We apply the transformation

$$u = c_1 x, \quad z = c_3 t \tag{B.2}$$

and we obtain the propagator for the new variables $q(u,z|u_0,0)$ via

$$q(u,z|u_0,0) = \frac{p(x,t|x_0,0)}{c_1}. \tag{B.3}$$

The contributions in the Fokker-Planck equation (Eq. (B.1)) change due to the

transformation

$$\frac{\partial}{\partial t}p(x,t|x_0,0) = c_1 c_3 \frac{\partial}{\partial z}q(u,z|u_0,0), \tag{B.4a}$$

$$\frac{\partial}{\partial x}h(x)p(x,t|x_0,0) = c_1^2 \frac{\partial}{\partial u}h\left(\frac{u}{c_1}\right)q(u,z|u_0,0), \tag{B.4b}$$

$$\frac{\partial^2}{\partial x^2}p(x,t|x_0,0) = c_1^3 \frac{\partial^2}{\partial u^2}q(u,z|u_0,0). \tag{B.4c}$$

Thus, the full Fokker-Planck equation for the new variables reads

$$\frac{\partial}{\partial z}q(u,z|u_0,0) = -\frac{c_1}{c_3}\frac{\partial}{\partial u}h\left(\frac{u}{c_1}\right)q(u,z|u_0,0) + \frac{c_1^2}{c_3}\frac{\chi}{2}\frac{\partial^2}{\partial u^2}q(u,z|u_0,0). \tag{B.5}$$

For a two-dimensional system (x,y), the Fokker-Planck equation is

$$\begin{aligned}\frac{\partial}{\partial t}p(x,y,t|x_0,y_0,0) &= -\frac{\partial}{\partial x}g(x,y)p(x,y,t|x_0,y_0,0) \\ &\quad -\frac{\partial}{\partial y}h(x,y)p(x,y,t|x_0,y_0,0) \\ &\quad +\frac{\chi}{2}\frac{\partial^2}{\partial y^2}p(x,y,t|x_0,y_0,0),\end{aligned} \tag{B.6}$$

where we have the drift functions $g(x,y)$ and $h(x,y)$ and the diffusion constant χ. Here we use the transformation

$$u = c_1 x, \quad w = c_2 y, \quad z = c_3 t, \tag{B.7}$$

and the new propagator is

$$q(u,w,z|u_0,w_0,0) = \frac{p(x,y,t|x_0,y_0,0)}{c_1 c_2}. \tag{B.8}$$

Similarly to Eqs. (B.4a) - (B.4c), the contributions of the Fokker-Planck equation

change

$$\frac{\partial}{\partial t}p(x,y,t|x_0,y_0,0) = c_1c_2c_3\frac{\partial}{\partial z}q(u,w,z|u_0,w_0,0), \tag{B.9a}$$

$$\frac{\partial}{\partial x}g(x,y)p(x,y,t|x_0,y_0,0) = c_1^2c_2\frac{\partial}{\partial u}g\left(\frac{u}{c_1},\frac{w}{c_2}\right)q(u,w,z|u_0,w_0,0), \tag{B.9b}$$

$$\frac{\partial}{\partial y}h(x,y)p(x,y,t|x_0,y_0,0) = c_1c_2^2\frac{\partial}{\partial w}h\left(\frac{u}{c_1},\frac{w}{c_2}\right)q(u,w,z|u_0,w_0,0), \tag{B.9c}$$

$$\frac{\partial^2}{\partial y^2}p(x,y,t|x_0,y_0,0) = c_1c_2^3\frac{\partial^2}{\partial w^2}q(u,w,z|u_0,w_0,0). \tag{B.9d}$$

Finally, from Eqs. (B.9a) - (B.9d) we get

$$\begin{aligned}\frac{\partial}{\partial z}q(u,w,z|u_0,w_0,0) \;=\; & -\frac{c_1}{c_3}\frac{\partial}{\partial u}g\left(\frac{u}{c_1},\frac{w}{c_2}\right)q(u,w,z|u_0,w_0,0)\\ & -\frac{c_2}{c_3}\frac{\partial}{\partial w}h\left(\frac{u}{c_1},\frac{w}{c_2}\right)q(u,w,z|u_0,w_0,0)\\ & +\frac{c_2^2}{c_3}\frac{\chi}{2}\frac{\partial^2}{\partial w^2}q(u,w,z|u_0,w_0,0).\end{aligned} \tag{B.10}$$

In the following sections (B.1 - B.8), we will apply these results to the different Fokker-Planck equations, that are investigated in this thesis.

B.1 Ornstein-Uhlenbeck process with white noise

The Fokker-Planck equation reads

$$\frac{\partial}{\partial t}p(v,t|v_0,0) = \frac{\partial}{\partial v}\gamma v p(v,t|v_0,0) + \frac{D}{2}\frac{\partial^2}{\partial v^2}p(v,t|v_0,0). \tag{B.11}$$

Thus, we have $h(v) = -\gamma v$ and $\chi = D$. Using Eq. (B.5), we get

$$\frac{\partial}{\partial z}q(u,z|u_0,0) = \frac{\gamma}{c_3}\frac{\partial}{\partial u}uq(u,z|u_0,0) + \frac{c_1^2}{c_3}\frac{D}{2}\frac{\partial^2}{\partial u^2}q(u,z|u_0,0). \tag{B.12}$$

Although it is possible to rescale the variables in order to change to an equation without any system parameter left (with $c_1 = \sqrt{2\gamma/D},\ c_3 = \gamma$), we choose $c_3 = 1$, $c_1 = D^{-1/2}$ and keep γ to facilitate the demonstration of several concepts and methods (see Sec. 2.1). The rescaled Fokker-Planck equation can be found in

Eq. (2.2).

B.2 Ornstein-Uhlenbeck process driven by coloured noise

The Fokker-Planck equation for this system reads

$$\begin{aligned}\frac{\partial}{\partial t}p(v,\eta,t|v_0,\eta_0,0) &= \frac{\partial}{\partial v}(\gamma v-\eta)p(v,\eta,t|v_0,\eta_0,0)+\frac{\partial}{\partial \eta}\frac{\eta}{\tau}p(v,\eta,t|v_0,\eta_0,0)\\ &\quad+\frac{D}{2\tau^2}\frac{\partial^2}{\partial\eta^2}p(v,\eta,t|v_0,\eta_0,0).\end{aligned} \tag{B.13}$$

As this problem is two-dimensional, we use Eq. (B.10). With $g(v,\eta)=-\gamma v+\eta,\ h(v,\eta)=-\eta/\tau,\ \chi=D/\tau^2$ we have

$$\begin{aligned}\frac{\partial}{\partial z}q(u,w,z|u_0,w_0,0) &= \frac{\partial}{\partial u}\left(\frac{\gamma}{c_3}u-\frac{c_1}{c_2c_3}w\right)q(u,w,z|u_0,w_0,0)\\ &\quad+\frac{\partial}{\partial w}\frac{w}{c_3\tau}q(u,w,z|u_0,w_0,0)\\ &\quad+\frac{c_2^2}{c_3}\frac{D}{2\tau^2}\frac{\partial^2}{\partial w^2}q(u,w,z|u_0,w_0,0).\end{aligned} \tag{B.14}$$

Here we choose $c_1=c_2=D^{-1/2},\ c_3=1$ to keep the parameters γ and τ. The rescaled Fokker-Planck equation corresponds to the dynamical equations Eqs. (2.12) and (2.14).

B.3 Pure dry friction and white noise

Here we have the Fokker-Planck equation

$$\frac{\partial}{\partial t}p(v,t|v_0,0)=\frac{\partial}{\partial v}\nu\sigma(v)p(v,t|v_0,0)+\frac{D}{2}\frac{\partial^2}{\partial v^2}p(v,t|v_0,0). \tag{B.15}$$

With $h(v)=-\nu\sigma(v)$ and $\chi=D$, we get

$$\frac{\partial}{\partial z}q(u,z|u_0,0)=\frac{\partial}{\partial u}\frac{c_1}{c_3}\nu\sigma(u)q(u,z|u_0,0)+\frac{c_1^2}{c_3}\frac{D}{2}\frac{\partial^2}{\partial u^2}q(u,z|u_0,0). \tag{B.16}$$

We rescale all variables to non-dimensional units by choosing

$$\frac{c_1}{c_3}\nu = 1, \quad \frac{c_1^2}{c_3}\frac{D}{2} = 1 \tag{B.17}$$

and obtain $c_1 = \frac{2\nu}{D},\ c_3 = \frac{2\nu^2}{D}$. The rescaled Fokker-Planck equation can be seen in Eq. (1.7).

B.4 Dry friction, viscous friction and white noise

Here the Fokker-Planck equation is

$$\frac{\partial}{\partial t}p(v,t|v_0,0) = \frac{\partial}{\partial v}\left[\gamma v + \nu\sigma(v)\right]p(v,t|v_0,0) + \frac{D}{2}\frac{\partial^2}{\partial v^2}p(v,t|v_0,0), \tag{B.18}$$

which gives us $h(v) = -\gamma v - \nu\sigma(v)$ and $\chi = D$. Thus, we consider

$$\frac{\partial}{\partial z}q(u,z|u_0,0) = \frac{\partial}{\partial u}\left[\frac{\gamma}{c_3}u + \frac{c_1}{c_3}\nu\sigma(u)\right]q(u,z|u_0,0) + \frac{c_1^2}{c_3}\frac{D}{2}\frac{\partial^2}{\partial u^2}q(u,z|u_0,0). \tag{B.19}$$

We choose

$$\frac{\gamma}{c_3} = 1, \quad \frac{c_1^2}{c_3}\frac{D}{2} = 1 \tag{B.20}$$

and obtain $c_1 = \sqrt{\frac{2\gamma}{D}}, c_3 = \gamma$. Therefore, the rescaled coefficient for the dry friction is $\mu = \sqrt{\frac{D}{2\gamma}}\nu$. The rescaled Fokker-Planck equation corresponds to the drift function in Eq. (2.60).

B.5 Dry friction, viscous friction, constant bias and white noise

The Fokker-Planck equation reads

$$\frac{\partial}{\partial t}p(v,t|v_0,0) = \frac{\partial}{\partial v}\left[\gamma v + \nu\sigma(v) - F\right]p(v,t|v_0,0) + \frac{D}{2}\frac{\partial^2}{\partial v^2}p(v,t|v_0,0). \tag{B.21}$$

We have $h(v) = -\gamma v - \nu\sigma(v) + F$ and $\chi = D$. Therefore, we get

$$\begin{aligned}\frac{\partial}{\partial z}q(u,z|u_0,0) &= \frac{\partial}{\partial u}\left[\frac{\gamma}{c_3}u + \frac{c_1}{c_3}\nu\sigma(u) - \frac{c_1}{c_3}F\right]q(u,z|u_0,0) \\ &\quad + \frac{c_1^2}{c_3}\frac{D}{2}\frac{\partial^2}{\partial u^2}q(u,z|u_0,0). \end{aligned} \tag{B.22}$$

We make the same choice as in Eq. (B.20) and obtain the two rescaled parameters $\mu = \sqrt{\frac{D}{2\gamma}}\nu$ and $b = \sqrt{\frac{D}{2\gamma}}F$. The rescaled system corresponds to the drift function in Eq. (2.72).

B.6 Pure dry friction and coloured noise

The Fokker-Planck equation is

$$\begin{aligned}\frac{\partial}{\partial t}p(v,\eta,t|v_0,\eta_0,0) &= \frac{\partial}{\partial v}(\nu\sigma_0(v) - \eta)p(v,\eta,t|v_0,\eta_0,0) + \frac{\partial}{\partial \eta}\frac{\eta}{\tau}p(v,\eta,t|v_0,\eta_0,0) \\ &\quad + \frac{D}{2\tau^2}\frac{\partial^2}{\partial \eta^2}p(v,\eta,t|v_0,\eta_0,0). \end{aligned} \tag{B.23}$$

Here we have $g(v,\eta) = -\nu\sigma_0(v) + \eta,\ h(v,\eta) = -\eta/\tau,\ \chi = D/\tau^2$ and we obtain

$$\begin{aligned}\frac{\partial}{\partial z}q(u,w,z|u_0,w_0,0) &= \frac{\partial}{\partial u}\left(\frac{c_1\nu}{c_3}\sigma_0(u) - \frac{c_1}{c_2c_3}w\right)q(u,w,z|u_0,w_0,0) \\ &\quad + \frac{\partial}{\partial w}\frac{w}{c_3\tau}q(u,w,z|u_0,w_0,0) \\ &\quad + \frac{c_2^2}{c_3}\frac{D}{2\tau^2}\frac{\partial^2}{\partial w^2}q(u,w,z|u_0,w_0,0). \end{aligned} \tag{B.24}$$

As we want to study the impact of the correlation time τ, we choose $c_1 = \frac{1}{D\nu^3}$, $c_2 = \nu$, $c_3 = \frac{1}{D\nu^2}$. We obtain a rescaled correlation time $\tau_{eff} = \frac{\tau}{D\nu^2}$ and arrive at the corresponding Eqs. (3.1) and (3.2). Note that we have dropped the label $_{eff}$ Chapter 3 for convenience.

B.7 Dry friction, viscous friction, constant bias and coloured noise

The underlying Fokker-Planck equation reads

$$\begin{aligned}\frac{\partial}{\partial t}p(v,\eta,t|v_0,\eta_0,0) &= \frac{\partial}{\partial v}\left[\gamma v+\nu\sigma_0(v)-F-\eta\right]p(v,\eta,t|v_0,\eta_0,0)\\ &+\frac{\partial}{\partial\eta}\frac{\eta}{\tau}p(v,\eta,t|v_0,\eta_0,0)\\ &+\frac{D}{2\tau^2}\frac{\partial^2}{\partial\eta^2}p(v,\eta,t|v_0,\eta_0,0).\end{aligned}\tag{B.25}$$

Here we have $g(v,\eta)=-\gamma v-\nu\sigma_0(v)+F+\eta,\ h(v,\eta)=-\eta/\tau,\ \chi=D/\tau^2$ and this leads to

$$\begin{aligned}\frac{\partial}{\partial z}q(u,w,z|u_0,w_0,0) &= \frac{\partial}{\partial u}\left[\frac{\gamma}{c_3}u+\frac{c_1\nu}{c_3}\sigma_0(u)-\frac{c_1F}{c_3}-\frac{c_1}{c_2c_3}w\right]q(u,w,z|u_0,w_0,0)\\ &+\frac{1}{c_3}\frac{\partial}{\partial w}\frac{w}{\tau}q(u,w,z|u_0,w_0,0)\\ &+\frac{c_2^2}{c_3}\frac{D}{2\tau^2}\frac{\partial^2}{\partial w^2}q(u,w,z|u_0,w_0,0).\end{aligned}\tag{B.26}$$

We choose again $c_1=\frac{1}{D\nu^3}$, $c_2=\nu$, $c_3=\frac{1}{D\nu^2}$. Thus, the correlation time is scaled as previously $\tau_{eff}=\frac{\tau}{D\nu^2}$, the effective viscous friction is $\gamma_{eff}=\gamma D\nu^2$ and the constant force is scaled with the dry friction coefficient $b=\frac{F}{\nu}$. The corresponding dynamical equations are Eqs. (4.1) and (4.3). Note that we have dropped the label $_{eff}$ in Chapter 4 for convenience.

B.8 Dry friction model with displacement and velocity

Here the underlying Fokker-Planck equation is

$$\begin{aligned}\frac{\partial}{\partial t}p(x,v,t|x_0,v_0,0) &= -\frac{\partial}{\partial x}vp(x,v,t|x_0,v_0,0) \\ &+ \frac{\partial}{\partial v}[\gamma v + \nu\sigma(v) - F]p(x,v,t|x_0,v_0,0) \\ &+ \frac{D}{2}\frac{\partial^2}{\partial v^2}p(x,v,t|x_0,v_0,0). \end{aligned} \tag{B.27}$$

This gives us $g(x,v) = v,\ h(x,v) = -\gamma v - \nu\sigma_0(v) + F,\ \chi = D$ and we obtain

$$\begin{aligned}\frac{\partial}{\partial z}q(u,w,z|u_0,w_0,0) &= -\frac{c_1}{c_2c_3}w\frac{\partial}{\partial u}q(u,w,z|u_0,w_0,0) \\ &+ \frac{\partial}{\partial w}\left[\frac{\gamma}{c_3}u + \frac{c_2\nu}{c_3}\sigma(u) - \frac{c_2F}{c_3}\right]q(u,w,z|u_0,w_0,0) \\ &+ \frac{c_2^2}{c_3}\frac{D}{2}\frac{\partial^2}{\partial w^2}q(u,w,z|u_0,w_0,0). \end{aligned} \tag{B.28}$$

We choose

$$\frac{c_1}{c_2c_3} = 1,\ \frac{\gamma}{c_3} = 1,\ \frac{c_2^2}{c_3}\frac{D}{2} = 1. \tag{B.29}$$

and obtain $c_1 = \sqrt{\frac{2\gamma^3}{D}}$, $c_2 = \sqrt{\frac{2\gamma}{D}}$, $c_3 = \gamma$. As in Sec. B.5, we have a rescaled dry friction coefficient $\mu = \sqrt{\frac{2}{D\gamma}}\nu$ and a rescaled constant force $b = \sqrt{\frac{2}{D\gamma}}F$. The corresponding equations of motion are Eqs. (5.1a) and (5.1b).

Appendix C

Properties of special functions

In this section we want to give a short introduction to some special functions, which are used in this thesis. First, we will introduce the parabolic cylinder functions and afterwards we will discuss aspects of the confluent hypergeometric function of the first kind. This section is mainly based on [2, 12, 29, 66].

C.1 Parabolic cylinder functions

The parabolic cylinder functions, also named Weber functions, are special functions, which satisfy the following differential equation:

$$\frac{d^2}{dz^2}D_\lambda(z) - \left(\frac{z^2}{4} - \lambda - \frac{1}{2}\right) D_\lambda(z) = 0. \tag{C.1}$$

This equation is also known as the Weber equation. $D_\lambda(z)$, $D_\lambda(-z)$, $D_{-\lambda-1}(iz)$ and $D_{-\lambda-1}(-iz)$ are the solutions of Eq. (C.1) for non-integer values of λ, which are connected by linear relations. As there are different notations for the parabolic cylinder functions in the literature (see Eq. (C.7)), we denote them in this thesis as $D_\lambda(z)$ (which is the so-called Whittaker notation). The parabolic cylinder functions can be expressed by the following integral representation

$$D_\lambda(z) = \begin{cases} \dfrac{e^{-z^2/4}}{\Gamma(-\lambda)} \displaystyle\int_0^\infty t^{-\lambda-1} e^{-zt-t^2/2} dt & \text{for } \mathrm{Re}(\lambda) < 0, \\ \dfrac{e^{z^2/4}}{\sqrt{\pi/2}} \displaystyle\int_0^\infty t^{\lambda} e^{-t^2/2} \cos(\lambda\pi/2 - zt) dt & \text{for } \mathrm{Re}(\lambda) > -1, \end{cases} \tag{C.2}$$

where $\Gamma(-\lambda)$ is the Gamma function. The two expressions in Eq. (C.2) coincide for $-1 < \mathrm{Re}(\lambda) < 0$.

We have the following recurrence relation for the parabolic cylinder functions

$$D_{\lambda+1}(z) = zD_\lambda(z) - \lambda D_{\lambda-1}(z) \tag{C.3}$$

and the differential relations

$$\frac{d}{dz}D_\lambda(z) = \frac{z}{2}D_\lambda(z) - D_{\lambda+1}(z), \tag{C.4a}$$

$$\frac{d}{dz}D_\lambda(z) = -\frac{z}{2}D_\lambda(z) + \lambda D_{\lambda-1}(z). \tag{C.4b}$$

From these expressions, we can derive the following useful formulas

$$\frac{d}{dz}\exp\left(-z^2/4\right)D_\lambda(z) = -\exp\left(-z^2/4\right)D_{\lambda+1}(z), \tag{C.5a}$$

$$\frac{d}{dz}\exp\left(z^2/4\right)D_\lambda(z) = \lambda\exp\left(z^2/4\right)D_{\lambda-1}(z). \tag{C.5b}$$

Furthermore, we have the product identity

$$D_\lambda(z)D_{\lambda+1}(-z) + D_\lambda(-z)D_{\lambda+1}(z) = \frac{\sqrt{2\pi}}{\Gamma(-\lambda)}. \tag{C.6}$$

In order to study the asymptotic behaviour of $D_\lambda(z)$ and $D_\lambda(-z)$ for large values $z \to \infty$, we need to make a short excursion through the literature and thus, we introduce a different notation for the parabolic cylinder functions, which is often used in references e.g. [29]. We remark for the interested reader that the notation in the following short paragraph is after Miller [74]. By applying the transformation $\lambda \to -\lambda - \frac{1}{2}$, the Weber equation (Eq. (C.1)) changes to

$$\frac{d^2}{dz^2}U(\lambda, z) - \left(\frac{z^2}{4} + \lambda\right)U(\lambda, z) = 0 \tag{C.7}$$

and can be solved by the functions $U(\lambda, z)$ and $V(\lambda, z)$, which are called parabolic cylinder function as well. $U(\lambda, z)$ is also known as the Whittaker function. They

are connected to the previously used functions $D_\lambda(z)$ through

$$U(\lambda, z) = D_{-\lambda-\frac{1}{2}}(z) \tag{C.8}$$

and

$$V(\lambda, z) = \frac{\Gamma\left(\frac{1}{2}+\lambda\right)}{\pi}\left[\sin(\pi\lambda)D_{-\lambda-\frac{1}{2}}(z) + D_{-\lambda-\frac{1}{2}}(-z)\right]. \tag{C.9}$$

Furthermore, we have the relation

$$U(\lambda, -z) = -\sin(\pi\lambda)U(\lambda, z) + \frac{\pi}{\Gamma\left(\frac{1}{2}+\lambda\right)}V(\lambda, z). \tag{C.10}$$

For a fixed λ, we have for the asymptotic behaviour $z \to \infty$

$$U(\lambda, z) \sim z^{-\lambda-\frac{1}{2}} \exp\left(-\frac{z^2}{4}\right), \quad |\arg(z)| < \frac{3}{4}\pi \tag{C.11}$$

and

$$V(\lambda, z) \sim \sqrt{\frac{2}{\pi}} z^{\lambda-\frac{1}{2}} \exp\left(\frac{z^2}{4}\right), \quad |\arg(z)| < \frac{1}{4}\pi. \tag{C.12}$$

Using these results and going back to the previously used notation, we investigate the asymptotic behaviour of the functions $D_\lambda(z)$. Considering the limit $z \to \infty$ now, we have

$$D_\lambda(z) \;=\; U\left(-\lambda-\frac{1}{2}, z\right) \sim z^\lambda \exp\left(-\frac{z^2}{4}\right) \tag{C.13}$$

thus, it decays at infinity. On the other hand, for $D_{-\lambda}(-z)$ we have (using Eq. (C.10))

$$\begin{aligned} D_\lambda(-z) &= U\left(-\lambda-\frac{1}{2}, -z\right) \\ &= -\sin\left(\pi\left(-\lambda-\frac{1}{2}\right)\right)U\left(-\lambda-\frac{1}{2}, z\right) + \frac{\pi}{\Gamma(-\lambda)}V\left(-\lambda-\frac{1}{2}, z\right) \\ &\sim -z^\lambda \exp\left(-\frac{z^2}{4}\right) + z^{-\lambda-1}\exp\left(\frac{z^2}{4}\right), \end{aligned} \tag{C.14}$$

which means it diverges at infinity.

In Chapter 5 we have to check the asymptotic behaviour for large velocities

$v \to \pm\infty$ in the expressions (see Eqs. (5.33), (5.52) and (5.53))

$$D_\Gamma(v+\mu-b+2i\beta), \quad D_\Gamma(-(v+\mu-b+2i\beta)). \tag{C.15}$$

As the argument of the parabolic cylinder function is a complex number ($z = v+\mu-b+2i\beta$), we need to take the above conditions for the argument of $D_\lambda(z)$ into account (see Eqs. (C.11) and (C.12)). We have

$$\arg(v+\mu-b+2i\beta) = \arctan\left(\frac{2i\beta}{v+\mu-b}\right). \tag{C.16}$$

For a fixed β and $v \to \infty$ this expression approaches zero. Thus, the above asymptotic expressions (Eqs. (C.11) - (C.14)) can be used and we find that

$$D_\Gamma(v+\mu-b+2i\beta) \tag{C.17}$$

satisfies the boundary conditions at $v \to \infty$, whereas

$$D_\Gamma(-(v+\mu-b+2i\beta)) \tag{C.18}$$

decays for $v \to -\infty$.

C.2 Confluent hypergeometric function

In this thesis, we use Kummer's confluent hypergeometric function of the first kind also known as Kummer's function, which is denoted as ${}_1F_1(a;b;z)$). Other symbols used in the literature for this hypergeometric function are $M(a,b,z)$ or $\Phi(a;b;z)$. The confluent hypergeometric function is a solution of the confluent hypergeometric differential equation (also called Kummer's equation)

$$z\frac{\partial^2}{\partial z^2}\,{}_1F_1(a;b;z) + (b-z)\frac{\partial}{\partial z}\,{}_1F_1(a;b;z) - a\,{}_1F_1(a;b;z) = 0 \tag{C.19}$$

and can be represented as the following power series

$${}_1F_1(a;b;z) = \sum_{k=0}^{\infty}\frac{(a)_k z^k}{(b)_k k!}. \tag{C.20}$$

Here we have the Pochhammer symbols $(a)_k$ and $(b)_k$ with

$$(a)_n = \frac{\Gamma(a+n)}{\Gamma(a)} = a(a+1)\cdots(a+n-1). \tag{C.21}$$

The confluent hypergeometric function can be expressed by the following integral representation

$${}_1F_1\left(a;b;z\right) = \frac{\Gamma(b)}{\Gamma(b-a)\Gamma(a)} \int_0^1 e^{zt} t^{a-1}(1-t)^{b-a-1} dt \tag{C.22}$$

if the real parts of a and b are larger than zero.

The confluent hypergeometric function can be related to many other functions, e.g.

$${}_1F_1\left(a;a;z\right) = e^z. \tag{C.23}$$

In Chapter 3, we use the connection to the parabolic cylinder functions [2]

$$\begin{aligned} & D_{-\lambda-\frac{1}{2}}(z) + D_{-\lambda-\frac{1}{2}}(-z) \\ = \;& U(\lambda,z) + U(\lambda,-z) \\ = \;& \frac{\Gamma\left(\frac{1}{4}-\frac{\lambda}{2}\right)\cos\left[\pi\left(\frac{1}{4}+\frac{\lambda}{2}\right)\right]}{\sqrt{\pi}2^{\frac{\lambda}{2}-\frac{3}{4}}} \exp\left(-\frac{z^2}{4}\right) {}_1F_1\left(\frac{\lambda}{2}+\frac{1}{4};\frac{1}{2};\frac{z^2}{2}\right), \end{aligned} \tag{C.24}$$

where $U(\lambda,z)$ denotes Whittaker's function (see Eqs. (C.7) and (C.8)). Therefore, we apply Eq. (C.24) to Eq. (3.31)

$$\begin{aligned} & \frac{D_{-s\tau}(\sqrt{2\tau}\eta_0) + D_{-s\tau}(-\sqrt{2\tau}\eta_0)}{D_{-s\tau}(\sqrt{2\tau}\alpha) + D_{-s\tau}(-\sqrt{2\tau}\alpha)} \exp\left[\frac{\tau}{2}\left(\eta_0^2-\alpha^2\right)\right] \\ = \;& \frac{\frac{\Gamma\left(\frac{1}{2}-\frac{s\tau}{2}\right)\cos\left[\pi\left(\frac{s\tau}{2}\right)\right]}{\sqrt{\pi}2^{\frac{s\tau}{2}-\frac{5}{4}}} \exp\left(-\frac{\tau\eta_0^2}{2}\right) {}_1F_1\left(\frac{s\tau}{2};\frac{1}{2};\eta_0^2\tau\right)}{\frac{\Gamma\left(\frac{1}{2}-\frac{s\tau}{2}\right)\cos\left[\pi\left(\frac{s\tau}{2}\right)\right]}{\sqrt{\pi}2^{\frac{s\tau}{2}-\frac{5}{4}}} \exp\left(-\frac{\tau\alpha^2}{2}\right) {}_1F_1\left(\frac{s\tau}{2};\frac{1}{2};\alpha^2\tau\right)} \exp\left[\frac{\tau}{2}\left(\eta_0^2-\alpha^2\right)\right] \\ = \;& \frac{{}_1F_1\left(\frac{s\tau}{2};\frac{1}{2};\eta_0^2\tau\right)}{{}_1F_1\left(\frac{s\tau}{2};\frac{1}{2};\alpha^2\tau\right)} \end{aligned} \tag{C.25}$$

which is the result in Eq. (3.32).

Furthermore, in Chapter 3 we have to compute the following integral (see Eq. (3.33))

$$\tilde{f}(s) = \frac{1}{2}\int_{-1}^{1} \frac{{}_1F_1\left(\frac{s\tau}{2};\frac{1}{2};\eta_0^2\tau\right)}{{}_1F_1\left(\frac{s\tau}{2};\frac{1}{2};\tau\right)} d\eta_0. \tag{C.26}$$

The denominator in Eq. (C.26) does not depend on η_0 and as the argument in the numerator is quadratic in η_0, we only need to consider

$$\frac{1}{2}\int_{-1}^{1} {}_1F_1\left(\frac{s\tau}{2};\frac{1}{2};\eta_0^2\tau\right) d\eta_0 = \int_{0}^{1} {}_1F_1\left(\frac{s\tau}{2};\frac{1}{2};\eta_0^2\tau\right) d\eta_0. \tag{C.27}$$

We apply the substitution $\eta_0^2 = z$ (and $d\eta_0 = |dz/2\sqrt{z}|$) and obtain

$$\int_{0}^{1} \frac{1}{2\sqrt{z}}\, {}_1F_1\left(\frac{s\tau}{2};\frac{1}{2};\tau z\right) dz. \tag{C.28}$$

Thus, we can use the following expression to solve the integral [102]

$$\int z^{\alpha-1}\, {}_1F_1\left(a;b;cz\right) dz = \frac{z^{\alpha}\, {}_2F_2\left(a,\alpha;b,\alpha+1;cz\right)}{\alpha} \tag{C.29}$$

where

$${}_2F_2\left(a_1,a_2;b_1,b_2;z\right) = \sum_{k=0}^{\infty} \frac{(a_1)_k (a_2)_k z^k}{(b_1)_k (b_2)_k k!} \tag{C.30}$$

is the generalized hypergeometric function ${}_2F_2$. From Eq. (C.28) (or Eq. (3.33)) we see that the integrand in Eq. (C.29) has the parameters $a = \frac{s\tau}{2}, b = \frac{1}{2}, c = \tau,\ \alpha = \frac{1}{2}$. Thus, α and b cancel out in Eq. (C.29) (represented by a_2 and b_1 in Eq. (C.30)), and we obtain

$$\int_{0}^{1} {}_1F_1\left(\frac{s\tau}{2};\frac{1}{2};\eta_0^2\tau\right) d\eta_0 = {}_1F_1\left(\frac{s\tau}{2};\frac{3}{2};\tau\right) \tag{C.31}$$

Finally, we have

$$\begin{aligned} \tilde{f}(s) &= \frac{1}{2}\int_{-1}^{1} \frac{{}_1F_1\left(\frac{s\tau}{2};\frac{1}{2};\eta_0^2\tau\right)}{{}_1F_1\left(\frac{s\tau}{2};\frac{1}{2};\tau\right)} d\eta_0 \\ &= \frac{{}_1F_1\left(\frac{s\tau}{2};\frac{3}{2};\tau\right)}{{}_1F_1\left(\frac{s\tau}{2};\frac{1}{2};\tau\right)}. \end{aligned} \tag{C.32}$$

Appendix D

Exit time problem for an Ornstein-Uhlenbeck process

Here we want to sketch the derivation of the exit time distribution (or first passage time distribution) for an Ornstein-Uhlenbeck process with two absorbing boundaries at α_L and α_R. The interested reader may consult [25, 87] as historic accounts and [38] for more detailed and general aspects of exit time problems. We base our computations on a more approachable representation [76]. Our equation of motion is the Ornstein-Uhlenbeck process, which generates the coloured noise (e.g. see Eq. (2.14))

$$\dot{\eta}(t) = -\frac{\eta(t)}{\tau} + \frac{\xi(t)}{\tau}. \tag{D.1}$$

The corresponding Fokker-Planck equation for the propagator $P(\eta, t|\eta_0, 0)$ reads

$$\frac{\partial}{\partial t}P(\eta, t|\eta_0, 0) = \frac{\partial}{\partial \eta}\frac{\eta}{\tau}P(\eta, t|\eta_0, 0) + \frac{1}{2\tau^2}\frac{\partial^2}{\partial \eta^2}P(\eta, t|\eta_0, 0). \tag{D.2}$$

We have the absorbing boundaries

$$P(\alpha_L, t|\eta_0, 0) = 0, \quad P(\alpha_R, t|\eta_0, 0) = 0 \tag{D.3}$$

and the initial condition

$$P(\eta, 0|\eta_0, 0) = \delta(\eta - \eta_0). \tag{D.4}$$

The exit time distribution is related to the propagator of a stochastic process for $\eta(t)$ via

$$f(T,\eta_0) = -\frac{\partial}{\partial T}\int_{\alpha_L}^{\alpha_R} P(\eta,T|\eta_0,0)d\eta. \tag{D.5}$$

There are two different approaches to calculate $f(T,\eta_0)$. The first is based on solving Eq. (D.2) and finding an expression for the propagator $P(\eta,t|\eta_0,0)$ e.g. via its spectral representation. The second way is to derive an equation for the exit time distribution $f(T,\eta_0)$. Here we will follow the latter method. The propagator $P(\eta,t|\eta_0,0)$ satisfies the corresponding backward Kolmogorow equation

$$\frac{\partial}{\partial t}P(\eta,t|\eta_0,0) = -\frac{\eta_0}{\tau}\frac{\partial}{\partial \eta_0}P(\eta,t|\eta_0,0) + \frac{1}{2\tau^2}\frac{\partial^2}{\partial \eta_0^2}P(\eta,t|\eta_0,0). \tag{D.6}$$

The boundary conditions are

$$P(\eta,t|\alpha_L,0) = 0, \quad P(\eta,t|\alpha_R,0) = 0 \tag{D.7}$$

and the initial condition is the same as in Eq. (D.4). From the Eqs. (D.5) and (D.6) we can derive an equation for $f(T,\eta_0)$

$$\frac{\partial}{\partial T}f(T,\eta_0) = -\frac{\eta_0}{\tau}\frac{\partial}{\partial \eta_0}f(T,\eta_0) + \frac{1}{2\tau^2}\frac{\partial^2}{\partial \eta_0^2}f(T,\eta_0) \tag{D.8}$$

with an initial condition

$$f(0,\eta_0) = 0, \quad \alpha_L < \eta_0 < \alpha_R \tag{D.9}$$

and the following boundary conditions

$$f(T,\alpha_L) = \delta(T), \quad f(T,\alpha_R) = \delta(T). \tag{D.10}$$

In order to solve Eq. (D.8), we take the Laplace transform with respect to T

$$\tilde{f}(s,\eta_0) = \int_0^\infty f(T,\eta_0)e^{-sT}dT \tag{D.11}$$

and we obtain

$$\frac{1}{2\tau^2}\frac{\partial^2}{\partial\eta_0^2}\tilde{f}(s,\eta_0) - \frac{\eta_0}{\tau}\frac{\partial}{\partial\eta_0}\tilde{f}(s,\eta_0) - s\tilde{f}(s,\eta_0) = 0. \tag{D.12}$$

The boundary conditions (Eq. (D.10)) translate to

$$\tilde{f}(s,\alpha_L) = 1, \quad \tilde{f}(s,\alpha_R) = 1. \tag{D.13}$$

Thus, Eq. (D.12) has become an ordinary differential equation in Laplace space. Next, we introduce the scaled variable

$$m_0 = \sqrt{2\tau}\eta_0 \tag{D.14}$$

and we get

$$\frac{\partial^2}{\partial m_0^2}\tilde{f}(s,m_0) - m_0\frac{\partial}{\partial m_0}\tilde{f}(s,m_0) - s\tau\tilde{f}(s,m_0) = 0. \tag{D.15}$$

Furthermore, we use the following ansatz

$$\tilde{f}(s,m_0) = e^{m_0^2/4}\tilde{g}(s,m_0) \tag{D.16}$$

and we get rid of the term with the first derivative $\frac{\partial}{\partial m_0}\tilde{f}(s,m_0)$

$$\frac{\partial^2}{\partial m_0^2}\tilde{g}(s,m_0) - \left(\frac{m_0^2}{4} + s\tau - \frac{1}{2}\right)\tilde{g}(s,m_0) = 0 \tag{D.17}$$

Equation (D.17) is called the Weber equation (see Eq. C.1 as well). Its general solution is

$$\tilde{g}(s,m_0) = A_1 D_{-s\tau}(m_0) + A_2 D_{-s\tau}(-m_0) \tag{D.18}$$

where $D_{-s\tau}(m_0)$ and $D_{-s\tau}(-m_0)$ are parabolic cylinder functions and represent the two independent solutions of Eq. (D.17). To find the expressions for the coefficients A_1 and A_2, we have to take into account the absorbing boundaries (Eq. (D.13)). We have

$$e^{\alpha_L^2/4}\tilde{g}(s,\alpha_L) = 1, \tag{D.19a}$$

$$e^{\alpha_R^2/4}\tilde{g}(s,\alpha_R) = 1. \tag{D.19b}$$

Inserting the expression from Eq. (D.18), we get

$$e^{\alpha_L^2/4}[A_1 D_{-s\tau}(\alpha_L) + A_2 D_{-s\tau}(-\alpha_L)] = 1, \tag{D.20a}$$

$$e^{\alpha_R^2/4}[A_1 D_{-s\tau}(\alpha_R) + A_2 D_{-s\tau}(-\alpha_R)] = 1. \tag{D.20b}$$

Solving for A_1 and A_2 yields

$$A_1 = -\frac{\left[D_{-s\tau}(-\alpha_L)e^{-\alpha_R^2/4} - D_{-s\tau}(-\alpha_R)e^{-\alpha_L^2/4}\right]}{D_{-s\tau}(\alpha_L)D_{-s\tau}(-\alpha_R) - D_{-s\tau}(\alpha_R)D_{-s\tau}(-\alpha_L)}, \tag{D.21a}$$

$$A_2 = \frac{\left[D_{-s\tau}(\alpha_L)e^{-\alpha_R^2/4} - D_{-s\tau}(\alpha_R)e^{-\alpha_L^2/4}\right]}{D_{-s\tau}(\alpha_L)D_{-s\tau}(-\alpha_R) - D_{-s\tau}(\alpha_R)D_{-s\tau}(-\alpha_L)}. \tag{D.21b}$$

Thus, we finally obtain for $\tilde{g}(s, m_0)$

$$\begin{aligned}\tilde{g}(s, m_0) = &\frac{\left[D_{-s\tau}(\alpha_L)e^{-\alpha_R^2/4} - D_{-s\tau}(\alpha_R)e^{-\alpha_L^2/4}\right] D_{-s\tau}(-m_0)}{D_{-s\tau}(\alpha_L)D_{-s\tau}(-\alpha_R) - D_{-s\tau}(\alpha_R)D_{-s\tau}(-\alpha_L)} \\ &- \frac{\left[D_{-s\tau}(-\alpha_L)e^{-\alpha_R^2/4} - D_{-s\tau}(-\alpha_R)e^{-\alpha_L^2/4}\right] D_{-s\tau}(m_0)}{D_{-s\tau}(\alpha_L)D_{-s\tau}(-\alpha_R) - D_{-s\tau}(\alpha_R)D_{-s\tau}(-\alpha_L)}.\end{aligned} \tag{D.22}$$

Going backwards with all transformations (see Eqs. (D.14) and (D.16)), we arrive at the following expression for the exit time distribution in Laplace space

$$\begin{aligned}\tilde{f}(s, \eta_0) = &\left[\left(D_{-s\tau}(\sqrt{2\tau}\alpha_L)e^{-\frac{\tau}{2}\alpha_R^2} - D_{-s\tau}(\sqrt{2\tau}\alpha_R)e^{-\frac{\tau}{2}\alpha_L^2}\right) D_{-s\tau}(-\sqrt{2\tau}\eta_0)\right. \\ &- \left.\left(D_{-s\tau}(-\sqrt{2\tau}\alpha_L)e^{-\frac{\tau}{2}\alpha_R^2} - D_{-s\tau}(-\sqrt{2\tau}\alpha_R)e^{-\frac{\tau}{2}\alpha_L^2}\right) D_{-s\tau}(\sqrt{2\tau}\eta_0)\right] \\ &\times \frac{\exp\left(\frac{\tau}{2}\eta_0^2\right)}{D_{-s\tau}(\sqrt{2\tau}\alpha_L)D_{-s\tau}(-\sqrt{2\tau}\alpha_R) - D_{-s\tau}(\sqrt{2\tau}\alpha_R)D_{-s\tau}(-\sqrt{2\tau}\alpha_L)}.\end{aligned} \tag{D.23}$$

For the case of a symmetric exit interval around $\eta_0 = 0$, i.e. $\alpha_R = \alpha$, $\alpha_L = -\alpha$, Eq. (D.22) simplifies to

$$\begin{aligned}\tilde{g}(s, m_0) &= \frac{\left[D_{-s\tau}(-\alpha)e^{-\alpha^2/4} - D_{-s\tau}(\alpha)e^{-\alpha^2/4}\right] D_{-s\tau}(-m_0)}{D_{-s\tau}(-\alpha)D_{-s\tau}(-\alpha) - D_{-s\tau}(\alpha)D_{-s\tau}(\alpha)} \\ &\quad - \frac{\left[D_{-s\tau}(\alpha)e^{-\alpha^2/4} - D_{-s\tau}(-\alpha)e^{-\alpha_L^2/4}\right] D_{-s\tau}(m_0)}{D_{-s\tau}(-\alpha)D_{-s\tau}(-\alpha) - D_{-s\tau}(\alpha)D_{-s\tau}(\alpha)} \\ &= e^{-\alpha^2/4}\frac{D_{-s\tau}(-m_0) + D_{-s\tau}(m_0)}{D_{-s\tau}(-\alpha) + D_{-s\tau}(\alpha)}, \end{aligned} \tag{D.24}$$

and therefore we obtain for the exit time distribution

$$\tilde{f}(s, \eta_0) = \frac{D_{-s\tau}(-\sqrt{2\tau}\eta_0) + D_{-s\tau}(\sqrt{2\tau}\eta_0)}{D_{-s\tau}(-\sqrt{2\tau}\alpha) + D_{-s\tau}(\sqrt{2\tau}\alpha)} \exp\left(\frac{\tau}{2}\left(\eta_0^2 - \alpha^2\right)\right). \tag{D.25}$$

This result is used in Sec. 3.3.2 (Eq. (3.31)).

Bibliography

[1] J. Abate, P. P. Valkó, *Multi-precision Laplace transform inversion*, Int. J. Numer. Meth. Eng **60**, 979 (2004)

[2] M. Abramowitz, I. A. Stegun, *Handbook of Mathematical Functions*, (Dover Publications, New York, 1970)

[3] J. D. Atkinson, T. K. Caughey, *Spectral density of piecewise linear first order systems excited by white noise*, Int. J. Non-Linear Mech. **3**, 137 (1968)

[4] J. D. Atkinson, T. K. Caughey, *First order piecewise linear systems with random parametric excitation*, Int. J. Non-Linear Mech. **3**, 399 (1968)

[5] A. Baule, E. G. D. Cohen, H. Touchette, *A path integral approach to random motion with nonlinear friction*, J. Phys. A: Math. Theor. **43**, 025003 (2010)

[6] A. Baule, H. Touchette, E. G. D. Cohen, *Stick-slip motion of solids with dry friction subject to random vibrations and an external field*, Nonlinearity **24**, 351 (2011)

[7] A. Baule, P. Sollich, *Singular features in noise-induced transport with dry friction*, Europhys. Lett. **97**, 20001 (2012)

[8] A. Baule, P. Sollich, *Rectification of asymmetric surface vibration with dry friction: An exactly solvable model*, Phys. Rev. E **87**, 032112 (2013)

[9] J. J. B. Biemond, N. van de Wouw, H. Nijmeijer, *Bifurcations of equilibrium sets in mechanical systems with dry friction*, Physica D **241**, 1882 (2012)

[10] F. P. Bowden, D. Tabor, *The Friction and Lubrication of Solids*, (Oxford University Press, Oxford 1950)

[11] S. Brandstetter, M. A. Dahlem, E. Schöll, *Interplay of time-delayed feedback control and temporally correlated noise in excitable systems*, Phil. Trans. R. Soc. A, **368**, 391 (2010)

[12] H. Buchholz, *The Confluent Hypergeometric Function with Special Emphasis on its Applications*, (Springer, Berlin, 1969)

[13] R. Burridge, L. Knopoff, *Model and Theoretical Seismicity*, Bull. Seismol. Soc. Am. **57**, 341 (1967)

[14] J. M. Carlson, J. S. Langer, B. E. Shaw, and C. Tang, *Intrinsic properties of a Burridge-Knopoff model of an earthquake fault*, Phys. Rev. A **44**, 884 (1991)

[15] T. K. Caughey, J. K. Dienes, *Analysis of a nonlinear first-order system with a white noise input*, J. Appl. Phys. **32**, 2476 (1961)

[16] M. K. Chaudhury, S. Mettu, *Brownian motion of a drop with hysteresis dissipation*, Langmuir **24**, 6128 (2008)

[17] S. Chandrasekhar, *Stochastic Problems in Physics and Astronomy*, Rev. Mod. Phys. **15**, 1 (1943)

[18] Y. Chen, A. Baule, H. Touchette, W. Just, *Weak-noise limit of a piecewise-smooth stochastic differential equation*, Phys. Rev. E **88**, 052103 (2013)

[19] Y. Chen, W. Just, *First-passage time of Brownian motion with dry friction*, Phys. Rev. E **89**, 022103 (2014)

[20] Y. Chen, W. Just, *On large deviation properties of Brownian motion with dry friction*, Phys Rev. E **90**, 042102 (2014)

[21] A. Colombo, M. di Bernardo, S. J. Hogan, M. R. Jeffrey, *Bifurcations of piecewise-smooth flows: perspectives, methodologies and open problems*, Physica D, **241**, 1845 (2012)

[22] S. Coombes, R. Thul, K. C. A. Wedgwood, *Nonsmooth dynamics in spiking neuron models*, Physica D **241**, 2042 (2012)

[23] S. Coombes, R. Thul, *Synchrony in networks of coupled non-smooth dynamical systems: Extending the master stability function*, Euro. J. Appl. Math. **27**, 904 (2016)

[24] G. Csernák, G. Stépán, *On the periodic response of a harmonically excited dry friction oscillator*, J. of Sound and Vibration **295**, 649 (2006)

[25] D. A. Darling, A. J. F. Siegert, *The first passage problem for a continuous Markov process*, Ann. Math. Stat. **24**, 624 (1953)

[26] P. Das, S. Puri, and M. Schwartz, *Single particle Brownian motion with solid friction*, Eur. Phys. J. E **40**, 60 (2017)

[27] P.-G. de Gennes, *Brownian motion with dry friction*, J. Stat. Phys. **119**, 953 (2005)

[28] M. di Bernardo, C. J. Budd, A. R. Champneys, P. Kowalczyk, *Piecewise-smooth Dynamical Systems: Theory and Applications* (Springer, Berlin, 2008)

[29] *NIST Digital Library of Mathematical Functions* http://dlmf.nist.gov/, Release 1.0.18 of 2018-03-27. F. W. J. Olver, A. B. Olde Daalhuis, D. W. Lozier, B. I. Schneider, R. F. Boisvert, C. W. Clark, B. R. Miller, B. V. Saunders, eds.

[30] F.-J. Elmer, *Nonlinear dynamics of dry friction*, J. Phys. A: Math. Gen. **30**, 6057 (1997)

[31] A. Erdélyi, W. Magnus, F. Oberhettinger, F. G. Tricomi, *Higher transcendental functions*, based on left notes by H. Batemann, Vol. II, (McGraw-Hill, New York, 1953)

[32] P. Eshuis, K. van der Weele, D. Lohse, D. van der Meer, *Experimental Realization of a Rotational Ratchet in a Granular Gas*, Phys. Rev. Lett. **104**, 248001 (2010)

[33] E. Fick, G. Sauermann, *The quantum statistics of dynamic processes*, (Springer, New York, 1990)

[34] A. F. Filippov, *Differential Equations with Discontinuous Righthand Sides*, (Kluwer, Dordrecht, 1988)

[35] E. Fodor, C. Nardini, M. E. Cates, J. Tailleur, P. Visco, F. van Wijland, *How Far from Equilibrium Is Active Matter?*, Phys. Rev. Lett. **117**, 038103 (2016)

[36] R. F. Fox, *Functional-calculus approach to stochastic differential equations*, Phys. Rev. A **33**, 467 (1986)

[37] R. F. Fox, *Uniform convergence to an effective Fokker-Planck equation for weakly colored noise*, Phys. Rev. A **34**, 4525 (R) (1986)

[38] C. Gardiner, *Stochastic methods: A Handbook for the Natural and Social Sciences*, (Springer, Berlin, 2009)

[39] P. M. Geffert, W. Just, *Nonequilibrium dynamics of a pure dry friction model subjected to colored noise*, Phys. Rev. E **95**, 062111 (2017)

[40] A. Gnoli, A. Petri, F. Dalton, G. Pontuale, G. Gradenigo, A. Sarracino, A. Puglisi, *Brownian ratchet in a thermal bath driven by Coulomb friction*, Phys. Rev. Lett **110**, 120601 (2013)

[41] A. Gnoli, A. Puglisi, H. Touchette, *Granular Brownian motion with dry friction*, Europhys. Lett. **102**, 14002 (2013)

[42] P. S. Goohpattader, S. Mettu, M. K. Chaudhury, *Experimental investigation of the drift and diffusion of small objects on a surface subjected to a bias and external white noise: roles of Coulomb friction and hysteresis*, Langmuir **25**, 9969 (2009)

[43] P. S. Goohpattader, M. K. Chaudhury, *Diffusive motion with nonlinear friction: apparently Brownian*, J. Chem. Phys. **133**, 024702 (2010)

[44] P. S. Goohpattader, M. K. Chaudhury, *Random motion with interfacial contact: driven diffusion vis-á-vis mechanical activation*, Eur. Phys. J. E **35**, 67 (2012)

[45] R. Graham, H. Haken, *Generalised thermodynamic potential for Markoff systems in detailed balance and far from thermal equilibrium*, Z Phys. A **243**, 289 (1971)

[46] M. S. Green, *Markoff Random Processes and the Statistical Mechanics of Time-Dependent Phenomena. II. Irreversible Processes in Fluids*, J. Chem. Phys. **22**, 398 (1954)

[47] P. Hänggi, P. Jung, *Colored noise in dynamical systems*, Adv. Chem. Phys. **89**, 239 (1995)

[48] H. Hayakawa, *Langevin equation with Coulomb friction*, Physica D **205**, 48 (2005)

[49] J. F. Heagy, N. Platt, S. M. Hammel, *Characterization of on-off intermittency*, Phys. Rev. E **49**, 1140 (1994)

[50] W. Horsthemke, R. Lefever, *Noise-Induced Transitions*, (Springer, Berlin, 1984)

[51] R. C. Hudson, C. R. Finfgeld, *Laplace transform solution for the oscillator damped by dry friction*, Am. J. Phys. **39**, 568 (1971)

[52] L. H'walisz, P. Jung, P. Hänggi, P. Talkner, L. Schimansky-Geier, *Colored noise driven systems with inertia*, Z. Phys. B - Cond. Mat. **77**, 471 (1989)

[53] M. R. Jeffrey, *Nondeterminism in the limit of nonsmooth dynamics*, Phys. Rev. Lett. **106**, 254103 (2011)

[54] M. R. Jeffrey, *Three discontinuity-induced bifurcations to destroy self-sustained oscillations in a superconducting resonator*, Physica D **241**, 2077 (2012)

[55] P. Jung, P. Hänggi, *Dynamical systems: A unified colored noise-approximation*, Phys. Rev. A **35**, 4464 (R) (1987)

[56] W. Just, H. Kantz, M. Ragwitz, F. Schmüser, *Nonequilibrium physics meets time series analysis: Measuring probability currents from data*, Europhys. Lett. **62**, 28 (2003)

[57] A. Kawarada, H. Hayakawa, *Non-Gaussian velocity distribution function in a vibrating granular bed*, J. Phys. Soc. Jpn. **73**, 2037 (2004)

[58] K. Kanazawa, T. G. Sano, T. Sagawa, H. Hayakawa, *Asymptotic derivation of Langevin-like equation with non-Gaussian noise and its analytical solution*, J. Stat. Phys. **160**, 1294 (2015)

[59] H. Kramers, *Brownian motion in a field of force and the diffusion model of chemical reactions*, Physica **7**, 284 (1940)

[60] P. E. Kloeden, E. Platen, H. Schurz, *Numerical Solution of SDE through Computer Experiments*, (Springer, Berlin, 1994)

[61] R. Kubo, *Statistical-Mechanical Theory of Irreversible Processes. I. General Theory and Simple Applications to Magnetic and Conduction Problems*, J. Phys. Soc. Jpn. **12**, 570 (1957)

[62] R. Kubo, *A Stochastic Theory of Line-Shape and Relaxation*, in *Fluctuation, Relaxation and Resonance in Magnetic Systems*, edited by D. ter Haar, (Oliver and Boyd, Edinburgh, 1962)

[63] R. Kubo, M. Toda, N. Hashitsume, *Statistical physics II: Nonequilibrium statistical mechanics*, (Springer, Berlin, 1991)

[64] C. Lihua, *Systems Driven by Colored Poisson Noise: Unified Colored Noise Approximation*, Commun. Theor. Phys. **30**, 45 (1998)

[65] C. Maggi, U. M. B. Marconi, N. Gnan, R. Di Leonardo, *Multidimensional stationary probability distribution for interacting active particle*, Sci. Rep. **5**, 10742 (2015)

[66] W. Magnus, F. Oberhettinger, R. P. Soni, *Formulas and Theorems for the Special Functions of Mathematical Physics*, (Springer, Berlin, 1966)

[67] S. N. Majumdar, A. Comtet, *Exact asymptotic results for persistence in the Sinai model with arbitrary drift*, Phys. Rev. E **66**, 061105 (2002)

[68] O. Makarenkov, J. S. W. Lamb, *Dynamics and bifurcations of nonsmooth systems: a survey*, Physica D **241**, 1826 (2012)

[69] A. Manarconda, A. Puglisi, A. Sarracino, *Coulomb friction driving Brownian motors*, Commun. Theor. Phys. **62**, 505 (2014)

[70] M. Marszal, A. Stefański, *Synchronization Properties in Coupled Dry Friction Oscillators* in *Nonlinear Dynamical Systems with Self-Excited and Hidden Attractors*, Studies in Systems, Decision and Control, edited by V.-T. Pham, S. Vaidyanathan, C. Volos, T. Kapitaniak, (Springer, 2018)

[71] A. Mauger, *Anomalous motion generated by the Coulomb friction in the Langevin equation*, Physica A **367**, 129 (2006)

[72] A. M. Menzel, N. Goldenfeld, *Effect of Coulombic friction on spatial displacement statistics*, Phys. Rev. E **84**, 011122 (2011)

[73] S. Mettu, M. K. Chaudhury *Stochastic Relaxation of the Contact Line of a Water Drop on a Solid Substrate Subjected to White Noise Vibration: Roles of Hysteresis*, Langmuir **26**, 8131 (2010)

[74] J. C. P. Miller *On the choice of standard solutions to Weber's equation*, Proc. Cambridge Philos. Soc. **48**, 428 (1952)

[75] W. Moon and J. S. Wettlaufer *On the interpretation of Stratonovich calculus*, New J. Phys. **16**, 055017 (2014)

[76] E. Orlandini, *First passage time problems*, Lecture notes (2012/2013), University of Padova

[77] M. Pascal, *Dynamics of coupled oscillators excited by dry friction*, J. Comput. Nonlinear Dynam. **3**, 031009 (2008)

[78] M. Pascal, *A new model of dry friction oscillator colliding with a rigid obstacle*, Nonlinear Dyn. **91**, 2541 (2018)

[79] L. M. Pecora, T. L. Carroll, *Master stability functions for synchronized coupled systems*, Phys. Rev. Lett. **80**, 2109 (1998)

[80] A. Pototsky, F. Marchesoni, *Periodically driven Brownian motion with dry friction and ultrarelativistic Langevin equations*, Phys. Rev. E **87**, 032132 (2013)

[81] P. Reimann, *Brownian motors: Noisy transport far from equilibrium*, Phys. Rep. **361**, 57 (2002)

[82] H. Risken, *The Fokker-Planck equation: Methods of Solution and Applications*, (Springer, Berlin, 1989)

[83] T. G. Sano, H. Hayakawa, *Roles of dry friction in the fluctuating motion of an adiabatic piston*, Phys. Rev E **89**, 032104 (2014)

[84] T. G. Sano, K. Kanazawa, H. Hayakawa, *Granular rotor as a probe for a nonequilibrium bath*, Phys. Rev. E **94**, 032910 (2016)

[85] A. Sarracino, A. Gnoli, A. Puglisi, *Ratchet effect driven by Coulomb friction: The asymmetric Rayleigh piston*, Phys. Rev. E **87**, 040101 (R) (2013)

[86] A. Sarracino, *Time asymmetry of the Kramers equation with nonlinear friction: Fluctuation-dissipation relation and ratchet effect*, Phys. Rev. E **88**, 052124 (2013)

[87] A. J. F. Siegert, *On the First Passage Time Probability Problem*, Phys. Rev. **81**, 617 (1951)

[88] D. J. W. Simpson, R. Kuske, *Stochastically perturbed sliding motion in piecewise-smooth systems*, Discrete Contin. Dyn. Syst. Ser. B **19**, 2889 (2014)

[89] D. J. W. Simpson, R. Kuske, *The positive occupation time of Brownian motion with two-valued drift and asymptotic dynamics of sliding motion with noise*, Stoch. Dyn. **14**, 1450010 (2014)

[90] D. J. W. Simpson, R. Kuske, *Stochastic perturbations of periodic orbits with sliding*, J. Nonlin. Sci. **25**, 967 (2015)

[91] A. Talbot, *The accurate numerical inversion of Laplace transforms*, IMA J. Appl. Math. **23**, 97 (1979)

[92] J. Talbot, R. D. Wildman, P. Viot, *Kinetics of a frictional granular motor*, Phys. Rev. Lett. **107**, 138001 (2011)

[93] J. Talbot, P. Viot, *Effect of dynamic and static friction on an asymmetric granular piston*, Phys. Rev. E **85**, 021310 (2012)

[94] H. Touchette, E. Van der Straeten, W. Just, *Brownian motion with dry friction: Fokker-Planck approach*, J. Phys. A: Math. Theor. **43**, 445002 (2010)

[95] H. Touchette, T. Prellberg, W. Just, *Exact power spectra of Brownian motion with solid friction*, J. Phys. A: Math. Theor. **45**, 395002 (2012)

[96] N. G. van Kampen, *Derivation of the phenomenological equations from the master equation: I. Even variables only*, Physica **23**, 707 (1957)

[97] N. G. van Kampen, *Derivation of the phenomenological equations from the master equation: II. Even and odd variables*, Physica **23**, 816 (1957)

[98] C. Wensrich, *Slip-stick motion in harmonic oscillator chains subject to Coulomb friction*, Tribology Intern. **39**, 490 (2006)

[99] R. Wittmann, C. Maggi, A. Sharma, A. Scacchi, J. M. Brader and U. M. B. Marconi, *Effective equilibrium states in the colored-noise model for active matter I. Pairwise forces in the Fox and unified colored noise approximations*, J. Stat. Mech. 113207 (2017)

[100] J. Wojewoda, A. Stefański, M. Wiercigroch, T. Kapitaniak, *Hysteretic effects of dry friction: modelling and experimental studies*, Phil. Trans. R. Soc. A **366**, 747 (2008)

[101] E. Wong, M. Zakai, *On the convergence of ordinary integrals to stochastic integrals*, Ann. Math. Stat. **36**, 1560 (1965)

[102] Wolfram Research,
Kummer confluent hypergeometric function ${}_1F_1$, Integration formula,
Wolfram Research, Inc., 29 Oct 2001,
http://functions.wolfram.com/07.20.21.0002.01

[103] L. F. C. Zonetti, A. S. S. Camargo, J. Sartori, D. F. de Sousa and L. A. O. Nunes, *A demonstration of dry and viscous damping of an oscillating pendulum*, Eur. J. Phys. **20**, 85 (1999)